

Femtosecond laser induced biomimetic surfaces with unique wetting and optical properties

MSc Thesis

Christina Lanara

Supervisor: prof. Emmanuel Stratakis

Co-supervisors: prof. Ioannis Remediakis

prof. Dimitrios Papazoglou

Heraklion, Crete, July 2019

**Δημιουργία βιομημικών επιφανειών με
ξεχωριστές διαβροχικές και οπτικές
ιδιότητες μέσω λέιζερ υπέρ-στενων παλμών**

Μεταπτυχιακή εργασία

Χριστίνα Λαναρά

Επιβλέπων : καθ. Εμμανουήλ Στρατάκης

Ακαδημαϊκοί επιβλέποντες: καθ. Ιωάννης Ρεμεδιάκης

καθ. Δημήτριος Παπάζογλου

Ηράκλειο, Κρήτη, Ιούλιος 2019

Preface

This MSc thesis has been elaborated in the Materials Science and Technology Department of the University of Crete (UoC) in collaboration with the Ultrafast Laser Micro and Nano Processing Laboratory (*ul μ +n*) of the Institute of Electronic Structure and Laser (IESL) of the Foundation for Research and Technology-Hellas (FORTH).

It has been supported by Horizon 2020 European Union's research and innovation programme under Grant Agreement No. 665337 ("LiNaBioFluid"; URL: <http://www.laserbiofluid.eu>) and HELLAS-CH-LASERLAB (MIS 5002735) implemented under "Action for Strengthening Research and Innovation Infrastructures," funded by the Operational Programme "Competitiveness, Entrepreneurship and Innovation" (NSRF 2014-2020) and co-financed by Greece and the European Union (European Regional Development Fund) – MSc scholarships.



Acknowledgments

I am greatly indebted to my advisor and supervisor Prof. Emmanuel Stratakis who gave me the opportunity to work in the laboratories of the Institute of Electronic Structure and Laser of the Foundation for Research and Technology – Hellas and accomplish this MSc Thesis. More specifically, for the acceptance to work in the Ultrafast Laser Micro and Nano Processing Laboratory, which is a group of great people. Also for the confidence he showed me and his advices on the project.

Also, I would like to thank Prof. Ioannis Remediakis and Prof. Dimitrios Papazoglou, who conceded to be in the examination committee of my thesis. I didn't have the opportunity to work with them experimentally on the present thesis, but it would be a pleasure for me to work with them in the future. However, some advices of Prof. Remediakis, as for the project, were very helpful for me and I appreciate the time he spent with me.

Additionally, I would like to express my full appreciation to the person who is responsible for many of these that you will read in my thesis, but also for many things that you will not read. This person is none other than Chara Simitzi and she is the person that taught me how to work in a laboratory. I would like to thank her for her endless help and support, both in experimental and personal part. Her help was invaluable, since the first time she showed me how to cut a silicon substrate. Even if she lives in UK now, she always answer to my e-mails, scientific or not.

I would also like to express my special thanks and gratitude to my collaborator Alexandros Mimidis, who helped me with a large part of my project and for the happy moments that he offered any time.

Many thanks to my friend and collaborator Evaggelos Skoulas for his support all this time. I think that without him I would not have learned many things, scientific or not.

Also, I would like to thank the SEM girl, Aleka Manousaki, for the infinite SEM images and for the unlimited discussions we had each time. The only times I do not remember what we were discussing about, were when she was telling me to go to the SEM at nine o'clock in the morning, because coffee was not allowed.

Additionally I would like to thank Dr. Antonios Kanaras from School of Physics and Astronomy at Southampton University, for the synthesis of gold nanoparticles and their immediate sent.

I would also like to thank Andreas Lemonis and Antonis Papadopoulos, all my friends and the post-graduate students at FORTH. Their continuous support has been invaluable to me.

Finally, I would like to thank my family for their endless support all these 25 years of my life. Without them I would not be the person that I am today.

Thank you all – July 2019, Heraklion, Crete

Christina Lanara

Abstract

Biomimetics offer the possibility of biological systems simulation on artificial surfaces, with desired properties. There are many attempts to fabricate artificially these surfaces.

The present thesis comprises three parts. The first one is the fabrication of micropatterned silicon substrates via ultra-short pulsed laser irradiation under different experimental parameters, including laser fluence. The second part is the fabrication of hierarchical micro-nano-patterned substrates. These comprise micropatterned silicon substrates which have been thermally oxidized and nano-decorated with spherical and rod shaped gold nanoparticles of various functionalities and sizes. Gold nanoparticles have been attached via silane chemistry. Both types of substrates have been characterized with respect to their morphological, wetting and optical properties. The third part is the fabrication of micropatterned steel substrates via ultra-short pulsed laser irradiation under different experimental parameters, including irradiation medium. Steel samples fabricated, for constant laser fluence, in air and ammonia gaseous environments.

Regarding the micropatterned substrates, the morphological characterization showed that as the laser fluence increased, the roughness of the surface increased as well. Micropatterned substrates comprised microcones of varying height and density. Specifically, the density and the height of the micro-features (i.e. microcones) decreased and increased respectively, with increasing laser fluence. Optical characterization showed that as the surface roughness appears, the absorbance increased, across the range of wavelength (250-2000nm). The layer of silicon oxide on flat silicon substrates lead to reduction of the reflectance, in contrast with the case of micro-structured substrates, where silicon oxide layer increased the reflectivity, in near infrared spectrum. This leads to absorbance reduction in near IR range but very high absorbance efficiency in UV/Vis range (~97%).

Regarding the hierarchical micro-nano substrates, SEM analysis confirmed the successful deposition of the gold nanoparticles on the micropatterned silicon substrates. Deposition gave a homogenous distribution of single nanoparticles and some regions of small clusters. All types of the gold nanoparticles (NPs) being tested, which carried diverse functionalities (e.g. oligopeptides, including the CALNN-RGD

and organic moieties, including the DMAP) have been successfully attached on the surfaces of the micropatterned silicon substrates. Rod shaped AuNPs do not carry any ligands. Remarkably, the NPs covered the whole 3D surface of the micropatterned substrates giving a distribution that was comparable to that on the flat silicon substrates. Optical characterization showed that gold nanoparticles caused increment of absorbance of the oxidized micro-patterned silicon substrates in near IR range.

Finally, steel micro-patterned substrates have been characterized for their morphological and wetting properties. Morphological characterization showed that in presence of reactive gas (ammonia), during the irradiation procedure, steel microcones were smaller and shorter than the air-structured ones. As for the wetting characterization, in the case of air-structured surfaces there was non stable wetting behavior, in contrast with the ammonia-structured steel surfaces which remained hydrophilic for over 100 contact angle measurement days. Also, the ammonia-structured surfaces appeared anti-corrosive behavior.

Περίληψη

Η Βιομιμητική προσφέρει τη δυνατότητα της προσομοίωσης βιολογικών συστημάτων σε τεχνητές επιφάνειες, με επιθυμητές ιδιότητες. Έχουν γίνει πολλές προσπάθειες για την τεχνητή κατασκευή αυτών των επιφανειών.

Η παρούσα διατριβή αποτελείται από τρία μέρη. Το πρώτο είναι η κατασκευή μικροδομημένων υποστρωμάτων πυριτίου μέσω ακτινοβολήσης με λέιζερ υπέρ-στενων παλμών, υπό διαφορετικές πειραματικές παραμέτρους, συμπεριλαμβανομένης της πυκνότητας ενέργειας. Το δεύτερο μέρος είναι η κατασκευή των ιεραρχικών μικρο-νανο-δομημένων υποστρωμάτων. Αυτές περιλαμβάνουν μικρο-δομημένα και οξειδωμένα υποστρώματα πυριτίου, που είναι νανο-διακοσμημένα με σφαιρικά και ραβδωτά νανოსωματίδια χρυσού διαφόρων λειτουργικών ομάδων και μεγεθών. Τα νανოსωματίδια χρυσού έχουν συνδεθεί μέσω της χημείας σιλανίου. Και οι δύο τύποι υποστρωμάτων έχουν χαρακτηρίζονται σε σχέση με τη μορφολογία τους και οπτικές τους ιδιότητες. Το τρίτο μέρος είναι η κατασκευή μικροδομημένων υποστρωμάτων ατσαλιού μέσω ακτινοβολήσης με λέιζερ υπέρ-στενων παλμών, υπό διαφορετικές πειραματικές παραμέτρους, συμπεριλαμβανομένου του περιβάλλοντος ακτινοβολήσης. Τα δείγματα ατσαλιού κατασκευάστηκαν με σταθερή πυκνότητα ενέργειας, σε περιβάλλον ακτινοβολήσης αέρα και αμμωνίας.

Όσον αφορά τις μικρο-δομημένες επιφάνειες, ο μορφολογικός χαρακτηρισμός έδειξε ότι καθώς η πυκνότητα ενέργειας λέιζερ αυξάνει, αυξάνει και η τραχύτητα της επιφάνειας. Τα μικροδομημένα υποστρώματα εμφάνισαν δομές μικροκώνων ποικίλου ύψους και πυκνότητας. Πιο συγκεκριμένα, η πυκνότητα και το ύψος των μικρο-δομών (δηλαδή των μικρο-κώνων) μειωνόταν και αυξανόταν αντίστοιχα, με την αύξηση της πυκνότητας ενέργειας του λέιζερ. Ο οπτικός χαρακτηρισμός έδειξε ότι καθώς η επιφανειακή τραχύτητα εμφανίζεται, η απορρόφηση αυξάνεται, σε όλο το εύρος του μήκους κύματος (250-2000nm). Το στρώμα οξειδίου του πυριτίου σε επίπεδες επιφάνειες πυριτίου οδηγεί σε μείωση του συντελεστή ανάκλασης, σε αντίθεση με την περίπτωση των μικρο-δομημένων υποστρωμάτων, όπου το στρώμα οξειδίου του πυριτίου αύξησε την ανακλαστικότητα, στο εγγύς υπέρυθρο φάσμα. Αυτό οδηγεί σε μείωση της απορρόφησης στο εγγύς υπέρυθρο φάσμα αλλά υψηλή απορροφητική απόδοση στο υπεριώδες/ορατό φάσμα (~97%).

Όσον αφορά τις ιεραρχικά δομημένα υποστρώματα, η ανάλυση SEM επιβεβαίωσε την επιτυχή εναπόθεση των νανοσωματιδίων χρυσού στις μικρο-δομημένες επιφάνειες πυριτίου. Η εναπόθεση απέδωσε μια ομοιογενή κατανομή νανοσωματιδίων με ορισμένες περιοχές μικρών συστάδων. Όλοι οι τύποι των νανοσωματιδίων χρυσού που δοκιμάστηκαν, και τα οποία φέρουν ποικίλες λειτουργικότητες (π.χ. ολιγοπεπτίδια, συμπεριλαμβανομένου του CALNN-RGD και οργανικές ενώσεις, συμπεριλαμβανομένου του DMAP) έχουν επιτυχώς συνδεθεί επί των μικροδομημένων επιφανειών των υποστρωμάτων πυριτίου. Είναι αξιοσημείωτο ότι τα νανοσωματίδια χρυσού μπόρεσαν να καλύψουν όλη την επιφάνεια των τριασδιάστατων μικροδομημένων υποστρωμάτων δίνοντας μια κατανομή η οποία ήταν συγκρίσιμη με εκείνη για τα επίπεδα υποστρώματα πυριτίου.. Ο οπτικός χαρακτηρισμός έδειξε ότι τα νανοσωματίδια χρυσού έχουν την τάση να αυξάνουν την απορρόφηση του οξειδωμένου μικρο-δομημένου υποστρώματος πυριτίου στο εγγύς υπέρυθρο φάσμα.

Τέλος, τα μικροδομημένα υποστρώματα ατσαλιού χαρακτηρίστηκαν για τις μορφολογικές και διαβροχικές τους ιδιότητες. Ο μορφολογικός χαρακτηρισμός έδειξε ότι παρουσία δραστικού αερίου κατά την ακρινοβόληση (αμμωνία), οι μικρο-κώννοι είναι μικρότεροι και χαμηλότεροι, συγκριτικά με αυτούς που παρασκευάστηκαν σε περιβάλλον αέρα. Όσο για τον διαβροχικό χαρακτηρισμό, οι επιφάνειες που παρασκευάστηκαν σε περιβάλλον αέρα δεν παρουσίασαν σταθερή διαβροχική συμπεριφορά, σε αντίθεση με τις επιφάνειες ατσαλιού που παρασκευάστηκαν σε περιβάλλον αμμωνίας οι οποίες παρέμειναν υδρόφιλες για πάνω από 100 μέρες μετρήσεων γωνίας επαφής. Επίσης, οι επιφάνειες ατσαλιού που παρασκευάστηκαν σε περιβάλλον αμμωνίας εμφάνισαν αντioxειδωτική συμπεριφορά.

TABLE OF CONTENTS

Acknowledgements	-4-
Abstract	-5-
Table of contents	-9-
List of Abbreviations	-12-
1.General Overview	-13-
1.1 Biomimetic micro/nano functional surfaces	-13-
1.1.1 Biomimetics.....	-13-
1.1.2 Biomimetic fabrication of hierarchical surfaces.....	-14-
1.1.3 Biomimetic micro/nano functional surfaces for microfluidic applications.....	-16-
1.1.4 Biomimetic micro/nano functional surfaces for tailoring the optical properties.....	-18-
1.2 Laser – Solid interactions.....	-19-
1.2.1 Silicon.....	-20-
1.2.2 Steel.....	-28-
1.2.3 Fundamental processes of laser – matter interaction.....	-31-
1.2.3.1 Primary processes – Absorption mechanisms.....	-33-
1.2.3.2 Secondary processes – Energy relaxation.....	-35-
1.2.4 Laser induced periodic surface structures (LIPSS).....	-36-
1.2.4.1 Surface plasmon waves.....	-38-
1.2.5 Surface structuring of silicon via ultrashort – pulsed laser processing...	-40-
1.2.6 Surface structuring of steel via ultrashort – pulsed laser processing....	-42-
1.3 Gold nanoparticles.....	-44-
1.3.1 Synthesis of gold nanoparticles.....	-45-
1.3.2 Properties of gold nanoparticles.....	-47-
2. Aim of the thesis	-51-
2.1 Problem statement & aim of thesis.....	-51-
2.2 Flow sheet.....	-52-

3. Experimental part : Materials & methods.....	53-
3.1 Fabrication of micropatterned silicon surfaces via ultrashort – pulsed laser....	
.....	-53-
3.1.1 Laser system.....	-53-
3.1.2 Experimental procedure.....	-53-
3.1.3 Sample preparation.....	-54-
3.1.4 Thermal oxidation of the substrates.....	-54-
3.2 Gold nanoparticles used.....	-55-
3.3 Deposition of gold nanoparticles onto the microstructured silicon surfaces....	
.....	-56-
3.4 Fabrication of micropatterned steel surfaces via ultrashort – pulsed laser...-	58-
3.4.1 Corrosion procedure of the microstructured steel surfaces.....	-58-
3.5 Characterization of the micro/nano patterned silicon & steel surfaces.....	-59-
3.5.1 Scanning electron microscopy (SEM).....	-59-
3.5.1.1 Technique.....	-59-
3.5.1.2 Experimental process.....	-59-
3.5.2 Energy-dispersive X-ray spectroscopy (EDS).....	-59-
3.5.2.1 Technique.....	-59-
3.5.2.2 Experimental process).....	-60-
3.5.3 Wetting response by static contact angle.....	-60-
3.5.3.1 Fundamentals.....	-60-
3.5.3.1.1 Young’s equation.....	-60-
3.5.3.1.2 Wenzel and Cassie Baxter states.....	-62-
3.5.3.2 Technique.....	-63-
3.5.3.3 Experimental process.....	-63-
3.5.4 Ellipsometry.....	-64-
3.5.4.1 Technique.....	-64-
3.5.4.2 Experimental process.....	-65-
3.5.5 Optical response by UV/Vis spectrophotometry.....	-65-
3.5.5.1 Optical parameters.....	-66-

3.5.5.2 Technique.....	67-
3.5.5.3 Experimental process.....	67-
4. Experimental part : Results.....	67-
4.1 Characterization of artificially structured silicon surfaces.....	67-
4.1.1 Morphological characterization of microstructured silicon surfaces..	67-
4.1.1.1 The effect of laser fluence.....	68-
4.1.1.2 Hierarchical micro/nano patterned silicon surfaces.....	70-
4.1.2 Optical properties of micro/nano - patterned silicon substrates.....	71-
4.1.2.1 The effect of roughness.....	72-
4.1.2.2 The effect of SiO ₂ thickness layer.....	73-
4.1.2.3 The effect of gold nanoparticles.....	75-
4.2 Characterization of artificially structured steel surfaces.....	76-
4.2.1 Morphological characterization of microstructured steel surfaces – The effect of NH ₃ reactive gas.....	76-
4.2.2 Wetting properties of micro/nano – patterned steel substrates.....	78-
4.2.2.1 The effect of irradiation environment.....	78-
4.2.2.2 The effect of corrosion procedure.....	79-
5. Discussion & Conclusions.....	82-
5.1 Micropatterned steel & silicon substrates fabricated via ultrashort-pulsed laser processing as artificial biomimetic surfaces.....	82-
5.2 Irradiation parameters influence the surface micro-topography.....	82-
5.3 The influence of surface roughness on the optical properties of Si micropatterned surfaces.....	83-
5.4 Surface functionality influence the optical response of Si micropatterned surfaces.....	85-
5.5 The influence of surface chemistry on the wetting properties of steel micropatterned surfaces.....	86-
6. References.....	88-

List of Abbreviations

AuNPs: Gold Nanoparticles
C.A.: Contact Angle
CW: Continuous Wave
DMAP: 4-DiMethylAminoPyridine
EDS: Energy-dispersive X-ray spectroscopy
 E_g : Energy band gap
HF: Hydrofluoric acid
HAZ: Heat-Affected Zone
HSFR: High Spatial Frequency Ripples
IR: Infrared
LIPSS: Laser Induced Periodic Surface Structures
LSFR: Low Spatial Frequency Ripples
LSPR: Localized Surface Plasmon Resonance
MCs: Microcones
MPTMS: (3-Mercaptopropyl)trimethoxysilane
 NH_3 : Ammonia
SEM: Scanning Electron Microscopy
 SF_6 : Sulfur hexafluoride
Si: Silicon
 SiO_2 : Silicon oxide
S-P: Surface Plasmon
S-PP: Surface Plasmon Polariton
SPR: Surface Plasmon Resonance
UV: Ultraviolet
Vis: Visible

1 General overview

1.1 Biomimetic micro/nano functional surfaces

What has wings like a butterfly, skin like a shark, and eyes like a moth? The future of science...

1.1.1 Biomimetics

Biomimetics (word coined by Otto Schmitt in 1957), or biomimicry (word coined in 1960 by Jack Steele), based on the effort of people to listen to the nature. The driving force is the restless perfection of nature, where everything is "tuned" to work perfectly. Nature is a source of inspiration, since it presents a unique and distinct ways to solve complex problems. The study and simulation of biological systems with desired properties is popularly known as *biomimetics* [Stratakis, E. I. and Zorba, V., 2010¹]. Although biomimetics exists from Daedalus and Icarus, who imitated the birds, biomimetics has evolved in recent years because of the development of nanotechnology, which takes impulses from biological systems (both flora as and fauna) which have surfaces composed of micro- and nano-structures with a special role, and in general there is a great diversity of surface structures in different sizes. Currently, a large area of biomimetic research deals with functional micro- and nanostructures for nanoscale devices, water repellence, self-cleaning, drag reduction in fluid flow, energy conversion and conservation, high adhesion, aerodynamic lift, materials and fibers with high mechanical strength, antireflection, structural coloration, thermal insulation, self-healing, responsiveness, and sensory aid mechanisms¹. All the above applications are based on biological systems and the excellent functional properties they have, so leading us to continually attempt to construct operably optimum surfaces such as those found in nature.

1.1.2 Biomimetic fabrication of hierarchical surfaces

The greater range of biomimetic research relates to the construction of functional micro- and nanostructures on respective surfaces. Since surfaces incorporating structures of different size scales (micro- and nano-scale) are characterized as

hierarchical. Nature develops biological objects by means of growth or biologically controlled self-assembly adapting to the environmental condition. Such adaptive and responsive self-assembly is provided by means of a hierarchical self-organization and optimization of the biological material at each level of hierarchy, so as to yield outstanding performance [Xia, F., and Jiang, L., 2008²]. Biological materials are highly organized from the molecular to the nano-, micro-, and macroscales, often in a hierarchical manner with intricate nanoarchitecture that ultimately makes up a myriad of different functional elements [Alberts B. et al., 2008³]. Similar to all natural materials, biological surfaces exhibit hierarchical morphology at the micro- and the nanoscales while the desired functionality is achieved through a tailored synergy of surface roughness and chemistry [Stratakis E. et al., 2011⁴]. The hierarchical structure of biological surfaces, attains considerable interest for the development of nanotechnology, both in the understanding of such multifunctional systems, and to the effort to implement, some interesting examples of which are shown in Figure 1.1.

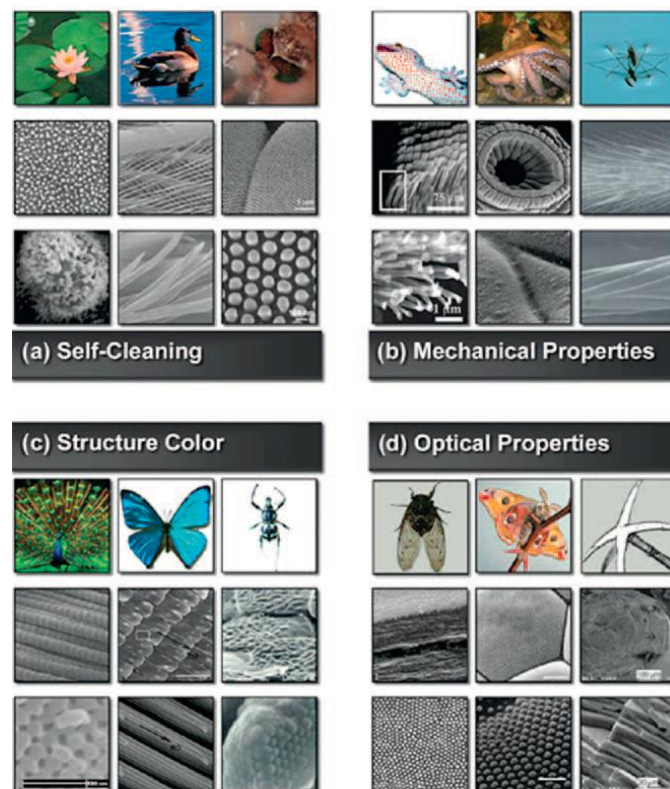


Figure 1.1

Multiscale structure in biology. Four types of interesting biological properties can be found in nature: a) self-cleaning properties: lotus leaf, duck feather, and mosquito eye (from left to right), b) mechanical properties: gecko feet, octopus suckers, and water strider, c) color through structure: peacock feather, butterfly wings, and beetle shells, and d) optical properties: cicada wings, moth compound eyes, and sponge spur. In each case the first row shows a photograph of the biological feature, while the second and third row show scanning electron microscopy (SEM) images of corresponding micro- and nanometer-scale structures¹.

The two basic manufacturing methods techniques for nanostructures is “bottom up” and “top down”. In the first one the desired features are constructed from fundamental building blocks (e.g., self-assembly, sol–gel methods, layer-by-layer deposition), without the need for patterning. In the contrary in the top down approach material is produced in bulk which is then shaped into a finished part through a variety of processes (e.g., casting, molding, rolling). Often the complex hierarchical structures are fabricated by the combination of the above two methods¹.

Various methods have been developed for structuring surfaces and fabrication of hierarchical surfaces. Specifically, by techniques such as electron – beam lithography [E. Martinez et al., 2008⁵] , photolithography [J.-Y. Shiu et al., 2004⁶] , plasma treatments [I. Woodward et al., 2003⁷] , it is possible to integrate, onto the surface topographical features with specific geometry, roughness and orientation in a controlled manner. Figure 1.2 shows SEM micrographs, where the morphological difference is obvious between the flat surface (a), micro- (c), nano- (b) and hierarchical (d) structures.

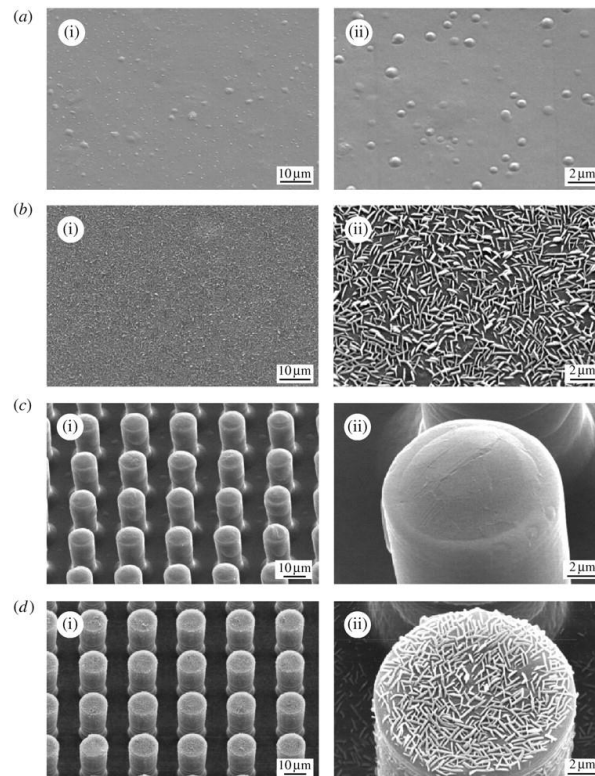


Figure 1.2

SEM images of (a) the flat surface, (b) nanostructure, (c) microstructure and (d) hierarchical structure measured at 45° tilt angle (shown using two magnifications (i)(ii)). All samples are fabricated with epoxy resin coated with 0.2 mg mm⁻² mass of n-hexatriacontane [Bhushan, B. et al., 2009⁸] .

A promising technique for fabrication of micro / nano structures with hierarchical surfaces is irradiation using pulsed laser, with pulse duration lower than a second, i.e. short and ultra-short pulse. Microstructuring using pulsed laser with pulse duration in the range of femtosecond (fs) [Her, T et al., 1998¹⁰], picosecond (ps) [Zorba, V. et al, 2008⁹], or nanosecond (ns) [Zorba, V et al., 2006¹¹] in a special environment irradiation is particularly attractive because it leads to the formation of microconical structures with high aspect ratio on surfaces⁵. The properties that can be tailored with surface structuring via ultra-short fs laser include electrical, mechanical, chemical [Stratakis, E., 2012¹⁶], tribology [Bonse, J. et al, 2014³⁰], wetting [Zorba V. et al., 2008¹³, Hermens, U., 2016³¹] and optical [Rudenko, A et al., 2016¹⁵]. Biomedical applications of artificial hierarchical surfaces include reduction or enhancement of cell adhesion, proliferation or differentiation depending on the types of cells [Simitzi, C. et al, 2015^{13,14}]. With proper setting of the laser parameters (e.g. fluence) and the environment (reactive gas), it is possible the formation of surfaces with different morphologies.

This thesis focuses on the technique of micro / nano structuring surfaces by using ultra-short laser pulses with a pulse duration in the range of fs. Specifically, it refers to irradiation of crystal silicon (Si) and commercially polished steel alloy (40CrMnMoS8-6) surfaces, in the presence of reactive gases. Changing the experimental parameters (such as laser energy, number of pulses, irradiation environment, etc.), (sections 3.1 & 3.4), the final morphology of the surface consists of 3D arrays semi-periodical microconical structures (spikes). At high laser fluence microconical structures are decorated with ledges size of nanometer scale (hierarchical surfaces).

1.1.3 Biomimetic micro/nano functional surfaces for microfluidic applications

What is microfluidics? It is the science and technology of systems that process or manipulate small (10^{-9} to 10^{-18} litres) amounts of fluids, using channels with dimensions of tens to hundreds of micrometres. The field of microfluidics has four parents: molecular analysis, biodefence, molecular biology and microelectronics [Whitesides, G. M., 2006¹⁷]. Microfluidic devices were developed through the study of controlled manipulation of liquids. The most common approach for liquid actuation

in microfluidics, is the manipulation of liquid via surface energy gradients⁴. In parallel with the morphology of a surface, we can tune the chemistry of it. Thus, by depositing chemicals / materials onto structured surfaces, the resulting surfaces can exhibit both stable morphology, and surfaces wettability changing. This is very important for the analysis of the characteristics of micro / nano-structured surfaces, for applications in microfluidics and tissue engineering. The most widely known plant of nature for its special wetting properties, which is a surface model for many scientists [^{3,13}, Koch, K. et al, 1943¹⁸, Guo, Z. et al, 2011¹⁹], who have found ways to represent it artificially, is superhydrophobic Lotus (*Nelumbo nucifera*) leaves, which patented for first time from Wilhelm Barthlott in 1980 [Karthick, B., & Maheshwari, R., 2008²²]. According to this model, we can study the wetting properties of surfaces, via static contact angle measurements (section 4.2.2), and associate them for their potential use in microfluidics applications. Figure 1.3 shows the Lotus leaf (a), a magnification of a water drop on the Lotus leaf (b), SEM images of the surface of the Lotus leaf, which comprises randomly distributed bell-shaped papillae with sizes 5–10 μm (c) decorated with branch like protrusions with sizes of about 150 nm (d).

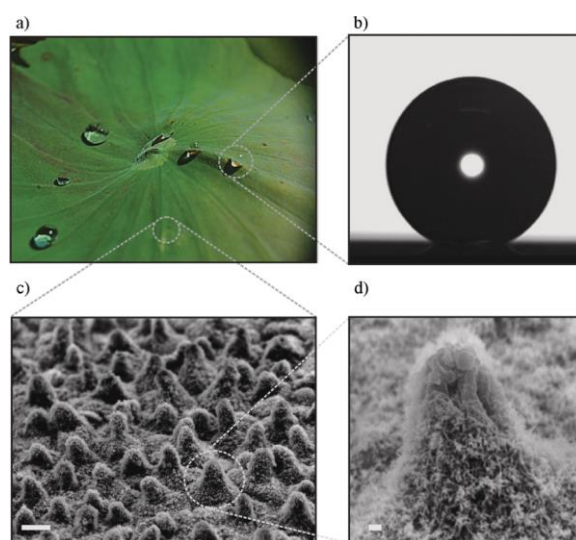


Figure 1.3

a) Picture of water droplets on a *Nelumbo nucifera* (Lotus) leaf. b) Static contact angle measurement of a water droplet of 0.78mm radius on the Lotus leaf surface; the contact angle is $153^{\circ} \pm 1^{\circ}$ c) SEM image of the leaf surface comprising almost-hemispherically-topped papillae with sizes 5–10 μm with surface density of $4.2 \times 10^5 \text{ cm}^{-2}$ (scale bar 10 μm). d) High magnification SEM image of a single papilla depicting branch like protrusions with sizes of about 150nm (scale bar 1 μm)¹³.

The present thesis studies the wetting properties of artificial hierarchical steel surfaces, with specific micro/nano topography (spikes) fabricated via ultra- short fs

laser under reactive gas pressure, by altering surface chemistry with different irradiation environment each time, based on the lotus effect. The ultimate goal is to fabricate hydrophilic and anti-corrosive steel surfaces, with stable behavior for a long time, which has already tried to be succeed [Trdan, U. et al.,2017²⁰, Rajab, F. H. et al.,2018²¹] for anti-corrosion and fluid transport applications. To date, there is no reported work on generating a stable superhydrophilic anti-corrosive metallic surface using a simple, environmentally clean and one step process.

1.1.4 Biomimetic micro/nano functional surfaces for tailoring the optical properties

Since millions of years ago biological systems were using nanometre-scale architectures to produce striking optical effects [Vukusic, P., & Sambles, J. R.,2003²³]. Nature, apart from surfaces with excellent wetting properties, offers surfaces with excellent optical properties (e.g. moth eye [Stuart A. Boden and Darren M. Bagnall,2015²⁶] and wings [Boden, Stuart A, and Darren M Bagnall,2009²⁷], wings of Morpho [Watanabe et al., 2005²⁹] and Greta Oto [Siddique et al.,2015²⁸] butterflies) which are a source of inspiration for scientific research field. Animals such as fish and cephalopods which have chromomorphic (colour-changing) and controllable goniochromic (iridescent-changing) properties, can control the optical properties of their skins for camouflage [Rossiter, J. et al., 2012²⁴]. Also antireflective surfaces composed of biomimetic sub-wavelength structures that employ the ‘moth eye principle’ for reflectance reduction are highly desirable in many optical applications such as solar cells, photodetectors and laser optics [Morhard, C. et al.,2010²⁵]. Some of these surfaces have been fabricated, as shown in Figure 1.4.

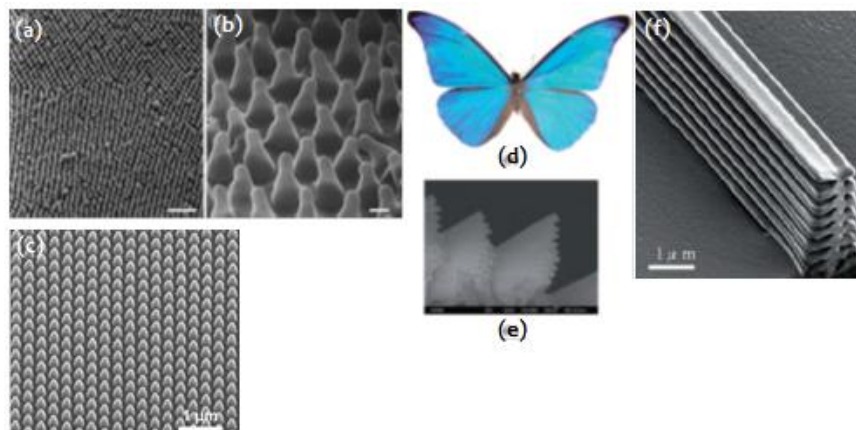


Figure 1.4

Moth-Eye antireflective structures. (left-up): Scanning helium ion microscope images of natural moth-eye structures found on the transparent wing of *Cephonodes hylas* (scale bars: (a) 1 mm and (b) 100 nm) , (left-down): scanning helium ion micrograph of silicon moth-eye structure fabricated using electron-beam lithography and dry etching (c)²⁶.

Morpho-butterfly structures. (right): (d) Top view optical microscope image, (e) Cross-sectional view SEM image, (f) SIM images of Morpho-butterfly-scale quasi-structure fabricated by FIB-CDV²⁹.

The optical phenomena (e.g. structural coloration, broad-range coloration, antireflectivity, strong flicker contrast¹) of these surfaces, stem from their unique and remarkable structure of both micro- and the nano-scale. Fabrication of such surfaces has been performed by various methods and materials [²³⁻²⁹]. In our case, the fabrication of hierarchical surfaces, regards to silicon (Si) surfaces which are irradiated with ultra – short fs laser , in the presence of reactive gas. The optical properties of laser structured Si have been studied [Crouch, C. H. et al.,2004³², Crouch, C. H. et al.,2004³³]. In particular, in this thesis we study the optical properties of ultra – short fs laser structured Si. *We study the effect of different laser irradiation parameters (e.g. laser fluence) and surface functionality (e.g. oxide layers) on the optical response of the fabricated structures, compared with flat silicon, as well as their response to the effect of different sizes gold nanoparticles (AuNPs).*

1.2 Laser - Solid interactions

Since the development of the first lasers, the interaction of laser irradiation with materials has been of scientific and technological interest [Janzén, E et al.,1984³⁴]. Absorption of laser irradiation by a solid can lead to a permanent modification of its surface, causing melting and resolidification, vaporization, or ablation of the material. Laser processing of solids, using both continuous and pulsed lasers, has been studied over the years for different classes of materials including metals [Nolte, S et al.,1997³⁵], semiconductors [Jost, D. et al.,1986³⁶] and dielectrics [Henyk, M et al.,1999³⁷]. Laser light and material interaction mechanisms depend strongly on i) the laser beam parameters (e.g. wavelength, pulse duration, intensity, spatial and temporal coherence, polarization etc.), ii) the physical and chemical properties of the material employed (absorption coefficient, thermal diffusion etc.), iii) as well as on the environmental conditions (vacuum, reactive or non-reactive surrounding medium) [^{9,15}, Barberoglou M. et al.,2013³⁸, Jing-tao³⁹]. In this section we focus on the

fundamental primary and secondary processes that take place upon the interaction of laser pulses with semiconductors, and more specifically with Silicon (Si) and we refer to the proposed mechanisms underlying the spontaneous formation of periodic structures (LIPSS) [J.F.Young et al., 1983⁴⁰] on the surfaces of materials upon laser irradiation in reactive gas ambient. Also, a brief review of structure formation mechanisms on metal surfaces (steel) is mentioned (section 1.2.6). But before dealing with the creation of periodic micro-structures, the basic properties of silicon (Si) and steel are mentioned.

1.2.1 Silicon

Silicon (Si) is the second most abundant element (Clarke number ~26%) on Earth and exists mainly in the oxidized silicate (SiO_2) form. Si sources are neither localized in very specific regions nor are they noble. However, crystalline (c-Si) and amorphous (a-Si) silicons remain the most fundamental, purely inorganic materials used for microelectronics, optoelectronics, integrated-circuit (IC) fabrication and photonics because the lithographic and p-n doping processes are already well-established in industry [Sukumar Basu 2011⁴¹]. Nowadays the use of silicon has been established in the commercial fabrication of many mechanical components, such as switches, filters, oscillators, fluidistic devices, medical and biochips, microphones, accelerometers, gyroscopes, flow detectors, micromirrors, and cantilever sensors [J. Voldman et al., 1999⁴², P. Sievila, 2013⁴³]. Furthermore silicon is widely for materials microfabrication and silicon-based microfabricated substrates with well-defined topographies have been extensively developed for a variety of applications [^{14,29,31}, T. Pearce and J. Williams, 2007⁴⁴, Stratakis E. 2012⁴⁵].

- **Silicon lattice form**

Silicon is used either as bulk material (polycrystalline silicon) or as a thin film (including epitaxial, amorphous, and polysilicon layers) [Hunt LP, 1990⁴⁶]. The different properties of single crystal, polycrystalline and amorphous silicon, which dictate their respective application, are mainly interrelated with the different crystal structure. Two-dimensional representations of the amorphous, polycrystalline, and single-crystal materials are shown in Figure 1.5.

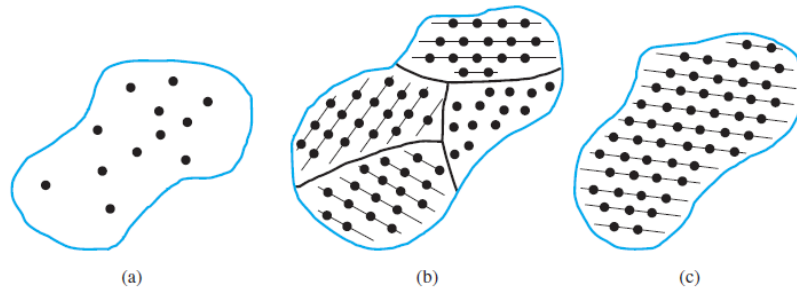


Figure 1.5: Schematics of three general types of forms based on crystal structures: (a) amorphous, (b) polycrystalline, (c) single. [Brown P, 1974⁴⁷]

Two fundamental parameters characterizing Si substrates are the crystallographic orientation of the wafer surface, and the crystallographic direction perpendicular to the wafer flat. Single-crystal Si is one of the simplest three-dimensional lattice system, referred to as the cubic lattice system. Bulk Si is an ideal lattice comprised of an infinite number of repetitive unit cells and an infinite number of cross-sectional planes and lattice directions. Figure 1.6 shows the unit cell of Si crystal, diamond structure, lattice constant (a), and the four nearest neighbor atoms bonding the Si lattice.

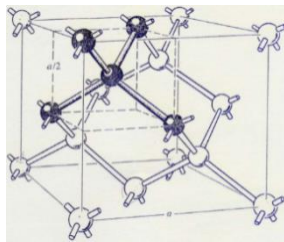


Figure 1.6: Unit cell of the silicon crystal (diamond lattice), is actually two interpenetrating face-centered cubic (fcc) lattices separated by $a/4$ along each axis of the cell

All lattice planes and lattice directions are described by a mathematical description known as the Miller Index. For the cubic lattice system, the direction $[hkl]$ defines a vector direction normal to surface of a particular plane or facet [B.G. Streetman, 1990⁴⁸].

Figure 1.7 shows three common planes, i.e. (100), (110), (111). Monocrystalline is opposed to amorphous silicon, in which the atomic order is limited to a short range order only.

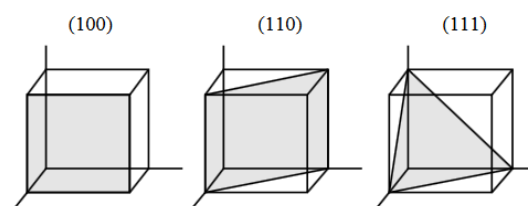


Figure 1.7: Three different crystal orientation (high symmetry) of single-crystal silicon (cubic system): (100), (110) and (111)

Polycrystalline silicon is composed of a large number of single crystals (grains or crystallite). The granules usually have a diameter 100nm-100µm. The boundary separating two small grains or crystals with different crystallographic orientations imposes an interfacial defect. This leads to higher chemical reactivity in these regions. Some important physical and chemical properties of silicon are shown in Table 1.1.

Table 1.1: Physical and chemical properties of silicon (Si).

<i>Physical properties</i>		<i>Chemical properties</i>	
<i>Color</i>	Pure silicon is a hard, dark gray solid	<i>Chemical formula</i>	Si
<i>Phase</i>	Solid	<i>Compounds</i>	Silicon forms compounds with metals (silicides) and with non-metals
<i>Luster</i>	Metallic shine or glow	<i>Oxidation</i>	Combined with oxygen as silica (silicon dioxide, SiO ₂) or with oxygen and metals as silicate minerals. It is stable in air even at elevated temperatures owing to the formation of a protective oxide film
<i>Allotropic*</i>	Silicon has two allotropic forms, a brown amorphous form, and a dark crystalline form	<i>Flammability</i>	Dark-brown crystals that burn in air when ignited
<i>Solubility</i>	Soluble in hydrofluoric acid and alkalis	<i>Reactivity with acids</i>	Dissolves only in a mixture of nitric acid and hydrofluoric acid
<i>Melting point</i>	Melts at 1417°C	Is transparent to long-wavelength infra-red radiation	
<i>Boiling point</i>	Boils at 2600°C		
<i>Conductivity</i>	Semi-conductor		

*Allotropic – Allotropes: Forms of an element with different physical and chemical properties occurring in two or more crystalline forms in the same physical state

• Energy bands of Si

A crystalline solid (e.g. silicon) consists of atoms arranged in a repetitive structure. Specifically, each silicon atom is surrounded by four nearest neighbors as illustrated by the shaded cluster in Figure 1.6. Recall that electrons in an atom occupy discrete energy levels as shown in Figure 1.8(a). If two atoms are in close proximity, each energy level will split into two due to the Pauli exclusion principle, that states that each quantum state can be occupied by no more than one electron in an electron system such as an atom molecule, or crystal. When many atoms are brought into close proximity as in a crystal, the discrete energy levels are replaced with bands of energy states separated by gaps between the bands as shown in Figure 1.8(b). Naturally, the electrons tend to fill up the low energy bands first. Between the (basically) totally filled and totally empty bands lie two bands that are only nearly filled and nearly empty as shown in Fig. 1.8(b). These

energy bands are the valence band (top nearly filled band with electrons) and the conduction band (the lowest nearly empty band). These bands are separated by a region which designates energies that the electrons in the solid cannot possess. This region is called the forbidden gap, or bandgap E_g . This is the energy difference between the maximum valence band energy E_v and the minimum conduction band energy E_c , as shown in Figure 1.9. The concept of E_g , is very important for the laser-solid interactions (section 1.2.3).

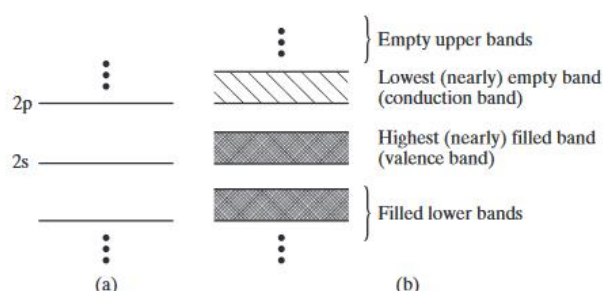


Figure 1.8

The discrete energy states of a Si atom (a) are replaced by the energy bands in a Si crystal (b).

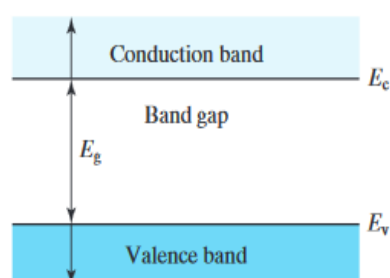


Figure 1.9

The energy band diagram of a semiconductor

- **Silicon oxide layer (SiO_2)**

Semiconducting surfaces have been investigated for many years. Due to its dominant role in silicon devices technologies (e.g. IC industry) [F. J. Himpsel et al., 1988⁴⁹, M. Razeghi, 2010⁵⁰] and because of its good electronic properties, as well as Si/ SiO_2 interface, the above SiO_2 properties has been intensively studied in the last decades. In contrast to other materials which suffer from one or more problems, SiO_2 offers a lot of desired characteristics and advantages [A.Hierlemann⁵¹]:

1. Excellent electrical insulator with a high dielectric strength and wide band gap (Resistivity $> 1 \times 10^{20} \Omega\text{cm}$, Energy Gap $\sim 9 \text{ eV}$)
2. High breakdown electric field ($> 10 \text{ MV/cm}$)
3. Dielectric constant SiO_2 : 3.9 (whereas Si_3N_4 : 7; Si: 11.9)
4. Stable and reproducible SiO_2 interface
5. Conformal oxide growth on exposed Si surface
6. SiO_2 good diffusion mask for common dopants: B, P, As, Sb

7. Very good etching selectivity between Si and SiO₂
8. SiO₂ has a high-temperature stability (up to 1600°C)

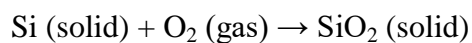
According to these properties of SiO₂ and Si/SiO₂ interface, the silicon oxide layer (SiO₂) is a high quality electrically insulating layer on the silicon surface, serving as a dielectric in numerous devices that can also be a preferential masking layer in many steps during device fabrication [Logofatu C. et al., 2011⁵²].

Among all the various oxidation methods (thermal oxidation, electrochemical anodization and plasma enhanced chemical vaporization deposition), only thermal oxidation in a resistance-heated oxidation furnace can provide the highest-quality oxides having the lowest interface trap densities. Thermal oxidation of Silicon can be performed in two ways: 1. Dry and 2. Wet oxidation process. A typical oxidation growth cycle consists of dry-wet-dry oxidations, where most of the oxide is grown in the wet oxidation phase⁵².

1. Dry thermal oxidation process

Dry oxidation uses dry oxygen. Oxidation process is slow e.g., 50 nm/h at 1000°C and results in more dense and high-precision thin oxide layers. The chemical

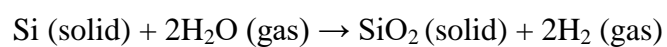
reaction describing thermal oxidation of silicon in dry oxygen is:



Dry thermal oxidation process is usually used in a device structure because of its good Si-SiO₂ interface characteristics.

2. Wet thermal oxidation process

Wet process uses (pyrogenic) water vapor. The oxidation process is fast, e.g., 400 nm/h at 1000°C and therefore is mainly used for thick oxide formation applications. The chemical reaction is the following:



In the wet oxidation method, the water vapor introduced into the furnace system is usually created by passing a carrier gas into a container with ultra pure water and

maintained at a constant temperature below its boiling point (100°C). Wet oxidation results in much more rapid growth and is used mostly for thicker masking oxide layers. In this thesis, silicon substrates have been processed via dry thermal oxidation.

For both means of oxidation, the high temperature allows the oxygen to diffuse easily through the silicon dioxide and the silicon is consumed as the oxide grows. SiO_2 layer incorporates silicon consumed from the substrate and oxygen supplied from the ambient. Thus the silicon oxide grows both down into the wafer and up out of it, so the total thickness increases [B.E.Deal and A.S.Grove,1965⁵³], as shown in Figure 1.10.

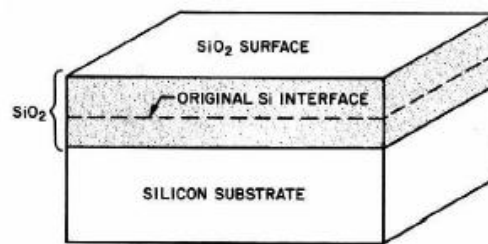


Figure 1.10 : Schematic of the thermal oxide (SiO_2) formation [S. M. Sze, 2002⁵⁴]

Kinetics of growth

A model elucidating the kinetics of oxide growth has been developed by Deal and Grove⁵³, where it is assumed that oxidation proceeds by an inward movement of the oxidant species rather than an outward movement of silicon. At the initial stage of oxidation, the oxidizing species (oxygen or water vapor) reacts with silicon atoms at the surface. This results in growth of a thin SiO_2 layer. Now, in order to oxidize Si, the oxidizing species has to diffuse through the SiO_2 layer of the Si- SiO_2 interface. More specifically, the transported species must go through the following stages:

1. It is transported from the bulk of the oxidizing gas to the outer surface where it reacts or is adsorbed.
2. It is transported across the oxide film towards the silicon
3. It reacts at the silicon surface to form a new layer of SiO_2

The model is generally valid for temperatures between 700 and 1300°C , partial pressure between 0.2 and 1.0 atmosphere, and oxide thickness between 30 nm and 2000 nm for oxygen and water ambient. The model is valid for (111), (100) single crystal silicon, and polysilicon. According to the equations of this model, which are

analyzed by B. Deal and A. Grove, 1965.⁵³, oxidation rate charts (different for dry and wet oxidation) have been developed based on which, oxide thickness layer for the optimum oxidation parameters can be predicted. However, the most reliable technique, to measure the SiO₂ thickness layer is ellipsometry (section 3.5.4).

SiO₂ layer structure

Regarding its structure, SiO₂ can be described as a three-dimensional network constructed from tetrahedral entities which are centered on a silicon atom. The four corners of the tetrahedral structure could be either silicon or oxygen atoms. It is accepted that an oxygen atom is bonded by two silicon atoms and never with another oxygen atom. The length of the Si-O bond is 1.62 Å while the distance of the bond between oxygen ions is 2.26 Å (Figure 1.11(a)) and Si-Si bond distance depends on the particular form of SiO₂ and is about 3.1 Å. The angle formed by the Si-O bonds in the Si-O-Si bridge is 144° [Carrier P. et al., 2002⁵⁵], and the angle between two oxygen atoms is 109.5°. Taking into account the fact that the silicon atom is four-coordinated and the oxygen is two-coordinated, concludes that, oxygen atoms are involved in Si-O-Si bridges, which means two Si-O bonds and Si atoms will contribute to Si-Si and Si-O-Si bonds.

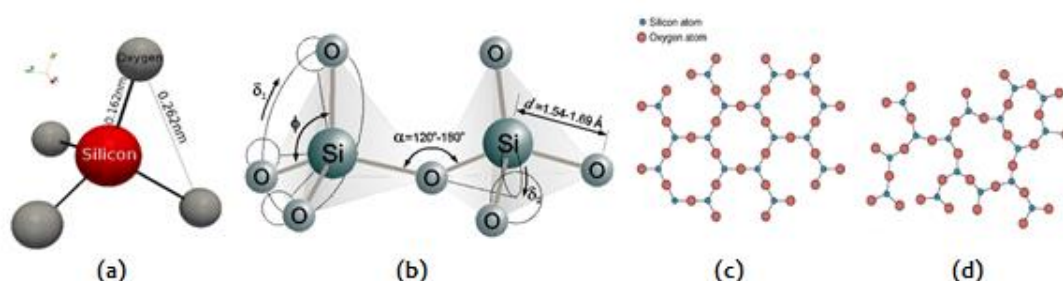


Figure 1.11 : (a)Structural unit of SiO₂ , (b)Regular silica structure: Si-O bond length (d), tetrahedral angle (φ), the Si-O-Si bridge bond angle (α), bond torsion angles (δ_1 , δ_2), [Henderson and Baker, 2002⁵⁷], (c) Quartz crystal lattice (2D), (d) Amorphous SiO₂ (2D)

The six-membered ring structure of SiO₂ is presented in Figure 1.11(d). In an ideal network the vertices of the tetrahedra are joined by a common oxygen atom called bridging oxygen (i.e. O atoms that bond to two silicon atoms). In the amorphous forms of SiO₂ (Figure 1.11(d)), some non-bridging oxygen atoms can also exist. These phases are often named, fused silica. Crystalline forms of SiO₂, such as quartz contain only binding oxygen bonds. The various crystalline and amorphous forms of

SiO₂ arise due to the ability of the bridging oxygen bonds to rotate, allowing the position of one tetrahedron to move with respect to its neighbors. This same rotation allows the material to lose long-range order and hence become amorphous. The rotation and the ability to vary the angle of the Si-O-Si bond from 120° to 180° (Figure 1.11(b)) with only a little change in energy play an important role in matching amorphous SiO₂ with crystalline silicon without breaking bonds. Dry oxides having larger ratio of bridging to non-bridging sites as compared to wet oxides, are thus “more stable”. The chemical bonding configurations are important basis for understanding the electronic states of the fabricated silicon oxides. In order to understand the chemical and electronic structures of the Si-SiO₂ interface, the Si-SiO₂ interface has been studied by various techniques such as X-ray photoelectron spectroscopy (XPS)⁵⁵. The conclusion was that, while the oxide layer grows, it is progressively less and less influenced by the properties of the interface.

Native oxide layer

Another important issue when dealing with silicon is the so called native oxide layer, which is built up on the surface when a clean Si surface is exposed to atmosphere at room temperature. It is of great importance, because it may influence the thermal oxidation kinetics. Native oxide films on Si surfaces prevent the low-temperature growth of high-quality epitaxial Si films and precise control of the thickness and electrical properties of very thin gate oxide films, plus give an increase of the contact resistance for via-holes of a small area. Native oxides serve as source of impurities to diffuse into the silicon and produce defects in succeeding high-temperature processes. The presence of native oxide film on silicon surfaces degrades the ability to control the quality of device fabrication processing and the performance and reliability of semiconductor devices themselves. The detection of the native oxide layer takes place through X-ray Photoelectron Spectroscopy (XPS). The oxidation mechanism of Si in air at room temperature (RT) is entirely different from the thermal oxidation mechanism. The following model [M. Morita et al., 1990⁵⁶] is proposed for the oxidation of Si at room temperature (Figure 1.12):

1. Si atoms at a cleaned wafer surface are terminated by hydrogen (Fig. 1.12(a)). In our case, the Si wafers were cleaned by aqueous hydrofluoric acid (HF).

2. The oxygen species (O) are expected to break preferentially the $\text{Si}_{\text{bulk}}=\text{Si}(\text{H})_2$ backbonds rather than the Si-H bonds on the surface at the initial stage. ($\text{Si}_{\text{bulk}}-\text{O}-\text{Si}(\text{H})_2$ bonds are formed- Fig. 1.12b).
3. After all Si atoms of the top layer are oxidized, the chemical structure of the second monolayer are broken by subsequent insertion of O_2 (Fig. 1.12d).
4. In this way, a layer-by layer growth of the native oxide film takes place on Si surfaces exposed to air at RT.
5. The overlayer structure converts to the amorphous phase.
6. The remaining $\text{O}-\text{Si}(\text{H})_2$ bonds on top layer cause hydrophobic behavior of the surface, which can be observed during the initial phase of native oxidation in air.
7. The Si-H bonds on the surface are oxidized only after completion of the backbond oxidation, and silanol groups SiOH are respectively formed, which introduce polarity (and the surface becomes less hydrophobic).

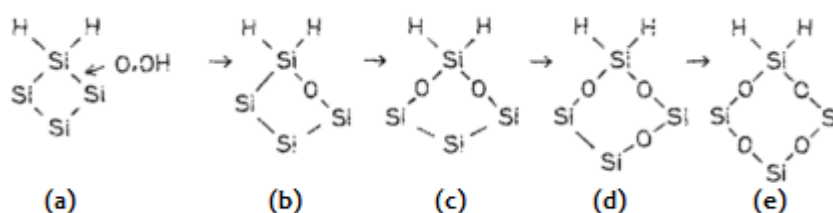


Figure 1.12 : A model of native oxide growth in air ⁵⁶

1.2.2 Steel

Metallic materials, such as steels, are normally combinations of metallic elements. They have large numbers of nonlocalized electrons; that is, these electrons are not bound to particular atoms. Many properties of metals are directly attributable to these electrons. Metals are extremely good conductors of electricity and heat and are not transparent to visible light; a polished metal surface has a lustrous appearance. Furthermore, metals are quite strong, yet deformable, which accounts for their extensive use in structural applications [William D. Callister, 2001⁵⁸].

Steels are iron-carbon alloys that may contain appreciable concentrations of other alloying elements; there are thousands of alloys that have different compositions

and/or heat treatments. The mechanical properties are sensitive to the content of carbon, which is normally less than 1.0 wt%. Some of the more common steels are classified according to carbon concentration, namely, into low-, medium-, and high-carbon types. Subclasses also exist within each group according to the concentration of other alloying elements. Plain carbon steels contain only residual concentrations of impurities other than carbon and a little manganese. For *alloy steels*, more alloying elements are intentionally added in specific concentrations. A taxonomic classification scheme for the various ferrous alloys is presented in Figure 1.13.

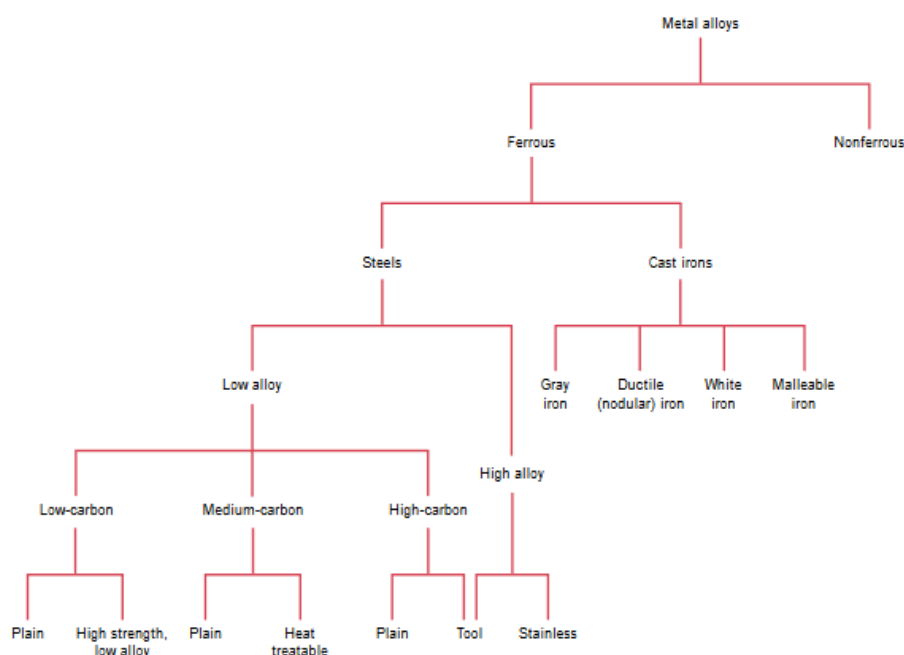


Figure 1.13: Classification scheme for the various ferrous alloys⁵⁸

The kind of steel that we focused on, is the *tool steels*. The tool and die steels are high-carbon alloys, usually containing chromium, vanadium, tungsten, and molybdenum. These alloying elements combine with carbon to form very hard and wear-resistant carbide compounds. The primary properties of tool steels are toughness, wear resistance, hardness and heat resistance. These steels are utilized as cutting tools and dies for forming and shaping materials, as well as in knives, razors, hacksaw blades, springs, and high-strength wire⁵⁸. Durability and *corrosion resistance* are of prime importance when a metal will be exposed to weather.

- **Energy bands of metals**

Every solid has its own characteristic energy band structure. In order for a material to be conductive, such as metals, both free electrons and empty states must be available. Metals have free electrons and partially filled valence bands, therefore they are highly conductive. In conductors, the valence band is either not fully occupied with electrons, or the filled valence band overlaps with the empty conduction band. In general, both states occur at the same time, the electrons can therefore move inside the partially filled valence band or inside the two overlapping bands. Energy band is a range of allowed electron energies. The energy band in a metal is only partially filled with electrons. Metals have overlapping valence and conduction bands. This means that E_g is equal to zero. Energy provided by an electric field is sufficient to excite many electrons into conducting states. Also in metals, valence electrons form an “electron gas” that are not bound to any particular ion. By alloying procedures conductivity decreases.

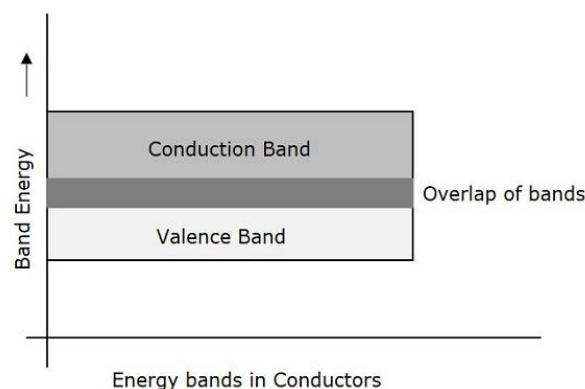


Figure 1.14: Illustration of energy bands in conductors

- **Corrosion of steel**

Any material made with iron that is exposed to both oxygen and water will rust. Because steel is made almost entirely of iron, it is the most highly manufactured man made material that is subject to rust. After the element Helium, elements like having 8 electrons in their outer shell, and will borrow electrons from other elements to achieve that level. Water, for example is made of an oxygen atom with six outer electrons and two hydrogen atoms that have one electron each. Through the borrowing and sharing

of electrons in a reduction reaction, $\text{FeO}(\text{OH})$ (the most common form of rust) is created.

When any type of steel rusts, including steel, it undergoes a chemical reaction called corrosion. During that process of being exposed to air and water while being left outside or in the elements for an extended period of time, a variety of different types of rusts can form, but the most common form is Fe_2O_3 . Rust only forms on the outside of a metal surface because it requires exposure of oxygen and water to rust.

Does steel rust in saltwater?

Steel rusts faster in saltwater than it does in freshwater. The presence of salt acts as a catalyst, accelerating the corrosion chemical reaction process. Salt is an electrolyte, and it contributes ions into water. Steel will rust immediately when being exposed to moisture and air. How quickly steel rusts typically depends on how much steel is exposed to moisture and air, the levels of both moisture and air, and whether or not any protective coatings are present (e.g. chromium oxide).

Coating steel with a thin layer of chromium oxide, is one of the most widely manufactured corrosion resistant procedures in the world. The chromium acts mostly to prevent the oxidation process of corrosion from occurring, as it acts as a barrier of oxygen from reaching the iron of the steel. Chromium also gives the steel a clean and *polished* appearance that makes it practical for a wide range of applications, but it is not an environmentally clean procedure. Also, passivation of steel surface (e.g. nitric layer) is a promising way to avoid the surface corrosion.

Commercially polished steel alloy samples 40CrMnMoS8-6 (1.2312), supplied by ML Engraving, were used throughout the study. The measured chemical composition of the material consisted of (0.35-0.48) wt.% C, (0.30-0.50) wt.% Si, (1.40-1.60) wt % Mn, (0.03) wt % P, (0.05-0.10) wt % S, (1.80-2.00) wt % Cr and (0.15-0.25) wt % Mo. Sulphur (S) additive promote high dimensional stability.

1.2.3 Fundamental processes of laser – matter interaction

The interpretation of the basic interaction mechanisms between the intense light of a laser beam and matter, is an aspect of increasing interest³⁵. Controlling the light-

matter interactions is crucial for the success and scalability of materials-processing applications¹⁶. In our case, this is achieved by surface irradiation with ultra-short laser pulses because pulse duration is a critical parameter for material processing. In order to understand and control the material response after/upon laser irradiation, the laser-matter interactions have to be taken into consideration.

1.2.3.1 Primary processes – Absorption mechanisms

Surface modification of materials by means of pulsed laser light requires the deposition of a certain amount of energy absorbed by the material. Different kinds of surface modification can be attained, depending on the laser parameters including energy, temporal and spatial distribution of the beam, and pulse repetition rate. Primary absorption processes involving interband transitions of electrons are: **(a)** single photon absorption, **(b)** multiphoton absorption, **(c)** interband transitions by free-carrier excitation and **(d)** impact ionization. Detailed information on these processes can be found elsewhere [E. Magoulakis et al., 2010⁵⁹]. This process increases the number of free carriers in the conduction band. If the laser intensity is high enough, multi-photon absorption and impact ionization can lead to optical breakdown, which produces a plasma [A.C. Tien, 1999⁶⁰].

So, the initial interaction of laser pulses with a *semiconducting* material is the excitation of electrons; upon photon absorption electrons are excited from their equilibrium states into higher-lying unoccupied states. More specifically, the energy band gap of *silicon* ($E_{g(Si)}$: 1 to 1.5 eV) is less than 3.0 eV, which means that Si absorbs energy through photoionization when irradiating in Vis-IR spectrum because the photon energy is bigger than the energy bandgap⁵⁹.

1.2.3.2 Secondary processes – Energy relaxation

Following the primary absorption mechanisms the energy absorbed by the electron is relaxed through a variety of processes which can eventually end in modification of the material structure. Figure 1.15 summarizes the most important processes involved after the absorption of the laser energy, its redistribution and transport through the

target and the resulting structural and thermal effects, together with their typical timescales.

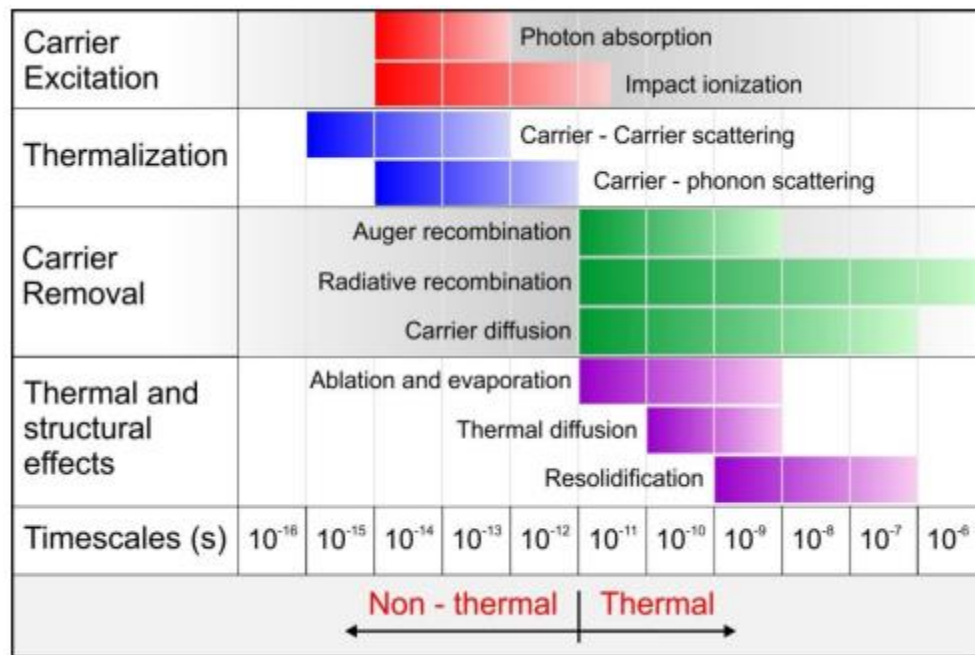


Figure 1.15: Processes (and associated timescales) taking place in the target following the absorption of the laser pulse⁵⁹

The governing processes are the following:

(i) Carrier excitation: Carrier (electrons in metals or electron-holes in semiconductors) excitation is the movement of an electron to a higher energy state due to absorption of photons by a laser beam. Single or multiphoton absorption are the dominant mechanisms for exciting electrons in the valence band provided that the energy gap is smaller or greater respectively than the photon energy. If some of the carriers are excited well above the band gap, impact ionization can generate additional excited states.

(ii) Thermalization: On a time scale of about $10^{-14} - 10^{-12}$ sec described as the electron phonon relaxation time, the initial energy distributed among the electrons is transferred to the lattice via carrier-carrier and carrier-phonon scattering.

(iii) Carrier removal: Once the carriers and the lattice are in equilibrium, the material is at a well-defined temperature. Although the carrier distribution has the same temperature as the lattice, there is an excess of free carriers compared to that in the thermal equilibrium. These are removed by recombination or carrier diffusion processes.

(iv) Thermal and structural effects: On the time scale of 10^{-11} sec and below carriers and lattice come to an equilibrium temperature and heat is diffused from the material's surface to the bulk. If the laser pulse intensity exceeds the melting or boiling point thresholds, melting or vaporization of the material occurs. As the deposited optical energy is converted to kinetic energy of the lattice ions, material removal via ablation can occur in the form of individual atoms, ions, molecules or clusters. Finally solidification of the material occurs in timescales from nanosecond through microseconds.

The distinct line at about 10^{-12} - 10^{-11} sec distinguishes the regimes between nonthermal and thermal processes. Mechanisms leading to structural modifications using picosecond (10^{-12} sec) and longer laser pulses are predominantly thermal. By contrast, exposure to ultrashort (femtosecond 10^{-15} sec) pulses leads to a different type of modification.

So, why to use an ultra-short femto-second pulse laser?

Nanosecond laser ablation of materials occurs due to melt expulsion driven by the vapour pressure and the recoil pressure of light, so the ablated area on the surface of the material target is not precise and uniform. Furthermore, nanosecond laser ablation creates a heat-affected zone (HAZ) (Figure 1.16) [Lucas, L. and J. Zhang , 2012⁶¹].

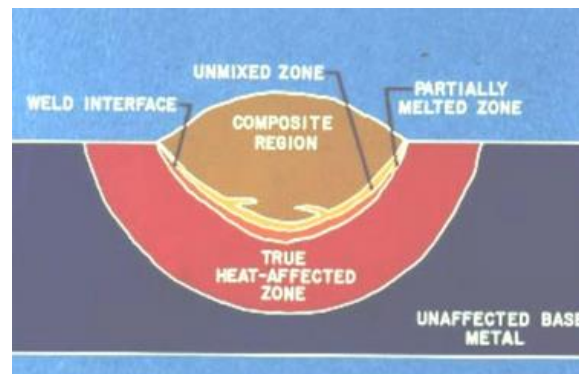


Figure 1.16: Illustration of HAZ on a metal target

As illustrated in Figure 1.15, for pulse durations that are significantly less than electron-to-lattice (ions) non-thermal pathways may be accessed that take place on a timescale shorter than a picosecond, hence before thermal processes are initiated. In the case of ultra-short laser pulses (pulse duration less than a few picoseconds (10^{-12} seconds)), pulse duration is considerably shorter than the timescale required for

energy transfer between the lattice and the free electrons of the material target. The laser energy is absorbed by the electrons, leaving the ions cold, and only after the laser pulse is gone thermalization takes place. As a result, very high temperatures and pressures are produced at a very shallow depth in the range of microns. However, the absorbed energy heats the material very quickly past the melting point, directly to the vapor phase with its high kinetic energy. The material is removed by direct vaporization away from the surface without formation of a recast layer. This provides negligible HAZ and very fine, sharp features. Also, the intensity of a femtosecond pulse is high enough to drive highly nonlinear absorption processes in materials that do not normally absorb at the laser wavelength⁶¹.

There are two major mechanisms to explain material removal by laser ablation: thermal vaporisation, and the occurrence of a Coulomb explosion (section 1.2.4.1). As shown in Figure 1.17, the long-pulse lasers have more heat-affected zones and shock waves in comparison with the shorter picosecond and femtosecond lasers.

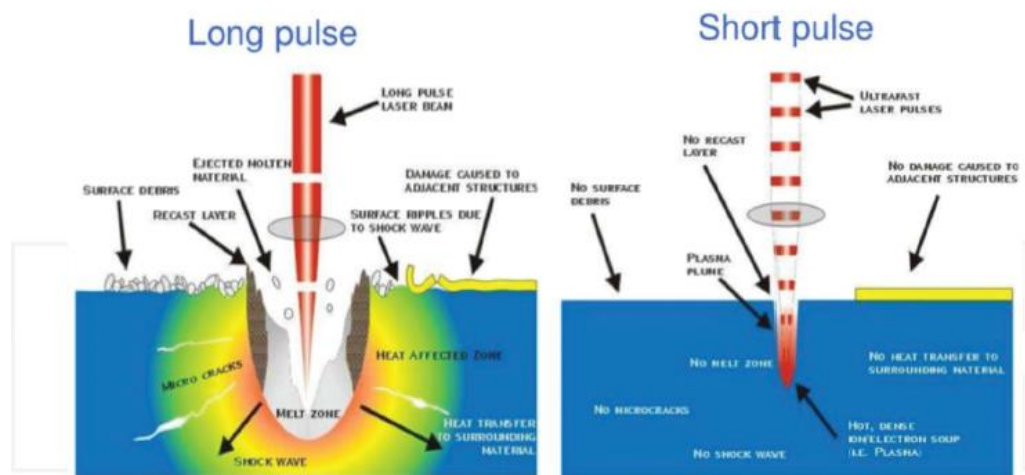


Figure 1.17: Long-pulse (left) and ultrafast-pulse (right) laser interaction with target material.

So by using ultrafast lasers with pulse duration less than sub-picosecond, we can limit the thermalization and thermal diffusion, caused by the relaxation process, in order to avoid the ablation of clusters and evaporation of material and to encourage the formation of controllable periodic structures in micro and nano scale [Y.C. Koji Sugioka, 2013⁶²].

1.2.4 Laser induced periodic surface structures (LIPSS)

Researchers that study the laser-matter interaction are familiar with almost a universal phenomenon occurring close to the damage threshold of a material. This is the so called “*Laser induced periodic surface structures*” (LIPSS) or “*ripples*” and their formation by a single laser beam can appear on any material absorbing radiation, regardless of its dielectric constant⁴⁰. LIPSS is a form of laser induced surface modification which appears to be spatially periodic in nature, and which occurs on a wide variety of both opaque and transparent materials.

Birnbaum [M. Birnbaum,1965⁶³] was the first to observe the formation of LIPSS after irradiation of semiconductor surfaces with a CW Ruby laser. He explained this ripple formation as the result of light diffraction effects at the focal region. These patterns exhibit a grating-like morphology with a periodicity close to the laser wavelength and have been observed at the surface of many materials including semiconductors [D. C. Emmony et. al.,1973⁶⁴, H. J. Leamy et. al.,1978⁶⁵, P. M. Fauchet et al.,1981⁶⁶], metals [T. E. Zavecz and M. A. Saifi,1975⁶⁷, J. C. Koo and R. E. Slusher,1976⁶⁸, N. R. Isenor,1977⁶⁹, A. K. Jain et. al.,1981⁷⁰] and dielectrics [P. A. Temple and M. J. Soileau,1981⁷¹]. For a normal incident laser beam ripples are formed perpendicular to the electric field *polarization*.

Light waves are recognized as electromagnetic transverse waves, i.e., with transverse oscillations of the electric and magnetic field. The direction of polarization is taken to be the direction of the electric field oscillations (i.e., not the magnetic ones).

For circular polarized light, no ripples are observed. Additionally, the number of laser shots is inversely proportional to periodicity [M. Huang et al.,2009⁷², A. Latif et al.,2009⁷³]. Ripples can be produced by a single or many laser shots and are independent of the irradiation atmosphere and of the crystallographic direction of the surface.

- *Low-Spatial Frequency-Ripples (LSFR)*

In 1973⁶⁴ researchers suggested that the interference between the incident and a scattered surface wave, may explain the formation of the observed ripples. Ripple formation leads to low spatial frequency ripples (LSFR) perpendicular (or parallel to the laser polarization, depending on the material [Mezera and Romer,2019⁸⁸]) to the

laser beam polarization, where the periodicity (spatial interval between the repeating structures (Λ)) is near to the laser wavelength (λ) ($\Lambda \sim \lambda$). The ripple periodicity Λ , due to the proposed mechanism was calculated to be equal to

$$\Lambda = \frac{\lambda}{1 \pm \sin\theta} \quad (eq. 1)$$

where λ is the laser wavelength, θ is the angle of the incidence laser beam and the \pm accounts for the scattered wave co-propagating and counter-propagating to the surface projection of the incident wave. For normal incidence, Eq.1 gives $\Lambda \sim \lambda$, therefore such ripples are called ‘‘Low-Spatial-Frequency-Ripples (LSFR)’’. LSFRs (coherent structures) are directly related to the coherence, the wavelength and the polarization of the laser light [D. Bäuerle, 2000⁷⁴].

- *High-Spatial Frequency-Ripples (HSFR)*

Despite the successful interpretation of LSFR formation, a large number of experimental observations showed that ripple periodicity can be much smaller than the laser wavelength ($\Lambda \ll \lambda$); in this case we have ‘‘High-Spatial-Frequency-Ripples (HSFR)’’, which formation could not be explained by the previous mentioned mechanism, as described in Eq.1. A widely accepted mechanism that accounts for HSFR (coherent structures) formation is based on the laser induced excitation of surface plasmon waves [S. Sakabe et al., 2009⁷⁶]. In this case, the Λ depends only on the frequency (electron density) of the surface plasmon wave (section 1.2.4.1). Directionality of HSFRs can be parallel or perpendicular to the laser beam polarization depending on the material [Sabri Alamri et al., 2019⁸⁹].

Apart from the ripples can be also formed other structures on a material surface, like *microgrooves* and *spikes*. The formation of *microgrooves* leads to structures with periodicity larger than the laser wavelength ($\Lambda > \lambda$) [Tsibidis George D. et al., 2015⁷⁵]. In case of micro-conical formation (MCs) or *spikes*, structures are characterized as *supra-wavelength quasi-periodic surface structures*, which means that the periodicity is markedly, even multiple times, higher than the laser wavelength ($\Lambda \gg \lambda$) [Tsibidis George D. et al., 2016⁷⁸]. Spikes are non-coherent structures that are not directly related to any spatial periodicity of the energy input caused by interference phenomena; their period is related to the laser-beam intensity and the ambient gas

pressure, when such is used⁷⁴, rather than the laser wavelength and polarization. They appear at higher intensities as compared to coherent structures [S. Clark and D.C. Emmony, 1989⁷⁷]. Figure 1.18 shows the morphological changes induced on a Si surface following fs pulse laser irradiation.

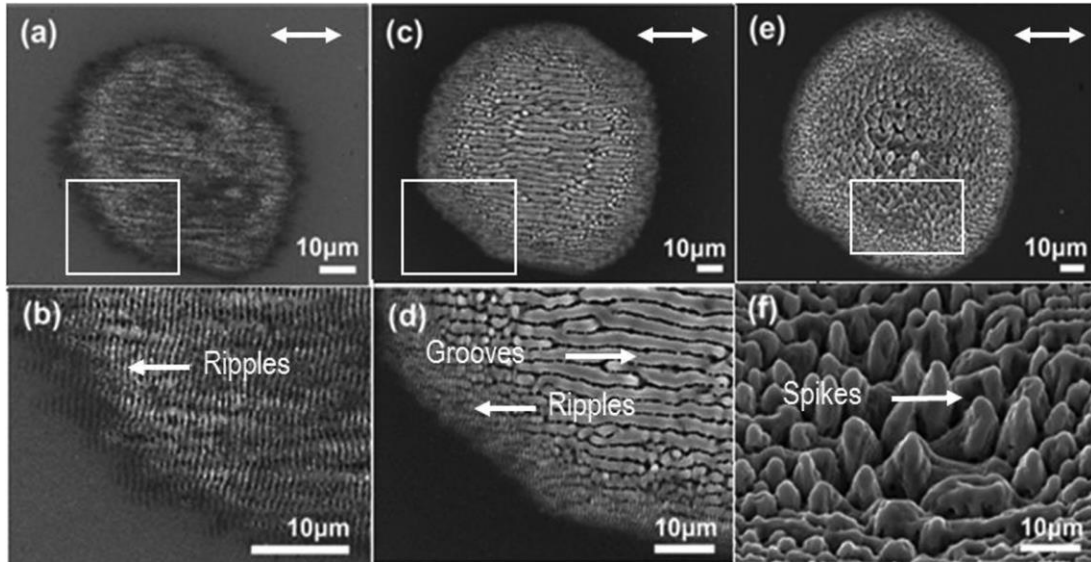


Figure 1.18: Morphological changes induced on a Si surface following irradiation with NP = 10 (a), 40 (c), and 100 (e) pulses, laser beam wavelength $\lambda = 800$ nm, where (b), (d), and (f) provide an enlarged area. Double-ended arrows indicate the laser beam polarization⁷⁵.

1.2.4.1 Surface plasmon waves

In 1907 Zenneck⁷⁹ proposed that electromagnetic waves in the radiofrequency regime can ride along the planar interface between air and either ground or water. This idea was later reintroduced in 1957 by R. H. Ritchie⁸⁰ to the visible portion of the electromagnetic spectrum at the interface of a metal and a dielectric, leading to the concept of *surface-plasmon-polaritons S-PP*.

Surface plasmons (S-P), are coherent electron oscillations that exist at the interface between any two materials (Figure 1.19) (e.g. a metal-dielectric interface, such as a metal sheet in air). S-Ps have lower energy than bulk (or volume) plasmons.

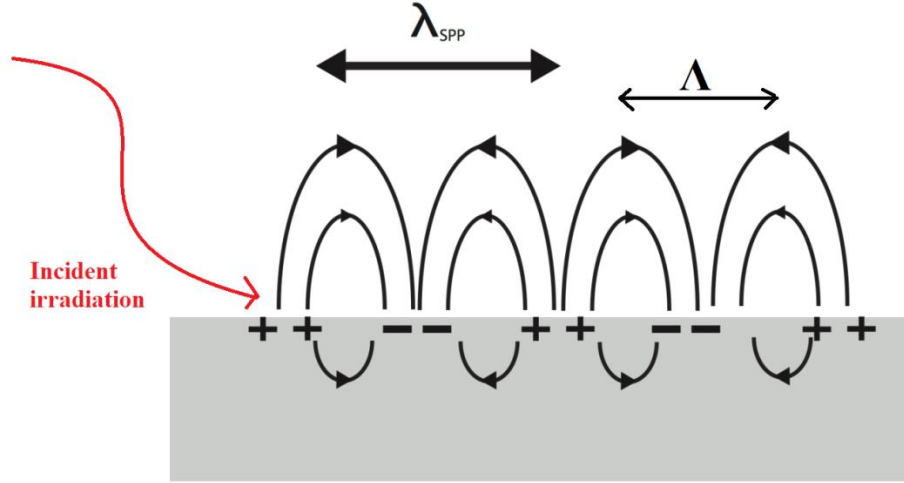


Figure 1.19: Schematic representation of an interference of the incident beam (red line) with the surface plasmon wave (black line) for a metal - dielectric interface. The charge density oscillations and associated electromagnetic fields are called surface plasmon-polariton waves.

When S-Ps couple with a photon, the resulting excitation is called surface plasmon polariton (S-PP). This S-PP can propagate along the surface of a metal until energy is lost either via absorption in the metal or radiation into free-space. S-Ps can be excited by both electrons and photons. Due to the laser-induced excitation of a large number of electrons in the conduction band, semiconducting surfaces irradiated by ultrashort pulsed laser, at fluences close to the damage threshold, also exhibit metallic behaviour. Therefore S-PPs can potentially be excited along a semiconductor - dielectric interface as well.

The mechanism for the formation of periodic structures, due to the S-P waves excitation, propose that the interference of the incident laser beam with the propagating plasmon wave gives rise to the generation of local, periodically charged areas onto the material surface. Areas that become positively charged are exploded towards free space by the Coulomb repulsive force (Coulomb explosion); consequently, a thin layer located at such areas is ablated and a periodic pattern is imprinted. According to the above mechanism, the periodicity of the surface patterns depends only on the frequency (electron density) of the surface plasmon wave⁷⁶, as we already mentioned.

Figure 1.19 illustrates the above mechanism. During material heating and melting process, the interference of the incident beam with the surface plasmon wave gives

rise to periodic fringes (black colour) which are subsequently “printed” on the material after resolidification. Therefore, the structures formed exhibit the periodicity of the interference pattern.

1.2.5 Surface structuring of silicon via ultrashort – pulsed laser processing

The irradiation of a solid surface via ultra-short fs pulsed laser, leading to microstructures of different morphologies. The resulting structures/ morphology depend on the material (e.g. optical and thermal properties), laser source (such as laser fluence, repetition rate, wavelength, etc.) and irradiation environment (liquid, vacuum or reactive gas). By irradiating Si surfaces with fs laser pulses above the ablation threshold in the presence of a variety of background gases, quasi-periodic sharp conical micrometer-sized spikes are formed. High-intensity nanosecond pulses can induce the formation of much larger conical microstructures [A. Pedraza et al., 1999⁸¹, S. Dolgaev et al., 2001⁸²].

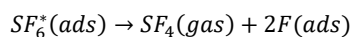
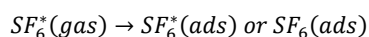
Microstructuring by ultra-short pulsed lasers is an especially attractive approach, because it leads to the formation of arrays of high-aspect ratio microcones (MCs) on solid surfaces. In particular, fs lasers allow patterning through non-linear absorption processes, providing excellent control over the regularity and uniformity of 3D micron and submicron features¹⁶. This method exploits a number of phenomena taking place under the action of intense pulsed laser irradiation of crystalline Si in the presence of a reactive gas, in order to induce morphological, structural and compositional modifications on its surface. The resulting structures, apart from their unique (conical) morphology, they also exhibit improved optical, electronic and wetting response. Proper tuning of the laser (such as laser fluence, repetition rate, etc.) and reactive gas parameters (such as pressure) can lead to the formation of structures with different morphologies [Zorba V. et al., 2006⁸³]. One of the most useful properties of ultrafast laser induced modification is the limited size of the affected volume, resulting in perfect control of structures fabrication in micro- and submicron scales, for reasons which explained in section 1.2.3.2.

The role of reactive gas

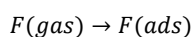
The first objective of the present thesis was the fabrication of hierarchical silicon structures. One way to achieve the fabrication of double roughness surfaces (micro- and nano- scales), is the irradiation via ultra-short fs pulsed laser in presence of a gas which reacts with the initiate surface. More specifically, microstructuring of the flat silicon (Si) substrate surfaces by ultrafast fs lasers under reactive gas (SF₆) atmosphere chosen as a method of surface micro-structuring because it produces surface morphologies through a simple one-step process [T.-H.Her et al., 1998⁸⁴]. Pure sulfur hexafluoride (SF₆) plasmas produce large quantities of atomic fluorine (F) that is used to quickly etch silicon. When SF₆ plasma is used to etch silicon, it typically results in etch profiles that are isotropic in nature [Bates Robert L. et al., 2014⁸⁵].

At room temperature SF₆ is stable and does not chemisorb on Si. However heating at approximately 1000°C may initiate a thermal reaction. This suggests that laser heating could cause a reaction. SF₆ can be physisorbed at 90K or for P ≥ 1Torr at room temperature⁷⁴. The dissociation of SF₆ leading to the formation of fluorine radicals. Etching of Si can then occur through the formation of these F radicals, which eventually react with Si to form volatile Si containing fluorine compounds. A theoretical model is developed for plasma etching of silicon with SF₆. The three-dimensional model developed includes diffusion and convection of molecular fragments in a duct geometry [Lii, Y.-J. et al., 1990⁸⁶]. Gaseous or physisorbed SF₆ molecules are excited into higher vibrational states and chemisorb on Si surfaces resulting to the formation of fluorine ions. Part of the chemisorbed F- ions penetrate into the Si forming a fluorosilyl layer [J.D.Fowlkes et al., 2000⁸⁷]. The chemical reactions describing the chemisorbtion processes are shown below⁷⁴:

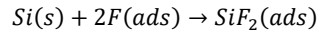
Vibrationally excited SF₆^{} dissociatively chemisorb:*



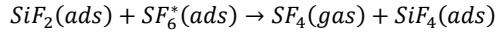
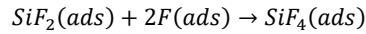
At very high laser intensities, F radicals are produced. These can spontaneously chemisorb on Si surfaces:



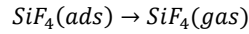
Chemisorbtion may lead to SiF₂⁻ like state:



where F may also penetrate beneath the surface. The reaction between chemisorb species according to:



results in the formation of SiF_4 that desorbs from the surface:



As a result, the formation of the nano-roughness on the MCs structures becomes more apparent with increasing the pressure of SF_6 gas.

1.2.6 Surface structuring of steel via ultrashort – pulsed laser processing

Texturing surfaces to create micro/nano scale surface structures has tremendous technological importance^{1,2,4,8}. The enhancements in surface area, resulting from formation of various types of micro/nano structures have important applications in altering the surface wetting properties to make them superhydrophobic for self-cleaning applications [^{13,30}, Kietzig A et al.,2009⁹⁰]. Texturing of metal surfaces has been carried out using various techniques such as grit-blasting [Wennerberg A et al.,1996⁹¹], chemical etching [Bathomarco R et al.,2004⁹²], electrochemical treatment [Madore C et al.,1999⁹³], and laser treatment [⁹⁰, Sano T. et al.,2005⁹⁴], etc. Studies have shown that laser processing have advantage over other techniques in terms of more reproducibility and less contamination [Gaggl A. et al.,2000⁹⁵] due to its non-contact process. Surface texturing in metals has been reported using nanosecond Nd:YAG and excimer lasers [Bereznai M. et al.,2003⁹⁶], picosecond Nd:YAG and sub-picosecond excimer lasers⁹⁶. However, the structures formed by these lasers do not exhibit well-defined features. Recently, femtosecond lasers have become an advanced tool for material processing and have advantages over nanosecond lasers in terms of high precision, reduced heat-affected zone, and minimum burr formation [Chichkov B. et al.,1996⁹⁷]. More recently, researchers have demonstrated that femtosecond laser pulses could be used to produce self-organized regular arrays of nano-textured conical microstructures in inorganic materials, e.g. steel [Hermens, U. et al.,2017⁹⁸, S. V. Kirner et al.,2017⁹⁹].

It is known that metals exhibit high reflectivities, low penetration depths and are excellent electrical conductors. The electromagnetic waves may be seriously affected by the abundance of free electrons. In particular, when ultrafast laser metal interaction is considered, other parameters such as polarization, laser intensity, sample surface roughness, phase transition and oxide films also affect the reflectivity [Schmidt V. et al.,2000¹⁰⁰].

In case of metals, researchers have shown that the surface ripple periodicity is smaller compared to the incident radiation wavelength and that the formation of conical microstructure formation occurs with successive impingement of laser shots on target surface [Barada K. Nayak and Mool C. Gupta,2010¹⁰¹]. Furthermore ripples and grooves both show a clear correlation with the laser beam polarization (grooves: parallel to polarization, ripples: perpendicular to polarization), the spikes morphology is less dependent on that. The spikes exhibit a clear dependence with the laser intensity (local laser fluence)⁹⁸, like in the Si case (Fig. 1.18). Also, the spikes formed by fs pulsed laser irradiation, represent a multi-scale structure, where the micrometre-sized spike-like features are additionally covered by a nanoscale roughness⁹⁹.

By irradiating steel surfaces with fs laser pulses above the ablation threshold in the presence of a variety of background mediums, functionalized quasi-periodic sharp conical micrometer-sized spikes are formed. The selection of the surrounding medium affects both the attained surface features and chemistry is chosen depending on the application [P. Pou et al.,2018¹⁰²]. In the special case of wetting properties, surface pattern inspiration has often been drawn from natural archetypes which are mimicked with the use of ultrashort laser pulses^{98,99}. Although many works have been reported where the wettability of steel samples has been modified with the application of laser pulses, the acquired wetting properties are unstable and evolve spontaneously following irradiation⁹⁹.

The second objective of the present thesis was the fabrication of hierarchical steel structures, inspired by the bark bug [⁹⁹, T. van der Heyden and J.M. Díaz,2016¹⁰³], with stable hydrophilic and anti-corrosive behaviors. One way to achieve these formations is the irradiation via ultra-short fs pulsed laser in presence of a gas which reacts with the initiate surface. More specifically, microstructuring of the flat steel surfaces by ultrafast fs lasers under reactive gas (NH₃) atmosphere chosen as a

method of surface micro-structuring because it produces functionalized surfaces through a simple one-step process. Pure ammonia (NH_3) plasmas produce large quantities of amides (NH_2) and imidogen radicals (NH) that is used to quickly etch steel. The chemical reactions describing the chemisorbtion processes are similar to the SF_6 on Si (section 1.2.5). The interplay between increased roughness and polar surface chemistry enhances the hydrophilicity of the attained surfaces that in contrary to the samples processed in ambient air, remain highly hydrophilic after irradiation. Furthermore the presence of ammonia has also be found to inhibit surface oxidation during a systematic corrosion test study.

The combination of these two functionalities, hydrophilicity and corrosion resistance which are induced in a single-step fabrication procedure on steel targets, could find applications in metallic cooling systems and heat transfer or dissipation devices.

1.3 Gold nanoparticles

Nanotechnology generally refers to a field of science and engineering dedicated to materials of sizes ranging from 1 – 100 nm [Mody et al. 2010¹⁰⁴, Salata 2004¹⁰⁵]. The term ‘ nano ’ is extracted from the Greek word ‘ dwarf ’ , which means ‘ extremely small ’ . When used as a prefix, it means 10^{-9} or 0.000000001 meter [Thakkar et al. 2010¹⁰⁶]. Particles of sizes between 1 and 100 nm show fascinating properties with unusual characteristics that lead to the formation of unique properties in nanosystems, which are not observed in ordinary materials. These are considered as nanoparticles (NPs). Metallic nanoparticles have different physical and chemical properties from bulk metals (e.g., lower melting points, higher specific surface areas, specific optical properties, mechanical strengths, and specific magnetizations). Their unique properties might prove attractive in various industrial applications [Vollath, D.,2013¹⁰⁷]. Gold nanoparticles (AuNPs) and their arrays are some of the most studied nanomaterials, with promising applications in many fields such as electronics, optoelectronics, catalysis, solar cells and biology [Zhou et al., 2009¹⁰⁸]. These particles are also malleable in a molecular sense: groups of functional molecules (ligands) can be attached easily as shown in Figure 1.20.

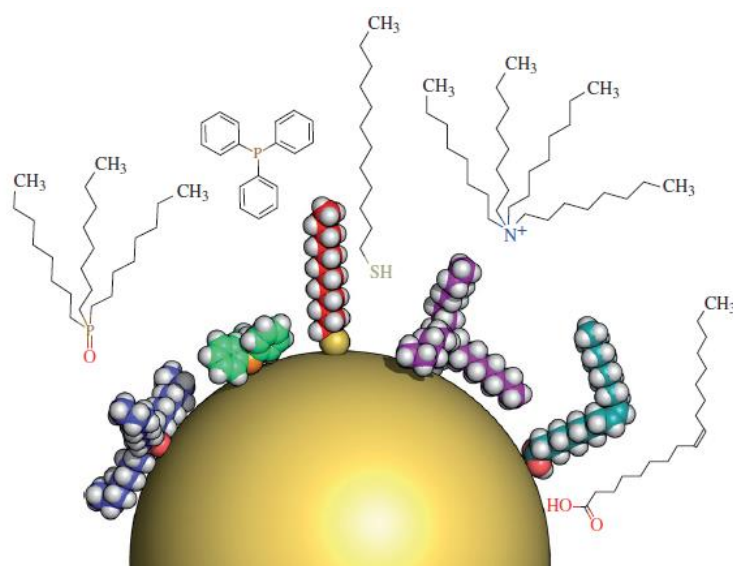


Figure 1.20 : Commonly used hydrophobic ligand molecules drawn to scale along with a particle of 5nm diameter. The particle is idealized as a smooth sphere; the schematic molecule structures above are not drawn to scale. Left to right: trioctylphosphine oxide (TOPO), triphenylphosphine (TPP), dodecanethiol (DDT), tetraoctylammonium bromide (TOAB) and oleic acid (OA). The spatial conformation of the molecules is only shown schematically as derived from their chemical structure and space-filling models [Sperling R. and W. J. Parak, 2010¹⁰⁹].

1.3.1 Synthesis of gold nanoparticles

The most important property of nanoparticles is their size, as many applications depend on it. Size polydispersity is an undesirable characteristic. Thus, prediction of both size and size dispersity for a given system is of concern in systematizing the manufacture of nanoparticles. The methods of nanoparticle synthesis are classified as (i) gas-phase and (ii) liquid-phase [Kumar S. et al., 2007¹¹⁰].

- (i) Gas-phase based synthesis method: Bulk material is evaporated using high energy sources such as resistive heating and lasers to obtain a supersaturated gas phase, which, under controlled conditions, produces nuclei that grow to become nanoparticles.
- (ii) Liquid-phase based synthesis method: Precursors react to form a supersaturated solution, which nucleates and gives rise to particles ranging from 1 to 100 nm in size with stability ranging from a couple of hours to years. Wet synthesis methods are attractive at least for two reasons: a) they are more energy efficient and b) they can be used to produce nanoparticles using the standard apparatus available in a laboratory.

So far, two strategies have been followed for wet synthesis. In the first strategy, two reactants, usually both of them in micellized form, are mixed and nanoparticles form inside them by precipitation. The size of particles is controlled by the rates of nucleation and growth, and stabilization is provided by adsorption of surfactant. This strategy offers scope for good control over particle size. In the second strategy, precipitation is carried out in bulk in the presence of stabilizers that adsorb on nanoparticles and prevent coagulation of particles. Three widely used bulk-precipitation-based techniques for the synthesis of gold nanoparticles are as follows: (1) citrate method of Turkevich et al.,¹¹¹ (2) citrate-tannic acid method of Muhlfordt,¹¹² and (3) Brust-Schiffrin method of Brust et al.,¹¹³. The first two methods yield particles which are stable against coagulation, whereas the last one produces particles which are also capped and cannot grow further.

More specifically, colloidal nanoparticles are dispersed in a solvent that can be either water-based or an organic solvent for hydrophilic or hydrophobic particles, respectively, while amphiphilic nanoparticles can be dispersed in both kinds of solvents. The synthesis of colloidal NPs involves surfactant molecules that bind to their surface, which stabilize the nuclei and larger nanoparticles against aggregation by a repulsive force¹⁰⁹. The ligand molecules bound to the nanoparticle surface not only control the growth of the particles during synthesis, but also prevent the aggregation of the nanoparticles. The repulsive force between particles can, in principle, be due to electrostatic repulsion, steric exclusion or a hydration layer on the surface. Various chemical functional groups possess a certain affinity to inorganic surfaces, the most famous example being thiol to gold.

Conjugation strategies for AuNPs

The labile capping ligands on AuNPs (citrate, thiols, or other adsorbed ligands) can be displaced by thiols through a place ligand exchange reaction to synthesize mixed monolayer-protected AuNPs (Figure 1.21(A)). Place ligand exchange allows the secondary tethering of organic molecules or biomolecules to the surface of AuNPs (Figure 1.21(B)). Non-covalent conjugation is a simpler way for molecules to bind to AuNPs. Alternatively, covalent conjugation of molecules to AuNPs stabilizes the conjugates, which is more useful when stable constructs are required (e.g., amine-carboxylate coupling [U. Drechsler et al., 2004¹¹⁴]).

Although there are several synthesizing methods for AuNPs, such as electrochemical method [Reetz and Helbig 1994¹¹⁶, Reetz et al., 1995¹¹⁵], seeding growth method [Jana et al., 2001¹¹⁷], biological method [Das et al., 2011¹¹⁸, Smitha et al., 2009¹¹⁹], sonochemical method [Itoh et al., 2004¹²⁰], electron beam lithography [Eustis Susie, and Mostafa El-Sayed, 2006¹²¹].

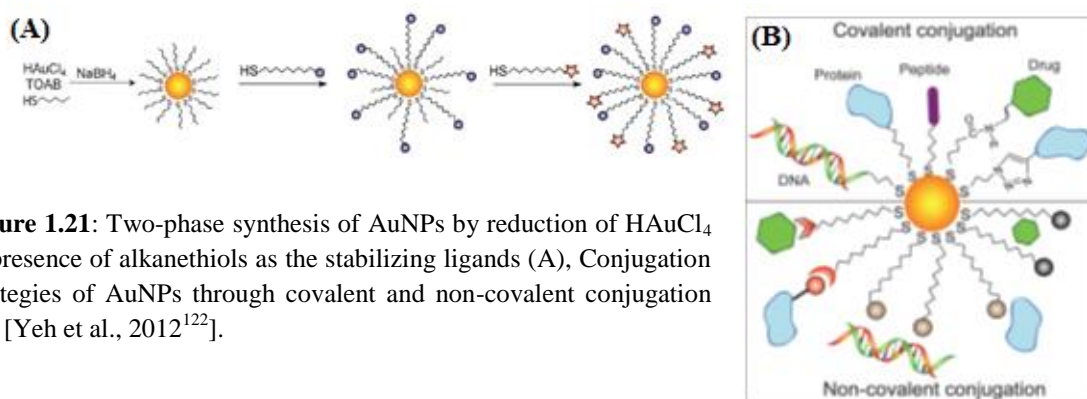


Figure 1.21: Two-phase synthesis of AuNPs by reduction of HAuCl_4 in presence of alkanethiols as the stabilizing ligands (A), Conjugation strategies of AuNPs through covalent and non-covalent conjugation (B) [Yeh et al., 2012¹²²].

1.3.2 Properties of gold nanoparitlecs

AuNPs are being widely used in a variety of biomedical applications because of their compatibility of synthesis and functionalization, less toxicity, and facility of detection [Tiwari et al. 2011¹²³]. Their properties depend on their shape and size. Colloidal gold, unlike bulk gold, is considered to be highly reactive, allowing for new applications. The applications of gold are further extended by colloidal gold which are submicrometer size particles of gold [Shah M et al., 2014¹²⁴]. Prerequisite for every possible application, of colloidal AuNPs (range 1 nm to 1 μm), is the proper surface functionalization of such nanoparticles, which determines their interaction with the environment. These interactions ultimately affect the colloidal stability of the particles, and may yield to a controlled assembly or to the delivery of nanoparticles to a target, e.g. by appropriate functional molecules on the particle surface¹⁰⁹. Their synthesis technique, makes them extremely stable for both shape and size. Also the functionalization of colloidal AuNPs can be done via bioconjugation with antibodies, proteins or oligonucleotides¹²². This is a very promising technique for scaffold fabrication for drug and gene delivery [Majidi et al., 2016¹²⁵]. In response to the properties of functionalized gold nanoparticles, we chose to work with colloidal

AuNPs, which have on their surfaces functional groups such as amino acids, or organic moieties.

Of particular importance, the optical property is one of the fundamental attractions and a characteristic of a nanoparticle. AuNPs have exceptional optical properties due to surface plasmon resonance (SPR) effects. SPR is an optical phenomenon occurring from the interaction between an electromagnetic wave and the conduction of electrons in a metal. [Hu et al. 2006¹²⁶]. In particular, AuNPs present localized surface plasmon resonances (LSPRs) that lead to a strong absorption/scattering and local field enhancement near such structures [Hubert, C. et al., 2007¹²⁷]. More recent treatments have shown that the color of AuNPs is due to the collective oscillation of the electrons in the conduction band, known as the surface plasmon oscillation. The oscillation frequency is usually in the visible region for gold and silver, giving rise to the strong surface plasmon resonance absorption. When AuNPs are enlarged, their optical properties change only slightly as observed for the different samples in Figure 1.21, whereas the absorption peak of the surface plasmon resonance shift (“red shift”). However, when an anisotropy is added to the nanoparticle, as is the case of nanorods, the optical properties of the nanoparticles change dramatically¹²¹. These changes are due to the free d electrons of gold, which can oscillate in the conduction band. Figure 1.22 shows not big enough color changes for the case of gold nanospheres, with increasing size. On the contrary, in the case of the gold nanorods big color changes can be observed with increasing aspect ratio (length/width).

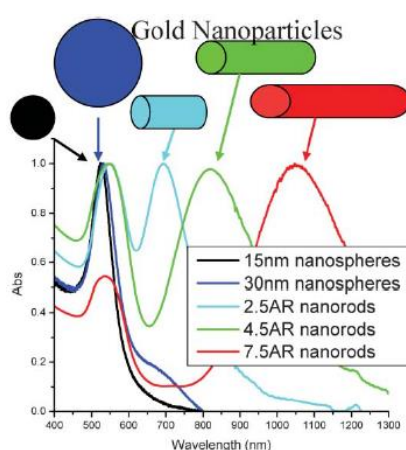


Figure 1.21: Gold nanoparticles – absorption of various sizes and shapes¹²¹.

The absorbance of surface plasmon resonance peak for anisotropic AuNPs can be resolved along the three main axes. The surface plasmon resonance is not only

responsible for the high absorption of the AuNPs, but also causes non-linear properties. The nonlinear properties of spherical AuNPs is closely linked to the depreciation coefficient of the absorption (higher nonlinear properties around the top SPR $\sim 520\text{nm}$) [Pong et al., 2007¹²⁸]. Gold nanorods (GNr) have been shown to have two plasmon resonances, one due to the transverse oscillation of the electrons at visible region ($\sim 520\text{nm}$) for gold and the other due to the longitudinal plasmon resonance at near infrared (NIR) region as shown for various aspect ratios in Figure 1.21.

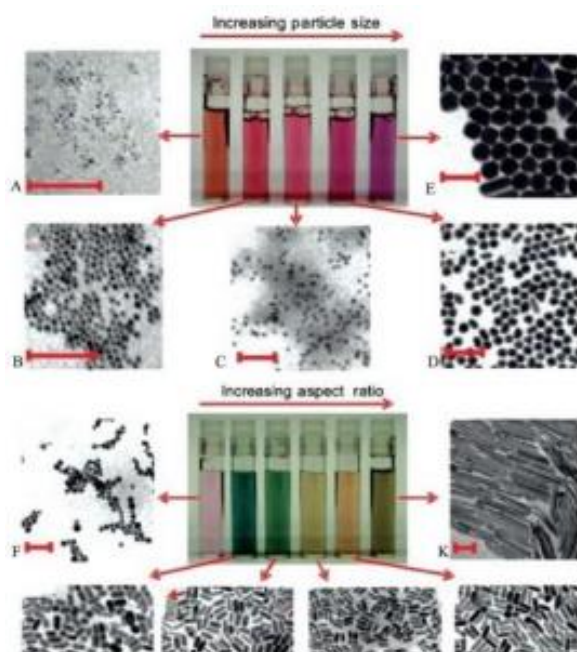


Figure 1.22: TEM images of gold spheres and gold nanorods in increasing order of dimensions with a scale bar of 100 nm for all. Size for gold spheres (A-E) varies from 4-40 nm whereas for gold nanorods (F-K), the aspect ratio varies from 1.5. to 20¹²⁴.

In general, AuNPs have the ability to strongly scatter the electromagnetic irradiation in a specific wavelength which belongs to the visible range and it depends on the size, shape, concentration and environmental optical properties¹¹¹. In the present thesis, we have focused on the size and shape of AuNPs and the effect they have on the optical properties of microstructured Si surfaces. The optical properties and intense electromagnetic fields generated by the nanoparticles make these particles very attractive for sensing, diagnostics, and photothermal therapeutic applications in many areas¹²¹.

Finally, NPs are well known to increase the efficiency of photovoltaic devices by reducing reflection and increasing light trapping within device. However, metal NPs on top flat surface suffer from high reflectivity losses due to the backscattering of the NPs itself. Light absorption due to NPs itself is relatively small and the amount of absorbed light reduces when the size of the metal NPs becomes larger. AuNPs have been widely used to enhance photocurrent of various photovoltaic devices (PVs) [Chee Leong Tan et. al.,2012¹²⁹]. In present thesis we demonstrate a novel structure, which consists of metal AuNPs on hierarchical Si oxidized MCs, that exhibits ultrahigh absorbance in the UV/Vis range and ultralow absorbance in the near IR range (section 4.1.2.3). For metal NPs deposited on transparent media (e.g. glass), other phenomena, like grating coupling, takes place [Cesario J. et. al.,2005¹³⁰]. These patterns could open a way to new PVs [¹²⁹, A. Ranjgar et al.,2013¹³⁴], metamaterials [Mehdi Keshavarz Hedayati et. al.,2014¹³¹], sensors [C.A. Grimes et. al.,2006¹³²] and photonic devices [H. B. Liao,2003¹³³, Dongdong Lin et. al.,2017¹³⁵].

2 Aim of the thesis

2.1 Problem statement & aim of thesis

Nature is a source of inspiration, since it presents unique and distinct ways to solve complex problems. Many models of nature have been studied and artificially constructed.

The attempt of the man to study and simulate artificially the biological systems with their desired properties is termed biomimetics. One of the applications of biomimetic research is the construction of surfaces with optimized properties. The most famous, and studied, biological model of all is the lotus leaf, which comprises a dual scale roughness and exhibits incredible wetting properties. These surfaces are called hierarchical micro-nano surfaces because they incorporate features of different size scales (i.e. micro- and nano-scale).

Using techniques such as photolithography, microcontact printing, microfluidic patterning, electrospinning and self-assembly, 3D topographical features of tailored geometry, roughness and orientation, complemented by the desired spatial resolution at micron and submicron scales, can be realized on material surfaces.

The approach used in the present study involves the fabrication of microconical structured silicon surfaces by ultra-short pulsed laser processing. It has been shown in previous work of the group that when flat silicon is irradiated by ultra-short pulsed laser microconical features arise. The resulting surfaces exhibit remarkable optical surfaces^{1,9}. Thus, we wanted to see how these properties of the micropatterned substrates are influenced by the incorporation of dielectric (e.g. SiO₂) and metal (e.g. AuNPs) coatings. In other words, the first aim of the present thesis was to study what are the respective optical properties of the hierarchical nano-micro-patterned Si substrates.

The second aim of this thesis was to fabricate steel microstructured surfaces with remarkable wetting properties^{98,99,102}. The differences between the ultra-short laser procedures of Si and steel surfaces, is the gaseous medium and laser intensity during the irradiation procedure. For steel samples NH₃ reactive gas was used and for Si samples was used the SF₆ reactive gas. By the choice of irradiation medium, we

achieved stable hydrophilic and anti-corrosive behaviors of the microstructured steel surfaces.

2.2 Flow sheet

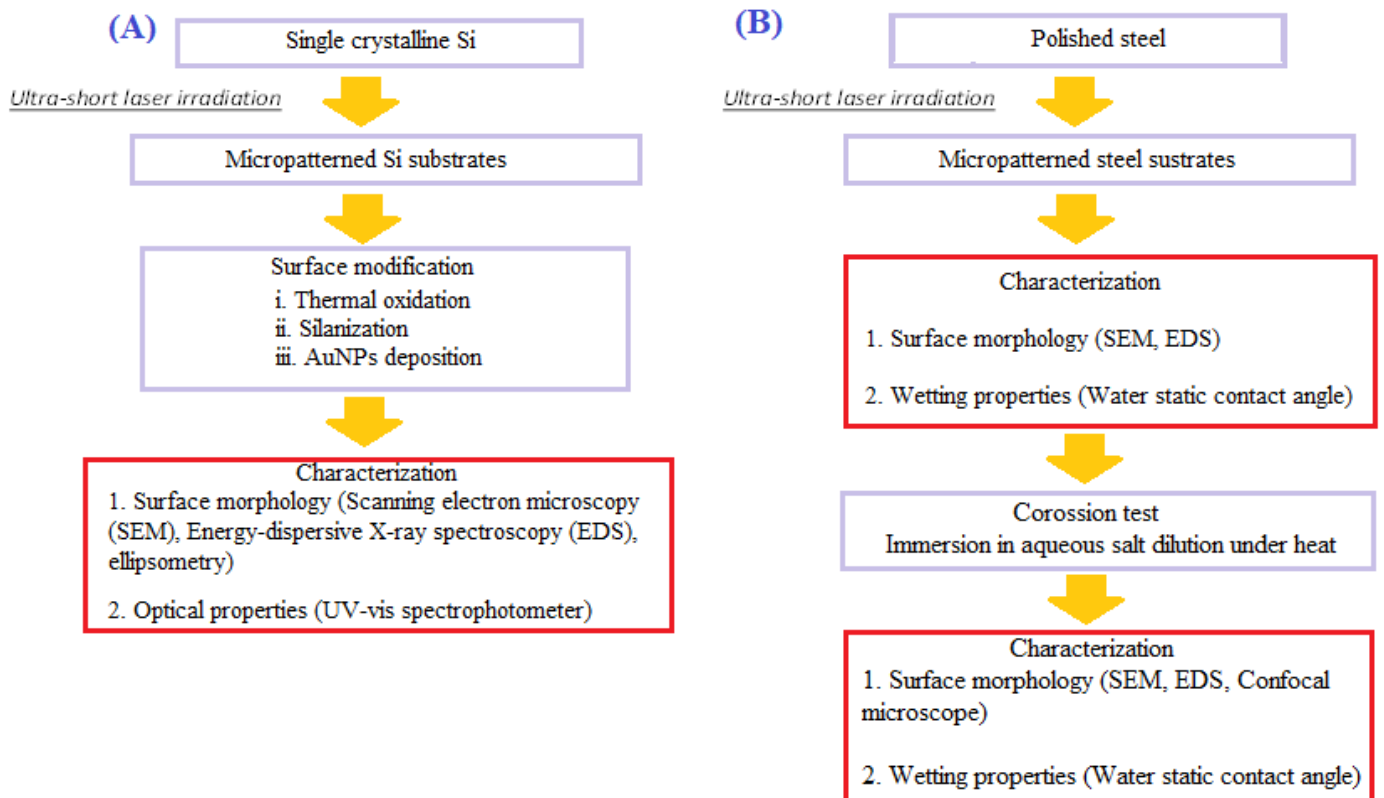


Figure 2.1: Illustrates the flow sheet of the (A) Si and (B) steel experimental designs of the present thesis.

3 Experimental part : Materials & methods

3.1 Fabrication of micropatterned silicon surfaces via ultrashort – pulsed laser

3.1.1 Laser system

Ti:Sapphire laser system is a high repetition rate femtosecond laser system based on chirped pulse amplification (CPA) technique, which uses directly diode-pumped Yb:KGW (ytterbium doped potassium gadolinium tungstate) crystal as active medium. Automated second/third harmonic module for the Ti:Sapphire laser system offers the possibility to choose between three laser wavelengths (1030nm , 515nm and 343nm) by sending a command via computer (USB) or Remote Control Module (RCM). The switching between wavelengths in harmonics module is implemented by means of switchable mirrors which are controlled by two servo motors. The fundamental emission from the laser is directed through a periscope of two mirrors to the output of the harmonics module. The polarization of the output at 1030nm is horizontal (i.e. linear).

3.1.2 Experimental procedure

The micro-conical spike formation process was applied on single crystal n-type Silicon (1 0 0) wafers, with fs laser irradiation in SF₆ gaseous atmosphere.

Si wafers micro-structuring took place in a vacuum chamber evacuated down to a residual pressure of $\sim 10^{-2}$ mbar by means of a vacuum pump. A micro valve system attached to the chamber enabled a precise backfilling of an ambient gas (SF₆). The pressure of the backfilling gas was measured with a needle gauge at 500 Torr. The laser fluence was regulated by using a neutral density filter. The laser beam was first focused by lens with focal plane at 20cm and then entered the chamber through a quartz entrance window, while the irradiation process could be monitored through a plexiglas window, which was laterally mounted on the vacuum chamber.

The processing chamber was placed on a computer driven high precision X-Y translation stage with spatial resolution of 1 μ m allowing sample displacement with regard to the laser beam up to 10000 μ m (Figure 3.1). Scan velocity was stable at 500 μ m/sec and line separation at 20 μ m. The laser fluence used in these experiments

was in the range $0.17\text{--}0.78\text{ J/cm}^2$, in constant wavelength to 1026nm , repetition rate 1kHz and pulse duration 170fs .

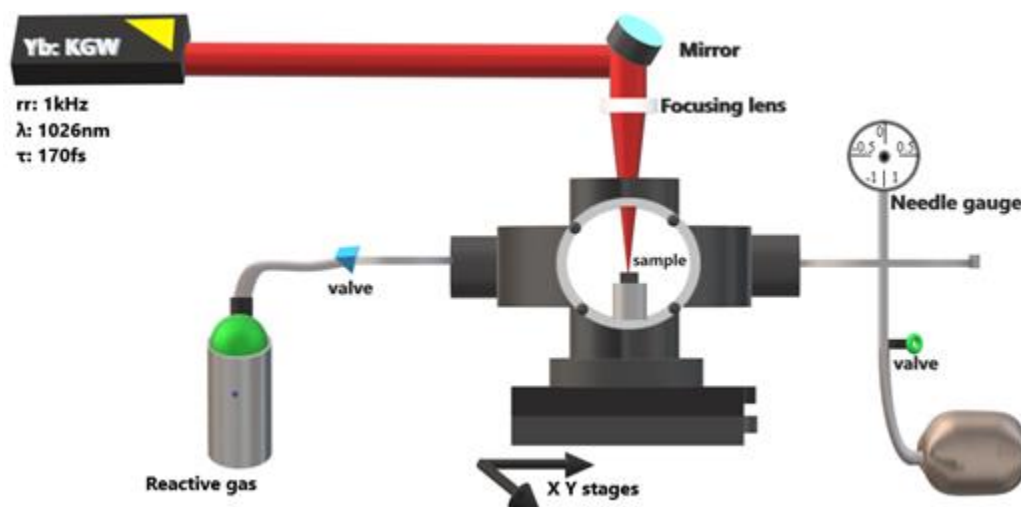


Figure 3.1: Schematic of the experimental ultra-short laser setup

3.1.3 Sample preparation

Single crystal n-type Silicon (1 0 0) wafers, of thickness $300\text{--}750 \pm 25\text{ }\mu\text{m}$ thickness, were cut in square shape by using a pen-diamond, in various sizes, depending on the micro-structured surface size under study, each time. Substrates were first immersed in a vial with ethanol and left in ultrasound water bath for two minutes. Then dried with nitrogen gas.

3.1.4 Thermal oxidation of the substrates

Before thermal treatment, Si substrates immersed in aqueous solution of hydrofluoric acid (HF) with a concentration of 30% for 1 hour. Then dried with nitrogen gas.

Flat and micropatterned Si substrates were subjected to dry thermal oxidation in a ceramic tube furnace at 1000°C for five different time scales (15, 90, 180, 300 and 540 minutes), with ramp rate $20^{\circ}\text{C}/\text{minute}$ (Figure 3.2). The substrates were further processed to characterization (e.g. SEM and ellipsometry). Finally, Si samples that oxidized for 90 min decorated with gold nanoparticles.

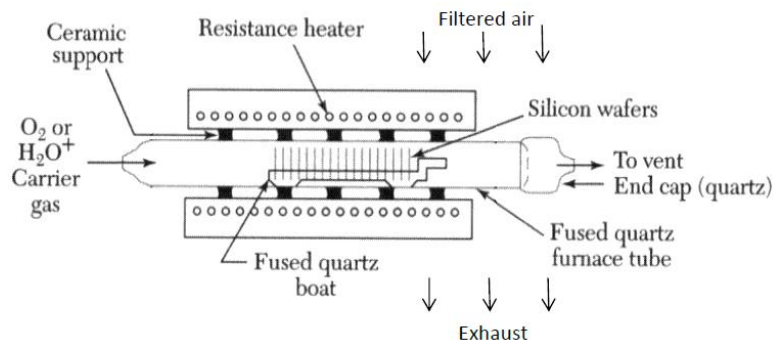


Figure 3.2: Schematic cross section of resistance-heated oxidation furnace [E.H. Nicollins and J.R. Brews, 1952¹³⁶].

3.2 Gold nanoparticles used

Colloidal gold nanoparticles (AuNPs), of spherical size and two diameters (i.e. 7 & 13 nm) have been used for the fabrication of the hierarchical micro-nano substrates. Also, non-colloidal rod-shaped AuNPs with aspect ratio 3:1, were used. The colloidal AuNPs carried the following functionalities: i) the oligopeptide CALNN-RGD, and small organic moieties, like the 4-dimethylaminopyridine (DMAP) (Figure 3.3A, B). All three types of gold nanoparticles were in aqueous solution.

For the deposition of AuNPs on the microstructured silicon substrates, manufactured gold nanoparticle solutions, which proportionally diluted either in nanopure water or in pure ethanol. Figure 3.3 shows the chemical composition and the nomenclatures of the functional groups of AuNPs. Table 3.1 shows the proportions of AuNPs solutions and their sizes.

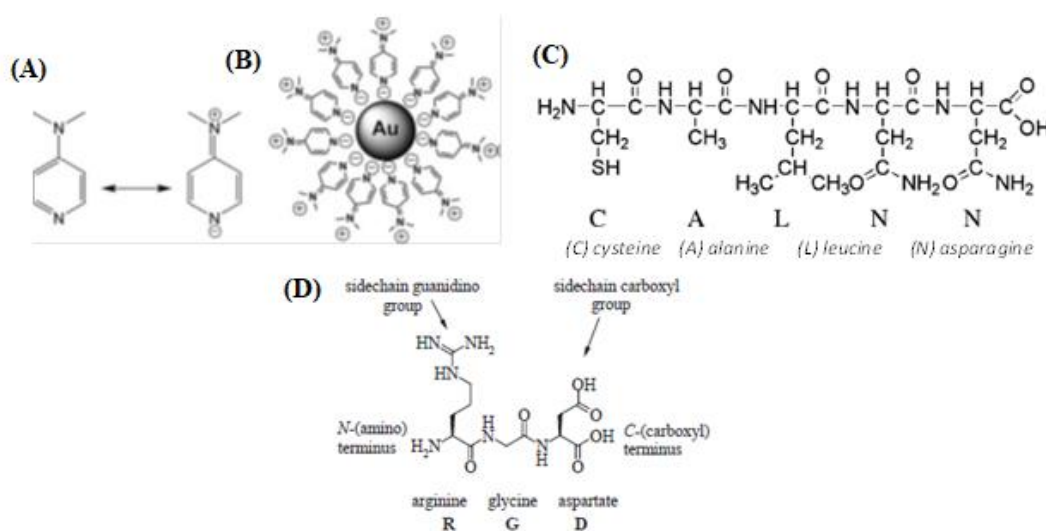


Figure 3.3: Chemical structures of functional groups of the colloidal AuNPs. Resonance of the DMAP molecule (A) and schematic representation of a DMAP-Au NPs (B) [Biver, T et al., 2012¹³⁷],

pentapeptide CALNN structure (C) [Lévy et al., 2004¹³⁹], RGD sequence, its molecular formula and nomenclature (D) [Hersel et al., 2013¹³⁸].

Table 3.1: Proportions of AuNPs solutions and AuNPs' sizes.

<i>AuNP type</i>	Size (nm)	Dilute solvent
<i>DMAP</i>	diameter: 7	30% nanopure water
<i>RGD</i>	diameter: 13	40% pure ethanol
<i>Rod - shaped</i>	aspect ratio: 3:1	0% solvent

**AuNPs synthesized from as.prof. Antonios Kanaras research group, at University of Southampton, United Kingdom, Laboratory for Inorganic Colloidal Nanocrystals and Applications.*

3.3 Deposition of gold nanoparticles onto the microstructured silicon surfaces

In order to deposit the gold nanoparticles onto the microstructured Si surfaces, substrates had to be activated and functionalized, i.e. to create surface functional groups, which tend to form covalent bonds with the gold nanoparticles. The activation of the surfaces has been performed via the piranha solution (i.e. a mixture of sulfuric acid and hydrogen peroxide, v/v: 3:1). Piranha solutions are strong oxidizers and used to remove organic residues from substrates. The functionalization of the surfaces was in turn performed with a Sulfur terminated silane, the (3-Mercaptopropyl)trimethoxysilane (MPTMS).

Micropatterned Si substrates have been thermally oxidized at 1000°C for 90 min in air. This treatment results in a conformal silicon oxide layer. Substrates have been in turn functionalized with (3-Mercaptopropyl)trimethoxysilane (MPTMS). For that, substrates have been activated via immersion in Piranha solution [i.e. H₂SO₄: H₂O₂=3:1 (v/v)] for 30min at room temperature (RT), followed by thorough rinsing with nanopure water and drying with gaseous Nitrogen. Then, substrates have been immersed in MPTMS solution in dry toluene [1.85% (v/v)] for 3hrs at RT followed by rinsing in toluene and ethanol (two times each), drying with nitrogen and thermal annealing at 100°C for 30min.

For the binding of the nanoparticles onto the MPTMS-functionalized surfaces, drop deposition has been followed. A drop of 50 µl has been deposited onto the

MPTMS-functionalized micropatterned Si surfaces, let be evaporated for 16 hours, followed by a thorough rinse with nanopure water to remove the nanoparticles that were not immobilized.

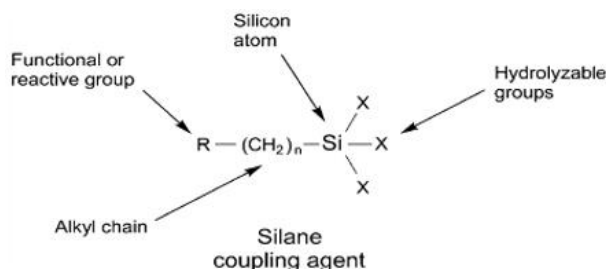


Figure 3.4: The general structure of a silane coupling agent includes a functional group or reactive group at the end of an organic spacer [Hermanson Greg T.¹⁴⁰].

There are several silanes which offer functionalization on surfaces. To present experiments used MPTMS ((3-Mercaptopropyl)trimethoxysilane) (Figure 3.5).

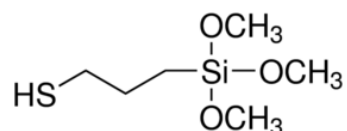


Figure 3.5: Chemical composition of MPTMS, with thiol as functional group (SH) (adopted by Sigma Aldrich).

To effect the binding of the silane, MPTMS diluted in dry toluene (organic solvent), an substrate immersed in for 2:30hours, because the method of silanation, which uses organic solvent is suitable for highly reactive silane derivatives, such as MPTMS. Also, this method is convenient to use for the functionalization of metallic nanoparticles, having the requisite -OH end groups¹⁴⁰. Figure 3.6 shows the final morphology of the functionalized silicon substrates.

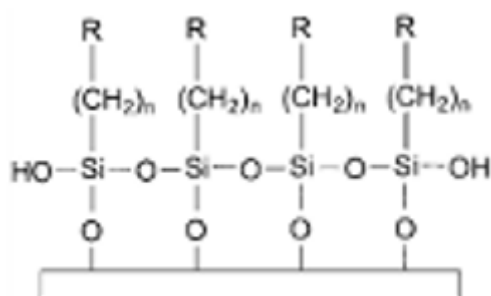


Figure 3.6: Covalent bond formation and coating of surfaces with functional silanes¹⁴⁰.

After this experimental step, the substrates characterized via UV/Vis spectrophotometry (section 4.1.2).

3.4 Fabrication of micropatterned steel surfaces via ultrashort – pulsed laser

For the fabrication of steel (40CrMnMoS8-6) microconed surfaces, were used the same laser system and experimental set up as for the Si surfaces microstructuring (sections 3.1.1 & 3.1.2). The differences are the reactive gas medium, the focal plane of the lens, the line separation step between the scans and the gas pressure.

The micro-conical spike formation process was applied on steel alloy wafers, with fs laser irradiation in air and gaseous ammonia (NH_3) atmospheres. The laser beam was focused by lens with focal plane at 15cm and the line separation was constant at 20 μm . Ammonia gas pressure remained constant at 150 Torr and the laser fluence used in these experiments was stable at 0.73 J/cm².

Debris generated during laser irradiation, by both air and ammonia atmospheres, were removed by immersing the wafers in ethanol ultrasonic bath for 15 min. Finally they dried by blowing nitrogen gas.

3.4.1 Corrosion procedure of the microstructured steel surfaces

Corrosion test was done to characterize the corrosiveness and anti-corrosiveness, of the microstructured steel surfaces, irradiated under air and ammonia gaseous atmospheres respectively. The test was performed using a hot plate, a glass beaker and 140mL of aqueous salt dilution ($\text{NaCl} / \text{H}_2\text{O} : 50 \text{ gr/L}$). The wafers immersed totally in the aqueous salt dilution, at 35°C, for 2 hours. Finally they dried by N gas [Hasan, B. O.,2010¹⁴¹].

3.5 Characterization of the micro/nano patterned silicon & steel surfaces

3.5.1 Scanning electron microscopy (SEM)

3.5.1.1 Technique

Scanning electron microscope (SEM) is a type of microscope that uses an electron beam to illuminate the specimen and produce a magnified image. The beam of electrons is produced at the top of the microscope (electron gun), follows a vertical path through the column of the microscope, makes its way through electromagnetic lenses which focus and direct the beam down towards the sample. The beam passes through pairs of scanning coils or pairs of deflector plates in the electron column, typically in the final lens, which deflect the beam in the x and y axes so that it scans over a rectangular area of the sample surface. The focused beam of high-energy electrons generates a variety of signals at the surface of solid specimens. The signals that derive from electron-sample interactions reveal information about the sample, including external morphology or surface topography, chemical composition and other properties, such as electrical conductivity. The spatial resolution of SEM depends on the size of the electron spot, which in turn depends on both the wavelength of the electrons and the electron-optical system which produces the scanning beam. Depending on the instrument, the resolution ranges between 1 and 20 nm. [N. Cortadellas et al., 2012¹⁴²].

3.4.1.2 Experimental process

Micro-structured surfaces were morphologically characterized by scanning electron microscopy (SEM). SEM was performed on a JEOL 7000 field emission scanning electron microscope with an acceleration voltage of 15 kV.

3.5.2 Energy-dispersive X-ray spectroscopy (EDS)

3.5.2.1 Technique

As its name suggests, X-ray microanalysis involves using X-rays to study very small scales, down to the micro or even nano- and atomic levels. In general terms, X-ray microanalysis relies on the ability to detect X-rays generated when a specimen is

bombarded with high-energy electrons in an electron microscope, with the method used to detect the X-rays defining the exact form of the technique. The X-rays can be detected using a crystal spectrometer fitted with a diffracting crystal to choose the wavelength of interest, or they can be detected with an energy-dispersive spectrometer, which can separate X-rays with different energy levels. An EDS system include: a semiconductor detector, and a main amplifier that provides further amplification and a fast pulse inspection function. All of this can be fully controlled with a computer-assisted system. When the electron beam hits the sample, there is a high probability that an X-ray will be generated. The resulting X-ray escapes the sample and hits the detector. This short-lived current is then converted into a voltage pulse with an amplitude reflecting the energy of the detected X-ray. Finally, this voltage pulse is converted to a digital signal [John Wiley & Sons,2015¹⁴³].

3.5.2.2 Experimental process

In our case, EDS spectrums, ensured via SEM. So the experimental process is the same as in section 3.5.1.2.

3.5.3 Wetting response by static contact angle

Contact angle analysis involves measuring the angle of contact (θ) between a liquid and a surface. The phenomenon of contact angle can be explained as a balance between the cohesive force among the liquid molecules and the adhesive force between the surface and the liquid molecules.

3.5.3.1 Fundamentals

3.5.3.1.1 Young's equation

A small droplet of a liquid deposited on a surface either forms a spherical cap shape with a well-defined equilibrium contact angle θ to the solid or it spreads across the surface until it forms a wetting film. The shape of the drop is described through the precise equilibrium that results from the balance between the surface tensions (γ) at the three-phase contact line formed along the solid–liquid, liquid–gas and solid–gas interfaces. The force balance leads to the well-known Young equation:

$$\gamma_{lg} \cos \theta_o = \gamma_{sg} - \gamma_{sl} \quad (eq. 2)$$

where the subscripts (sg), (sl), and (lg) refer to solid-gas, solid-liquid, and liquid-gas interfaces respectively (Figure 6.1). The angle at which a liquid-gas interface meets the solid surface is called the equilibrium or Young contact angle (θ_o) and for this, the energy of the system reaches a local minimum [P. De Gennes, 1985¹⁴⁴, L. Leger and J.F. Joanny, 1992¹⁴⁵, G. McHale et. al., 2004¹⁴⁶].

The contact angle is a measure of the wetting behavior of a given surface and depending on its value a surface can be characterized as *hydrophilic* ($<90^\circ$) (Figure 3.7 (a)) or *hydrophobic* ($>90^\circ$) (Figure 3.7 (b)).

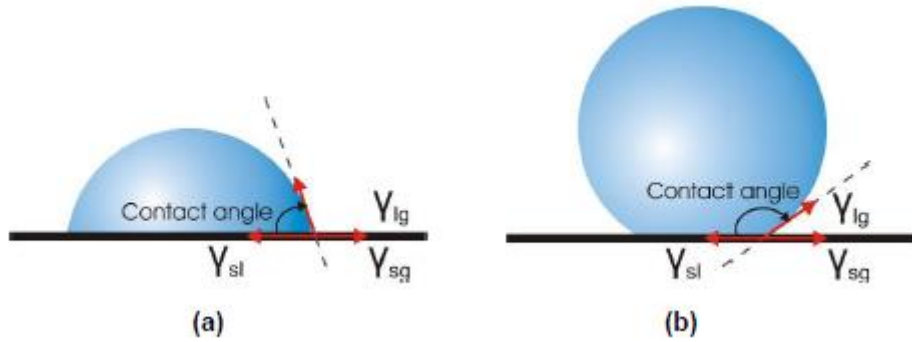


Figure 3.7: A sessile liquid drop on (a) a hydrophilic and (b) a hydrophobic surface.

Surface tension is a manifestation of the intermolecular forces at a surface (or interface) and is defined as the energy (W) needed to increase the surface area per increase in surface area (A):

$$\gamma = \frac{dW}{dA} \quad (eq. 3)$$

High interfacial surface energy for the liquid-solid results in a large contact angle, i.e. *the higher the surface tension of the liquid, or the lower the surface energy of the substrate, the larger the contact angle*. With water, typically the most hydrophobic flat solids can achieve up to $\theta \sim 120^\circ$. In order to obtain an even more hydrophobic surface, structuring which will increase its overall roughness is required. The enhancement of the hydrophilic or hydrophobic character of a surface upon structuring is reviewed in the following section.

3.5.3.1.2 Wenzel and Cassie Baxter states

The effect of the macroscopic surface roughness on the wettability of surfaces has been theoretically approached by two different models.

1. Wenzel model

In the Wenzel model [R. N. Wenzel, 1936¹⁴⁷], the liquid is assumed to completely penetrate within the entire rough surface, described as “homogeneous wetting regime” without leaving any air pockets underneath it (Figure 3.8 (a)). This model predicts that the contact angle will decrease / increase with surface roughness for an initially hydrophilic ($\theta^0 < 90^\circ$) / hydrophobic ($\theta^0 > 90^\circ$) surface, since the ratio of the unfolded surface to the apparent area of contact under the droplet (r) is always greater than unity. The apparent contact angle, θ_w , is then given by the following equation:

$$\cos\theta_w = r\cos\theta_o, r > 1 \quad (eq. 4)$$

where θ_o is the contact angle on a flat surface of the same nature as the rough (Young contact angle).

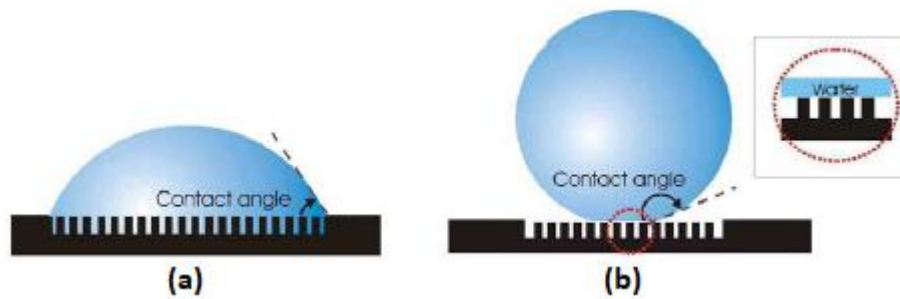


Figure 3.8: A liquid drop (a) in the Wenzel state, where the drop fills the recessed areas and (b) in the Cassie-Baxter state, where air pockets are trapped beneath it, minimizing the surface area of the solid in contact with the liquid.

2. Cassie Baxter model

In contrast, Cassie and Baxter (CB) model assumes [A. B. D. Cassie, 1944¹⁴⁸] that the liquid does not completely permeate the rough surface because air gets trapped underneath it (“heterogeneous wetting regime”). As a result a droplet will form a composite solid liquid / air –liquid interface with the sample in contact, and the effective surface energy of the scaffold below the water will be dominated by air. In

this case, the apparent contact angle, θ_{CB} , is an average of the flat surface, θ_o , and the value for full hover over the flat surface (that is, 180°) and is given by:

$$\cos \theta_{(CB)} = -1 + f_{ls} + r_f f_{ls} \cos \theta_o \quad (eq. 5)$$

where, f_{ls} is the fraction of the projected solid surface that is wet by the liquid, and r_f is the roughness ratio of the wet area.

As the ratio of the area of the projection surface, which comes into contact with the drop, to the area of the total projected area (f_{ls}) is lower than the unity this model always predicts enhancement of hydrophobicity, independently of the value of the initial contact angle θ_o . The lower the value of f_{ls} , the higher the contact angle measured.

When the liquid drop is lying on the top of the rough surface without sinking into the features at all (Figure 3.8 (b)), the roughness factor will be equal to one ($r_f=1$) and Eq. 5 becomes the widely used simplified form of the Cassie-Baxter equation.

$$\cos \theta_{(CB)} = -1 + f_{ls} (1 + \cos \theta_o) \quad (eq. 6)$$

When $f_{ls}=1$ and $r_f=r$, Eq.5 turns into the Wenzel equation.

3.5.3.2 Technique

There are a number of ways to measure the contact angle including sessile drop, captive air bubble method, capillary rise method. Static contact angle analysis provides a first screening of material surface and gives an insight into how the surface will interact with the external world. It indirectly measures surface energy, roughness, contamination, etc. and directly surface wettability.

3.5.3.3 Experimental process

For the sessile drop static contact angles, an automated tensionmeter was used to determine the contact angle, based upon a collection of digital images of sessile drops. The liquid (i.e. distilled deionized millipore water) drop (3 μ l) was gently deposited on the steel alloy samples using a micro litre plunger-operated pipette (Transferpette (1-10 μ l)). Images were captured to measure the angle formed at the liquid– solid interface. The surfaces being in normal atmospheric conditions and at an ambient

temperature of 20°C. The mean value was calculated from at least three individual measurements. Successive measurements were reproducible within $\pm 3^\circ$.

3.5.4 Ellipsometry

3.5.4.1 Technique

Ellipsometry is an optical measurement technique to measure the transmission and reflection properties after light is incident on some material. The name ellipsometry comes from the fact that most often light becomes elliptically polarized after passing through the medium. In ellipsometry change in polarization state is studied to infer properties of medium [Chauhan, Sourabh Singh, 2014¹⁴⁹]. When a monochromatic, plane light wave is directed at a surface at oblique incidence, the plane of incidence is defined as a plane perpendicular to the surface and containing the vector which points in the direction of propagation of the light wave. Figure 3.9 illustrates how a beam of linearly polarized light incident, on a film-covered surface is reflected (r) and Figure 3.10 shows the diagram of an ellipsometry device.

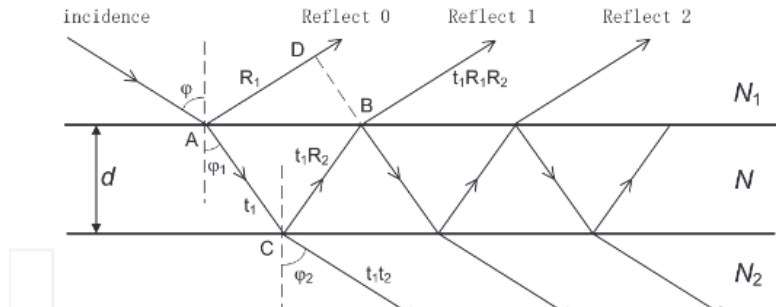


Figure 3.9: Reflection and transmission of polarized light from a transparent film covered surface, where d is the thickness of the film¹⁵⁰.

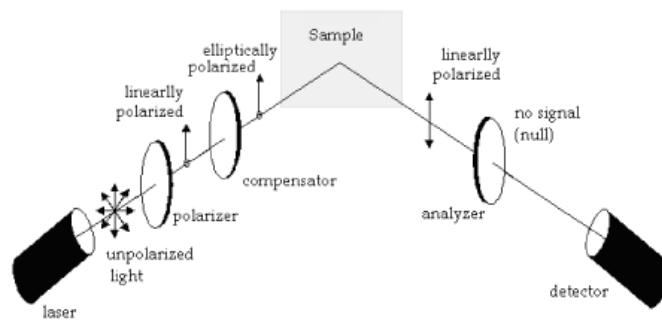


Figure 3.10: Schematic diagram of ellipsometry device [Débora Gonçalves and Eugene A. Irene, 2002¹⁵¹].

3.5.4.2 Experimental process

The measurements for the thickness of silicon oxide made by, the ellipsometer 439, Rudolph Instruments company. The arrangement of optics comprising shown in Figure 3.10.

Beam with wavelength $\lambda = 632.8$ nm produces a laser He-Ne and vertically passes initially through a linear polarizer, and subsequently, by a delay chip phase $\pi/2$ (compensator). The resulting package, incident on the sample at an angle, and regulated by turning the axle, which includes the laser, the polarizer and the compensator. The sample is placed on a regulated basis. The reflected beam passes by a diaphragm and then by another linear polarizer (the analyzer), resulting in the light detector (photomultiplier). The light entering the detector is limited by using an interference filter. The polarizer and the analyzer revolve around the direction of light propagation, and on the side supplied evidence (degrees) for the angle between the optical axis with the components of the passing wave. The compensator is located permanently at a 45° to produce elliptical polarized wave [R.M.A. Azzam and N.M.Bashara,1977¹⁵²].

Simultaneously adjusting the angle polarizer - analyzer achieves the minimum intensity of the beam reaching the detector, and note the angles of analyzer and polarizer. Then, measure the complementary angle rotating the polarizer, and the opposite angle of the analyzer, until reach the minimum intensity of the beam. Through a number of equations can be calculated the film thickness. In our case the film thickness is calculated by a computer.

3.5.5 Optical response by UV/Vis spectrophotometry

Ultraviolet–visible spectroscopy or ultraviolet–visible spectrophotometry UV/Vis) is routinely used in analytical chemistry for the quantitative determination of different analytes, such as transition metal ions, highly conjugated organic compounds, and biological macromolecules. Spectroscopic analysis is commonly carried out in solutions but solids and gases may also be studied.

3.5.5.1 Optical parameters

Three processes can take place when light impinges on a surface: reflection, transmission, and absorption. Reflectance (R), Transmittance (T) and Absorptance (A) are related through [J. M. Palmer,1995¹⁵³]:

$$R(\lambda) + T(\lambda) + A(\lambda) = I \quad (eq. 7)$$

The relative contribution of each process is determined by a material-dependent complex refractive index [R. Menzel,2001¹⁵⁴]:

$$\tilde{n} = n + ik \quad (eq. 8)$$

The real part n is called the refractive index and relates the velocity of light in a medium to that in vacuum:

$$v = \frac{c}{n} \quad (eq. 9)$$

where c is the velocity of light in vacuum.

The imaginary part k is called the extinction coefficient and is a measure of the absorption in the material. The absorption coefficient α of a medium is defined by the well-known Lambert-Beer's Law: the transmittance, $\equiv \frac{I_t}{I_i}$, of a layer decreases exponentially with the distance traveled through the layer (z), where I_i is the incident intensity and I_t is the transmitted intensity¹⁵⁴.

$$I_t(z) = I_i \cdot e^{-\alpha z} \quad (eq. 10)$$

and

$$\alpha = \frac{4 \cdot \pi \cdot k}{\lambda} \quad (eq. 11)$$

where α^{-1} is the distance by which the incident flux has decreased to 1/e and is called skin or penetration depth.

For normal incidence of light from air to the material, the reflectance of a material, defined as the reflected to incident intensity ratio, is expressed as:

$$R \equiv \frac{I_r}{I_i} = \frac{(1 - n)^2 + k^2}{(1 + n)^2 + k^2} \quad (eq. 12)$$

3.5.5.2 Technique

A common way to measure reflectance and transmittance from strongly scattering materials is to use an integrating sphere; a hollow sphere coated internally with a matte finish, diffusing type material. In this way the light that enters the sphere can be scattered uniformly around its interior through multiple reflections, before it is detected. The measurements were performed using a UV/Vis/IR spectrophotometer equipped with an integrating sphere (PerkinElmer Lambda-950). An all-reflecting, double monochromator optical system was used, for the UV/Vis and NIR range. The two radiation sources, a deuterium lamp and a halogen lamp covered the working range of the spectrometer.

3.5.5.3 Experimental process

Initially, ensure that the sample is clean, and the radiation beam is incident only on the sample area we want to measure. Then, substrates placed on a black cardboard (it absorbs radiation) and fixed with a tape.

4 Experimental part: Results

4.1 Characterization of artificially structured silicon surfaces

4.1.1 Morphological characterization of microstructured silicon surfaces

In order to study the effect of platform architecture on the optical response (reflectance, transmittance, absorbance), ultra-short pulsed laser structuring was applied on crystalline silicon (Si) wafers. This technique offers the advantage of patterning Si surfaces with periodic arrays of topographical features of microscale size, while offering high accuracy and reproducibility¹⁶. By varying the laser energy per unit area (fluence), substrates with different roughness have been obtained. At low laser fluence values, the irradiated surfaces comprised submicron-sized ripples, while at increased laser energy, quasi-periodical arrays of conical microstructures (denoted as microcones -MCs- or spikes) were formed (Figure 4.1).

More specifically, we examined the effect of the different laser fluences in a range of 0,17 to 0,78 (J/cm²), which means different laser beam intensity. The parameters

that have been kept constant was the laser wavelength (λ) at 1026 nm, the repetition rate (f) at 1 kHz, the pulse duration (τ) at 170fs and the irradiation step axes (x,y).

4.1.1.1 The effect of laser fluence

In this section we study the formation of microstructures on the surface of Si, by using the Ti:Sapphire laser system ($\lambda=1026$ nm, $\tau=170$ fs), operating at a repetition rate of 1 kHz and SF6 gas pressure at 500 Torr. The effect of the laser processing parameters on the morphology and geometrical characteristics of the fabricated structures was investigated via scanning electron microscopy (SEM). As shown in Figure 4.1, upon increasing laser fluence, conical microstructuring is promoted on the Si surface, with structures becoming more pronounced and spatially separated. In this case fluences varied from 0,17 J/cm² to 0,78 J/cm².

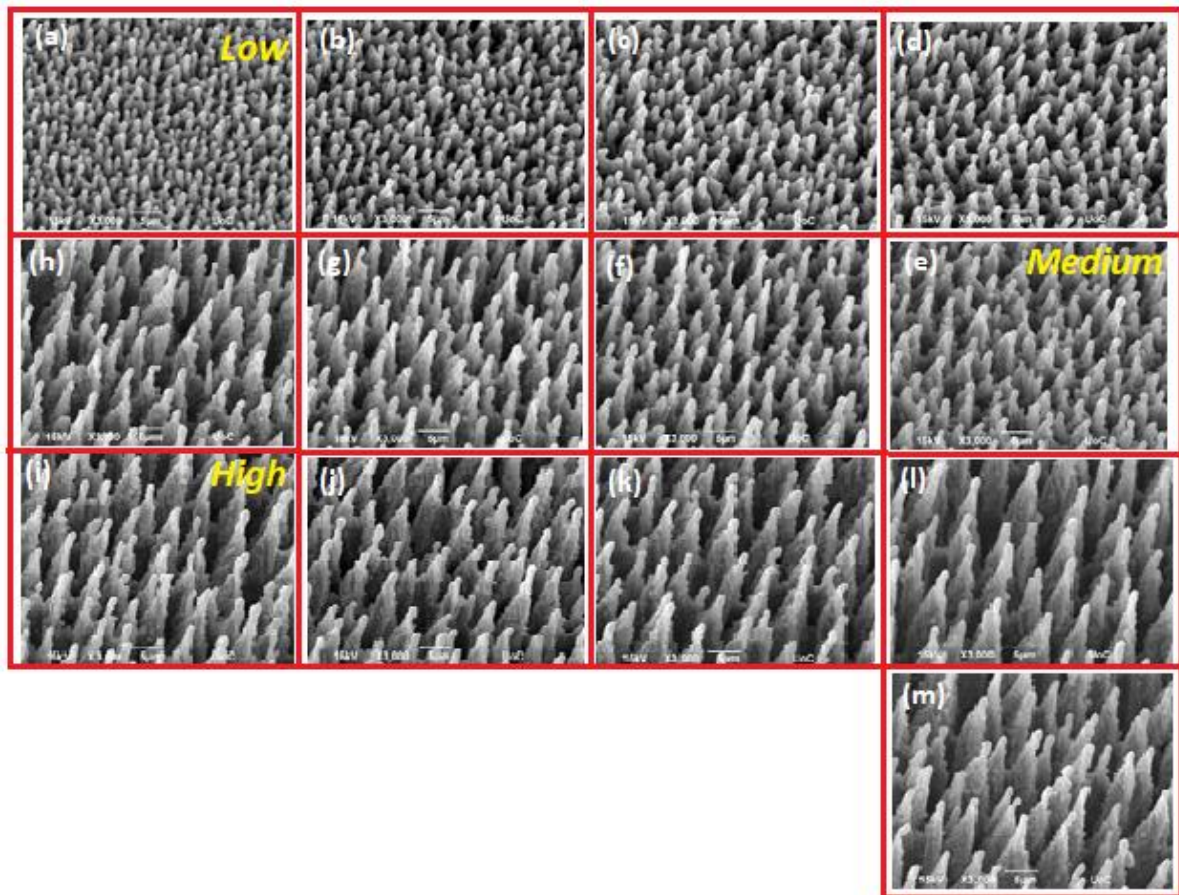


Figure 4.1 : Side SEM images of Si microstructures with increasing laser fluence (a to m). The effect of increasing laser power beam (mW) lead to fluences (a) 0.17 J/cm², (b) 0.22 J/cm², (c) 0.26 J/cm², (d) 0.30 J/cm², (e) 0.35 J/cm², (f) 0.43 J/cm², (g) 0.48 J/cm², (h) 0.52 J/cm², (i) 0.57 J/cm², (j) 0.61 J/cm², (k) 0.65 J/cm², (l) 0.70 J/cm², (m) 0.78 J/cm². Scale bar : 5μm.

For further investigation, we chose three types of roughness (low, medium, high), as shown with yellow texts, in Figure 4.1. In Figure 4.2 the low ($0.17\text{J}/\text{cm}^2$), medium ($0.35\text{J}/\text{cm}^2$) and high ($0.57\text{J}/\text{cm}^2$) roughness are shown. As the laser fluence increased, spikes density (MCs number/ cm^2) and interspike distance (μm) decreased. It has to be noted that, for all fluencies the direction of MCs is the same, and it is perpendicular to the beam polarization (or else to the electric field), (Figure 4.2(j)).

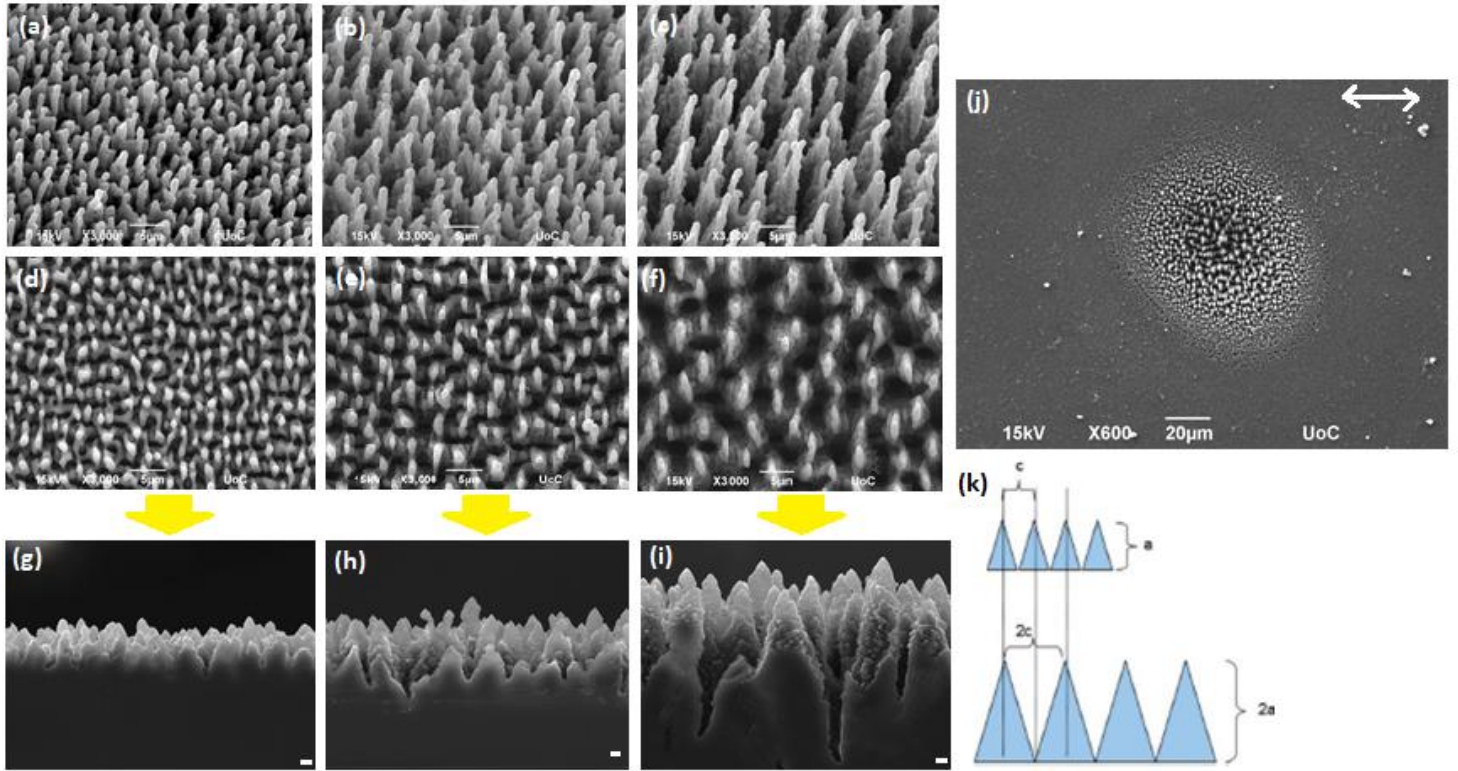


Figure 4.2: General characteristics of the laser patterned Si substrates: (a-c) Side SEM views of the as-prepared Si spikes surfaces structured at three different laser fluencies: (a) $0.17\text{ J}/\text{cm}^2$ (low roughness) (b), $0.35\text{ J}/\text{cm}^2$ (medium roughness) (c), and $0.57\text{ J}/\text{cm}^2$ (high roughness). (d-f) Top view SEM views of the low (d), medium (e), high (f) roughness respectively. (g-i) Cross section images of (d) low, (e) medium and (f) high roughness Si substrates, for height measurements. (j) Spot area where the double narrow indicates the beam polarization. (k) Schematic illustration of a geometrical model for the underlying surface topography based on the lateral cut views (d-f) of the laser patterned surfaces. Abbreviations in (k) area: spike height, c: interspike distance. Top SEM views (d-f) revealed an elliptical base of the microcones which was more pronounced as the laser fluence/ surface roughness are increased.

As shown in Figure 4.2 for fluencies $0.17\text{J}/\text{cm}^2$, $0.35\text{ J}/\text{cm}^2$ and $0.57\text{J}/\text{cm}^2$ (for low, medium, high roughness substrates respectively), MCs' density decreases with

increasing laser fluence. Specifically its value ranges from 106 to 107/cm² (MCs density is 10.78±0.04, 6.80±0.10 and 4.69±0.04 on low , medium and high roughness substrates, respectively). While spike density was lower in the high roughness structures, the MCs height increased. More specifically, MCs height varied from 3.21 ± 0.48 µm in the low roughness structures to 13.81 ± 2.00 µm in the high roughness structures (Table 4.1). Also, the interspike distance increase , while the fluence and spikes height increase. More specifically, MCs distance varied from 3,51±0,35 µm in the low roughness structures to 7,20±1,7 µm.

Table 4.1: Geometrical characteristics of the different micropatterned Si substrates. *

Type of roughness	Density D±STDEV (*10 ⁶ /cm ²)	Height, a ± STDEV (µm)	Interspike Distance, c ± STDEV (µm)	Fluence (J/cm ²)
<i>Low</i>	10.78±0.04	3.21 ± 0.48	3.51±0,35	0.17
<i>Medium</i>	6.80±0.10	4.51±0.33	5.52±0.80	0.35
<i>High</i>	4.69±0.04	13.81±2.00	7.20±1,7	0.57

* Geometrical characteristics of the different substrates used for this study, calculated out of the scanning electron microscopy (SEM) images with the aid of image processing software (ImageJ). The mean values were calculated from at least four individual measurements.

4.1.2 Hierarchical micro/nano patterned surfaces

Scanning Electron Microscopy (SEM) confirmed the i) successful binding of the gold nanoparticles on the micro-structured substrates, ii) all the types of gold nanoparticles (e.g. spherical and rod-shaped), regardless of sizes and functional groups have a very nice and homogeneous distribution with single nanoparticles. This was independent of the substrates's roughness.

Figure 4.3 illustrates SEM images of sphere and rod shaped AuNPs, evaporated on micropatterned and flat Si substrates.

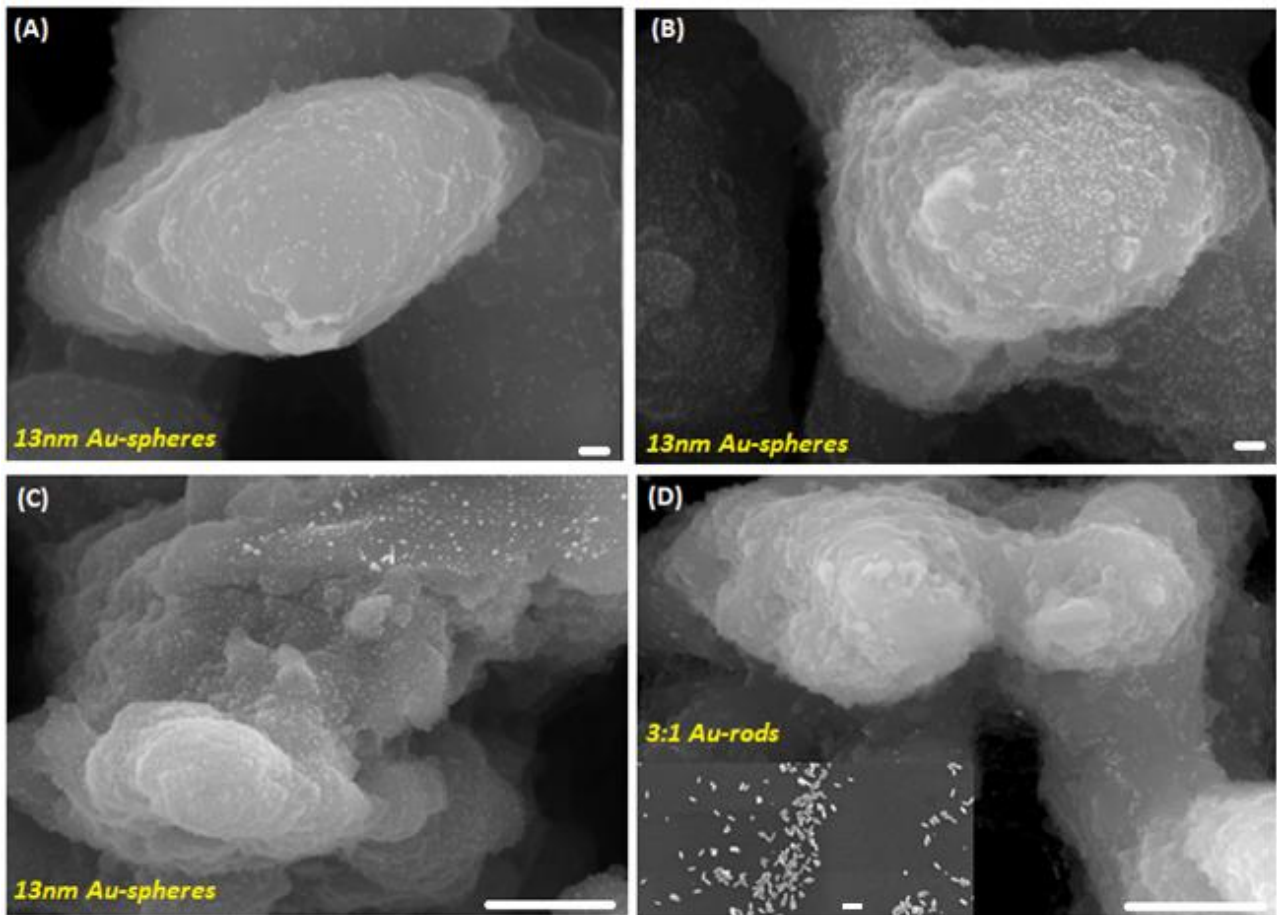


Figure 4.3: SEM images from hierarchical structured Si substrates with gold nanoparticles. On low roughness (Fig4.3(A),(B)) Si substrate with evaporated gold nanospheres diameter:13nm (scale bar: 100nm). Magnification on a single peak. On high roughness (Fig 4.3(C)) Si substrate with evaporated gold nanospheres diameter: 13nm (scale bar: 1μm). On medium roughness (Fig 4.3(D)) Si substrate with evaporated gold nanorods aspect ratio: 3:1 (scale bar: 1μm), in high magnification of two peaks. Inset is an image focusing on the flat area with rod-shaped AuNPs (scale bar: 100nm).

4.1.2 Optical properties of micro/nano - patterned silicon substrates

Si is a semiconductor commonly used in optoelectronic devices, such as solar cells and photodetector applications. Furthermore, the crystalline Si band gap (1.1 eV) makes its absorption and photoresponse to abruptly decrease for wavelengths typically above 1100 nm.

In particular, in this chapter we study the optical properties of laser structured Si. We fabricated extended areas of Si spikes, with fluence value on $0.57\text{J}/\text{cm}^2$ (high roughness substrates), and measure reflectance, transmittance and absorbance as a function of wavelength, compared to flat Si. Also we study the effect of silicon oxide

thickness layer (SiO_2) on the optical response of both flat and fabricated structures, as well as their response to evaporated sphere-shaped and rod-shaped AuNPs on oxidized Si surfaces.

4.1.2.1 The effect of roughness

We measure the total hemispherical reflectance (R) of our samples from 250 nm to 2000 nm using the spectrophotometer described in section 3.5.5.2, equipped with an integrating sphere. The samples fabricated with stable laser pulse duration (170fs), wavelength (1026nm) and SF_6 gas pressure (500 Torr). Figure 4.4 shows the reflectance (R), transmittance (T) and absorbance (A) measurements of bare Si microstructured substrate (black Si), in comparison with the flat bare Si substrate.

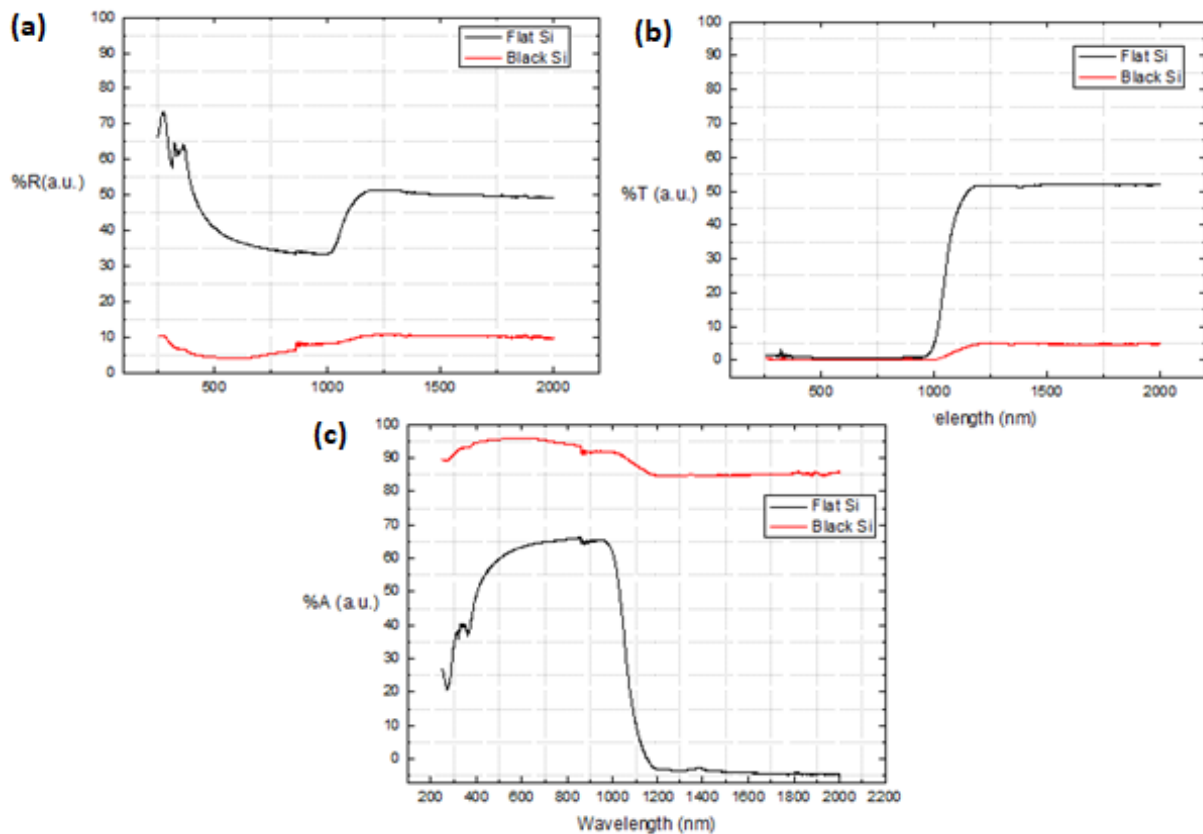


Figure 4.4: (a) Reflectance, (b) Transmittance, and (c) the calculated Absorbance of Si structured using the 170 fs, at 1026 nm laser source (0.57 J/cm^2 , 500 Torr SF_6). The same measurements are shown for unstructured (flat Si), single crystalline Si for reference.

The spectra shown in Figure 4.4 show absorption at below band gap wavelengths ($>1100 \text{ nm}$), where crystalline Si does not normally absorb, suggesting that chemical

modification, structural modification or combination of both, are maybe responsible for the improved optical performance of the laser structured samples.

4.1.2.2 The effect of SiO₂ thickness layer

Through the dry thermal oxidation, silicon oxide layer (SiO₂ thicknesses: 3, 100, 127, 188 and 245 nm) grow on Si substrates (flat and micropatterned) and measured via ellipsometry technique. Due to the different optical properties of SiO₂ (e.g. permeability, multiple reflections-refractions, low absorption [Ji, Yi-Qin et al., 2014¹⁵⁵]), a spectacular change of the spectras for bare microstructured silicon is observed. Energy band gap of SiO₂ is much larger (8.9 eV) than the energy gap of Si. Figure 4.5 shows the R,T and A measurements of a flat crystalline Si substrate before (bare) and after (oxidized) dry thermal oxidation.

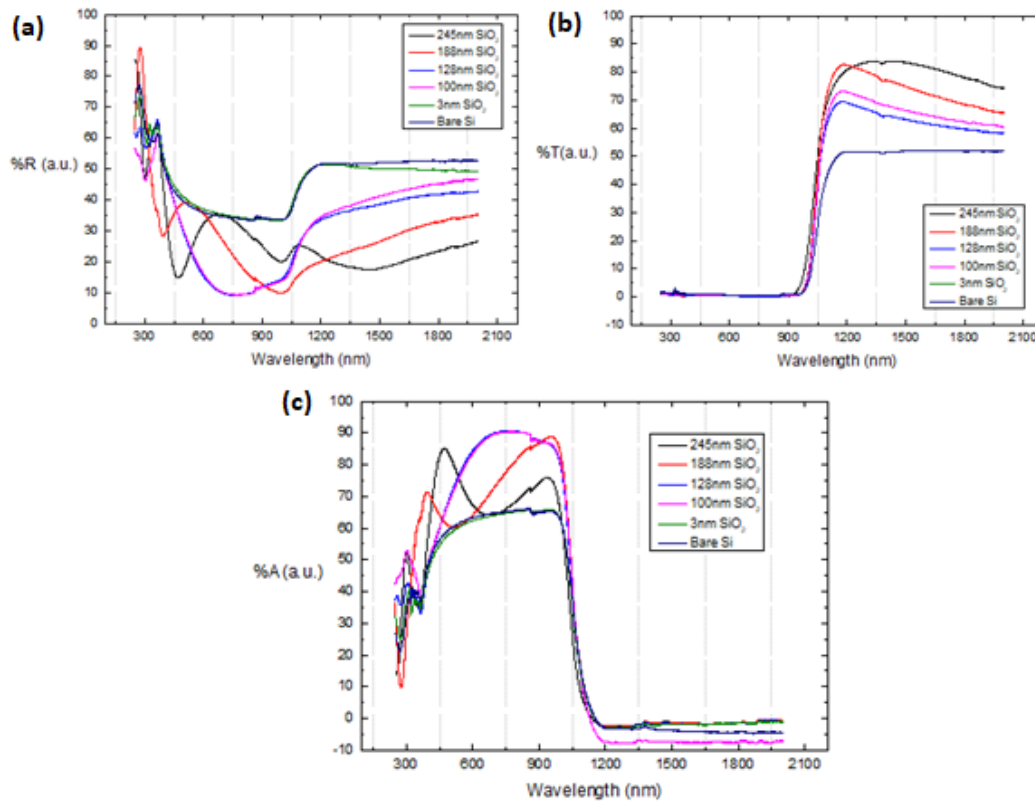


Figure 4.5: (a) Reflectance, (b) Transmittance, and (c) the calculated Absorptance of flat Si samples. Spectras compare the optical response of bare and oxidized flat Si substrates, for five different SiO₂ thicknesses (3nm(green color), 100nm(magenta color), 128nm(light blue color), 188nm(red color) and 245nm(black color)). Non-oxidized (bare Si) indicates with dark blue color.

Figure 4.6 shows the R,T and A measurements of a micro-structured Si substrate (0.57 J/cm^2), before and after oxidation, for the same SiO_2 layer thicknesses as for the flat Si samples.

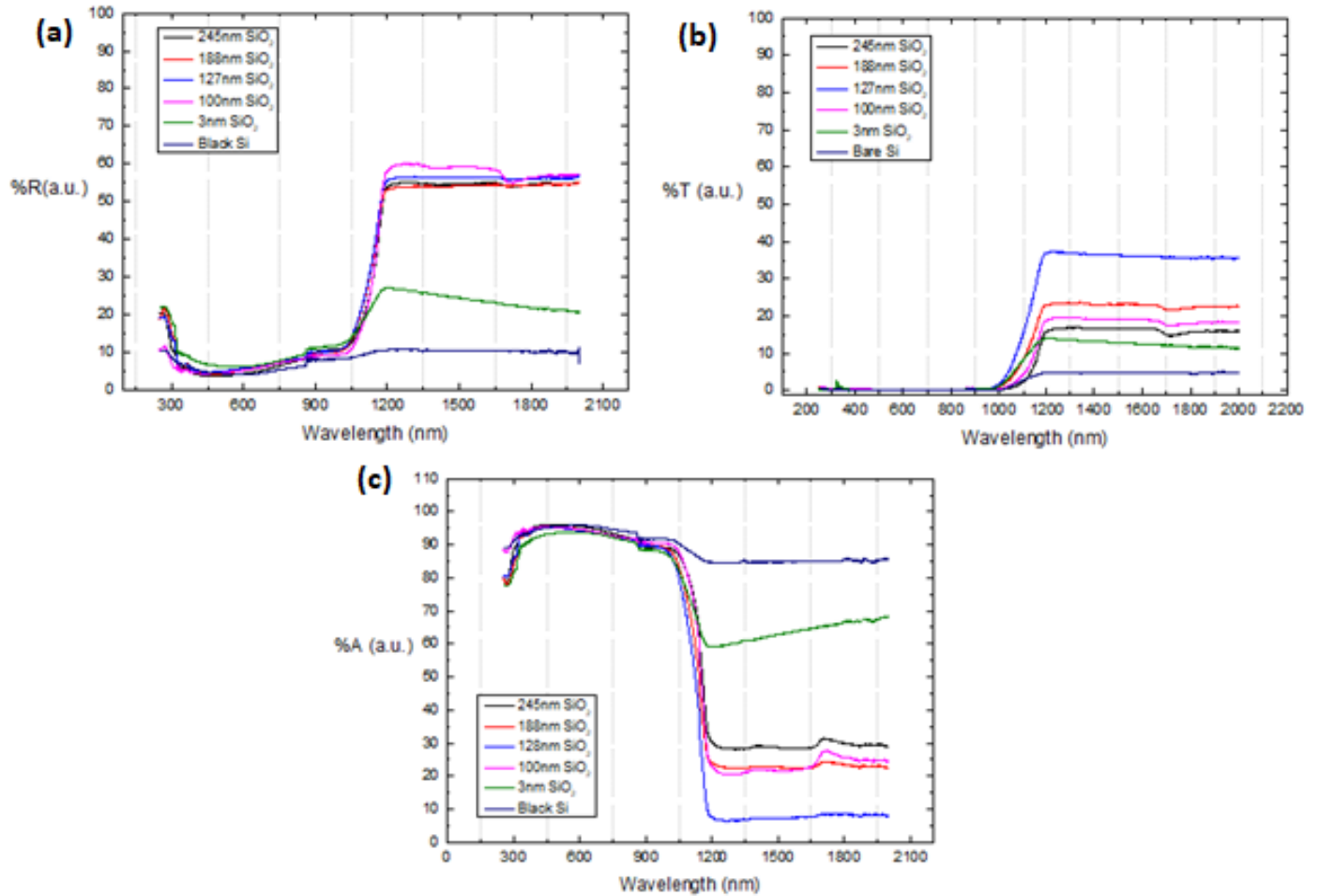


Figure 4.6: (a) Reflectance, (b) Transmittance, and (c) the calculated Absorbance of structured Si samples. Spectras compare the optical response of bare and oxidized micropatterned Si substrates (0.57 J/cm^2), for five different SiO_2 thicknesses (3nm(green color), 100nm(magenta color), 128nm(light blue color), 188nm(red color) and 245nm(black color)). Non-oxidized (black Si) indicates with dark blue color.

The spectra shown in Figure 4.5 (flat Si samples) show absorption incensement in UV/Vis range, for the oxidized samples compared with the non-oxidized Si. We already know, that due to the reflectance reduction (anti-reflecting coating) in this range and electrical properties of SiO_2 layer, it is commonly used in photovoltaic cells [Ketan K Ladava1, et. al.,2018¹⁵⁶]. Spectras clearly show that the position of the transmission maximum, the reflectance minimum, and the absorptivity maximum are functions of the film thickness. In near IR range we observe that, as the thickness of SiO_2 layer increases reflectance reduces and transmittance increases.

In contrast with the flat oxidized Si spectras, in Figure 4.6 we observe increasement of reflectance in near IR range, when the micropatterned Si substrates are oxidized. Also there is transmittance increasement, but in lower rate than the flat oxidized Si. Furthermore, absorbance spectra shows that 128nm SiO₂ thickness layer, on micro-structured Si, leads to high absorbance efficiency (95%) surfaces in UV/Vis range and low absorbance efficiency (5%) surfaces in near IR range. Additionally, we observe (Figure 4.6 (c)) that above 128nm SiO₂ thickness layer, absorbance starts to increase, which maybe means that there is a plateau on 128nm SiO₂ thickness. Refractive index of SiO₂ is ~1.46 and the refractive index of Si is ~3.98.

4.1.2.3 The effect of gold nanoparticles

Because of their unique optical properties, gold nanoparticles are under investigation for many applications. In this section we study the optical response of a system with many “layers”, to investigate the effect of gold nanoparticles. The system structure is: Silicon (micropatterned-high roughness) – SiO₂ layer growth (100nm) – AuNPs (spherical with 13nm, 7nm diameters and rod-shaped with aspect ratio 3:1).

Figure 4.7 shows the effect of gold nanoparticles on R,T and A spectrums of black Si substrate.

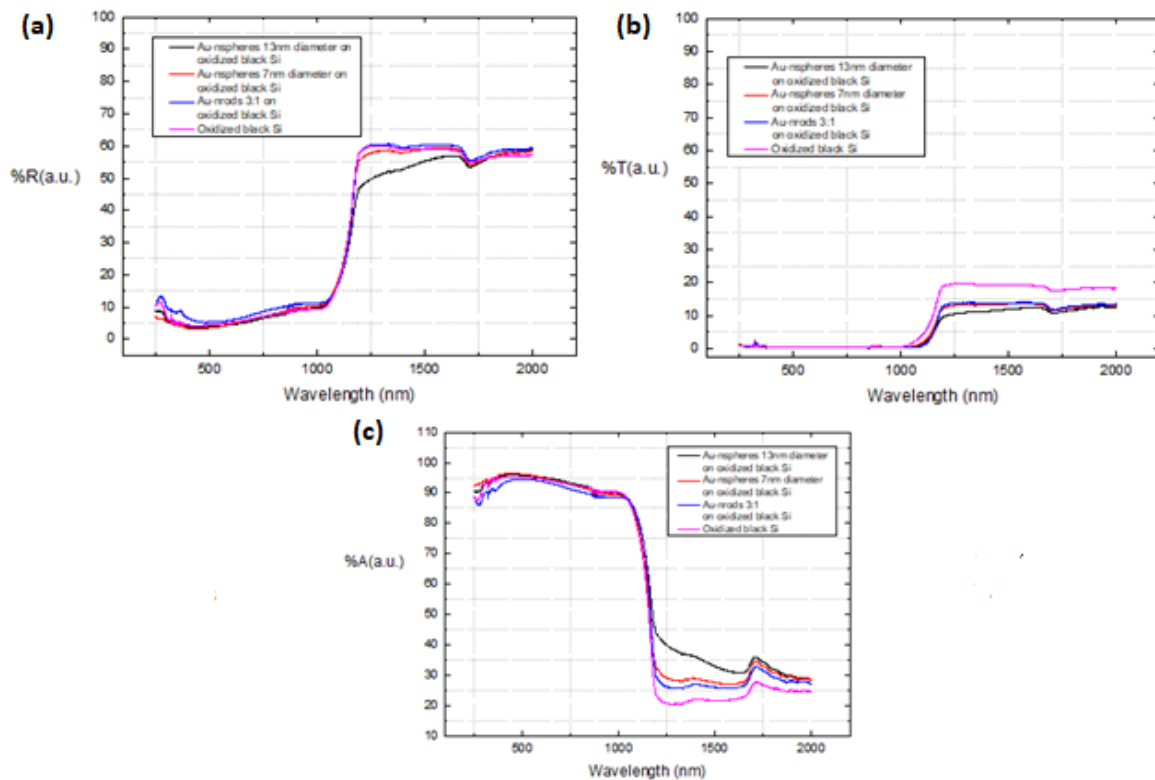


Figure 4.7: (a) Reflectance, (b) Transmittance, and (c) the calculated Absorptance of structured Si samples. Spectras compare the optical response of oxidized and AuNPs decorated micropatterned Si substrates (0.57 J/cm^2), for three different sizes of AuNPs (rod-shaped 3:1(blue color), sphere-shaped with 7 nm diameter(red color) and sphere-shaped with 13 nm diameter(black color)). Oxidized Si without AuNPs indicates with dark magenta color.

4.2 Characterization of artificially structured steel surfaces

4.2.1 Morphological characterization of microstructured steel surfaces - The effect of NH_3 reactive gas

Micropatterning of steel was performed by ultra-short pulsed laser structuring of polished steel wafers. This technique offers the advantage of patterning steel surfaces with periodic arrays of topographical features of microscale size. By varying the laser energy per unit area (fluence), substrates with different roughness have been obtained. We fabricated steel micro-patterned surfaces (steel MCs), under air and ammonia (NH_3) gaseous environment, during the laser procedure, to study the influence of surface chemistry on the wetting properties of steel. SEM-EDS elemental analysis confirmed the presence of nitrogen (N) onto the substrates which irradiated under NH_3 gaseous environment (Fig. 4.8 f).

Figure 4.8 reports the surface morphologies obtained with SEM. It can be observed that the spikes formed upon fs-laser scan processing under air and gaseous ammonia atmosphere environment represent hierarchical structures, where the micro-scale spikes-like features are covered with a nano-scale pattern, the so called ripples.

The steel structures fabricated in gaseous NH_3 are shorter and smaller than spikes fabricated in air environment (Figure 3.1 a,d). The reactive gas, plays a distinct role in the spikes fabrication process, since it determines the size and surface chemistry of the structures obtained.

Constant parameters during the irradiation procedure of steel samples, were the laser wavelength (λ) at 1026 nm, the laser fluence (0.73 J/cm^2), the repetition rate (f) at 1kHz, the pulse duration (τ) at 170fs, the reactive gas pressure (150 Torr) and the irradiation step axes (x,y).

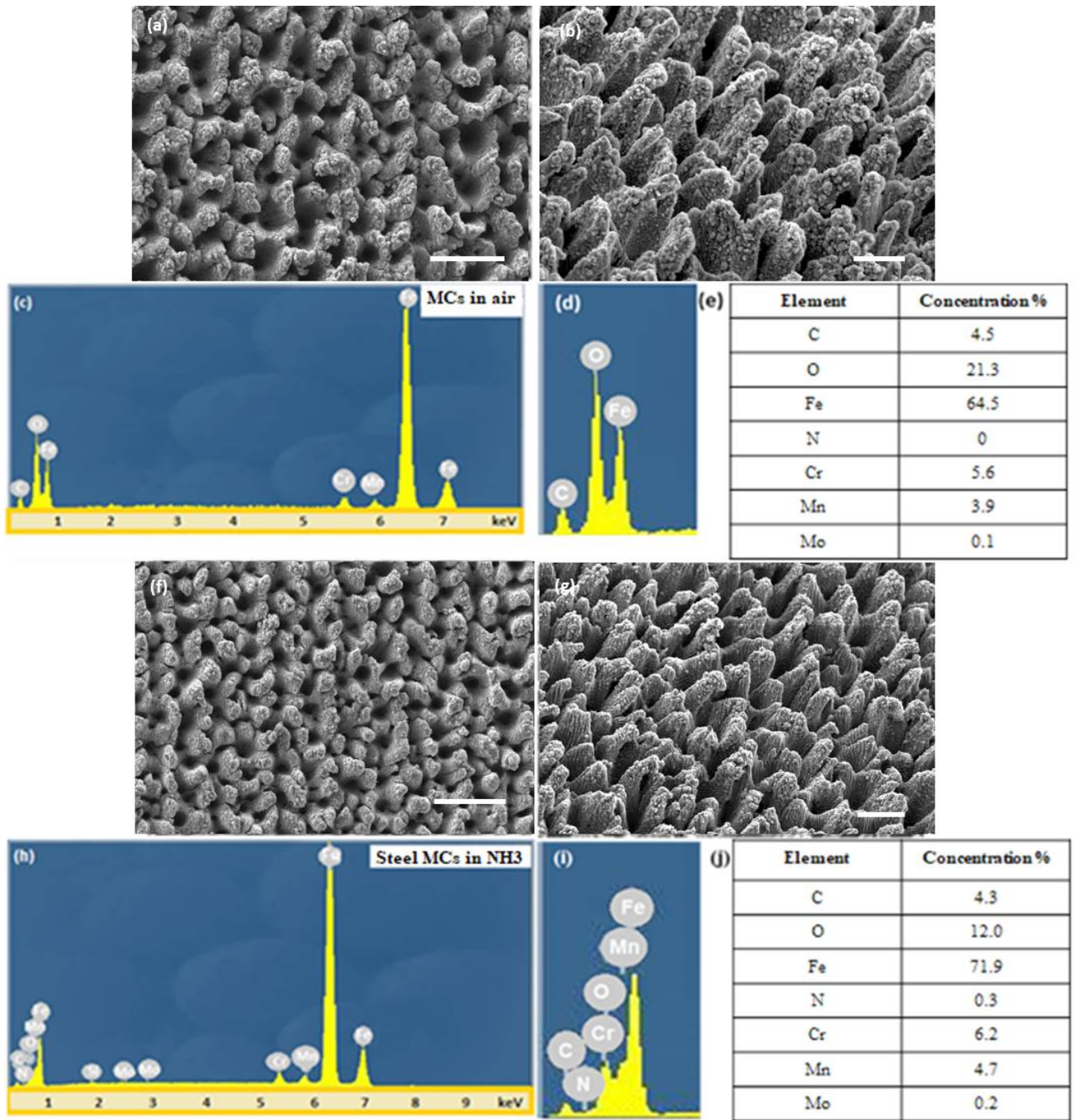


Figure 4.8: Top-view (a) and 45°-tilted (b) SEM images of steel surfaces fabricated in air at a fluence of 0.73 J/cm^2 (scale bars: 50 μm & 20 μm respectively); (c,d) EDS spectra from the area shown in (a). The corresponding elemental analysis is shown in (e); Top-view (f) and 45°-tilted (g) SEM images of fabricated in NH_3 atmosphere at a fluence of 0.73 J/cm^2 (scale bars: 50 μm & 20 μm respectively); (h,i) EDS spectra from the areas shown in (f). The corresponding elemental analysis is shown in (j).

4.2.2 Wetting properties of micro/nano – patterned steel substrates

For controlling the wetting properties of artificial hierarchical surfaces, a systematic study of the wetting response of steel structured surfaces was performed.

In particular wetting response of the functional micro-nanostructured steel substrates, fabricated in both air atmosphere condition and in the presence of NH_3 gas pressure, was examined.

4.2.2.1 The effect of irradiation environment

Laser structuring of steel in a reactive gas (NH_3) atmosphere, was shown to reduce the overall roughness of its surface. Textured steel surfaces have been fabricated by employing the same wavelength (1026 nm), for constant NH_3 gas pressure at 150Torr and constant laser fluence at 0.73 J/cm^2 . Table 4.2 shows that the static contact angle values, of the ammonia functionalized steel micro-nanostructured substrates, is in the range of 10 to 50 degrees for over 140 days. This hydrophilicity was not stable in the case of air structured steel substrates, which became hydrophobic to super hydrophobic after 5 days of laser procedure (Table 4.2). The control substrates for the C.A. measurements, was the flat steel substrate. Micro-structured substrates were (5x5)mm and deionized water droplet's volume was stable to $3\mu\text{l}$.

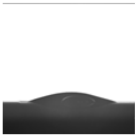
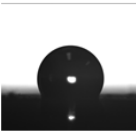
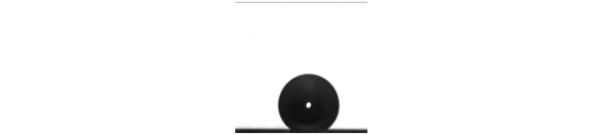




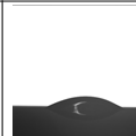

Days	1st	12th	26th	36th	101st	148th
<i>Air structured steel MCs</i>						
C.A. \pm S.D. (o)	16 ± 2	115 ± 3	150 ± 2			
<i>NH_3 gaseous environment structured steel MCs</i>						
C.A. \pm S.D. (o)	17 ± 2	20 ± 4	8 ± 2	18 ± 4	24 ± 3	43 ± 4

Table 4.2: Static contact angle (C.A.) measurements of steel MCs structures in air and gaseous NH_3 irradiation atmospheres for over 140 days after the laser procedure.

Figure 4.9 illustrates the C.A. fluctuation for 148 measurement days between the flat, air-structured and ammonia-structured steel surfaces, after the irradiation procedure.

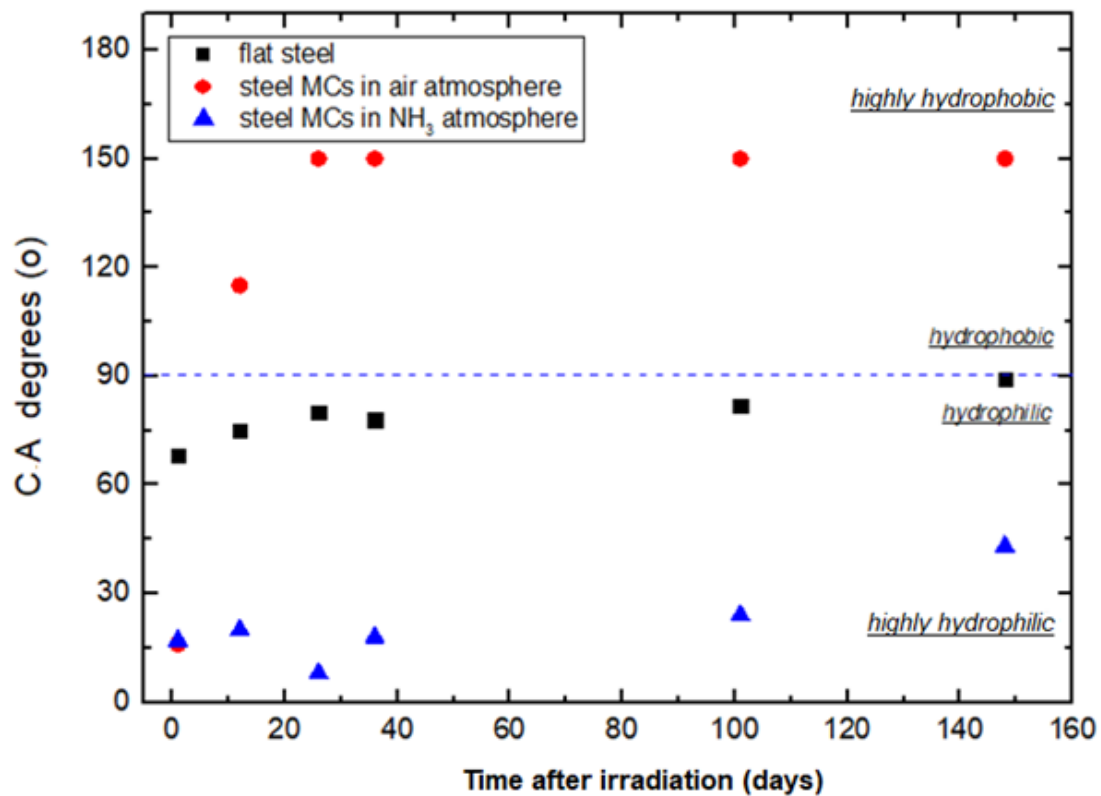


Figure 4.9: C.A. fluctuation for 148 measurement days of flat (black spots), air-structured (red spots) and ammonia-structured (blue spots) steel surfaces.

The wettability of a metallic surface changes with time, due to the air room conditions which are exposed (organic/carbon material contamination), but during this process the surface roughness on microscale stays the same [⁹⁰, J. Long et. al.,2015¹⁵⁷]. Therefore, it is a challenge to maintain long-term hydrophilic characteristics on a metallic surface.

4.2.2.2 The effect of corrosion procedure

Salt dilution tests are suitable as corrosion protection tests for surface coatings with purpose to transform a material from corrosive to anti-corrosive. During corrosion reaction, metals react with nonmetallic elements of their environment and producing chemical compounds¹⁵⁸. Steel micro – nano structured surfaces which fabricated in air and ammonia gaseous atmospheres, for constant laser parameters as in section 4.2.2.1, have been tested. Both substrates immersed in aqueous salt dilution (NaCl / H₂O : 50 gr/L) at 35°C, for 2 hours and finally dried by N gas [Hasan, B. O.

2010¹⁵⁹]. The first observation was the transformation of the transparency of salt dilution to a yellow liquid color.

Figure 4.10 reports the surface morphologies obtained with both SEM (a,c) and confocal microscopes (e-h), after the corrosion test. It can be observed that, for the air structured steel surfaces, have been created salty patterns in a large number (Fig. 4.10 a, e, f), on both micro-structured (region 1) and flat (region 2) areas. The ammonia structured steel surfaces did not represent salty patterns (Fig. 4.10 c, g), on the micro-structured area (region 3), but salty patterns appeared on the flat area (Figure 4.10 h, region 4). Also, we examined the effect of the corrosion by SEM-EDS elemental analysis, which confirmed the presence of sodium (Na) and chlorine (Cl) elements onto the substrates which irradiated under air environment and onto the flat regions (2,4), for both samples (Fig. 4.10 b). In the opposite, steel substrates which irradiated under NH₃ gaseous environment did not represent the two previous elements (Fig. 4.10 d), but continued to represent the nitrogen (N) element, as before the corrosion test (Fig. 4.8 i).

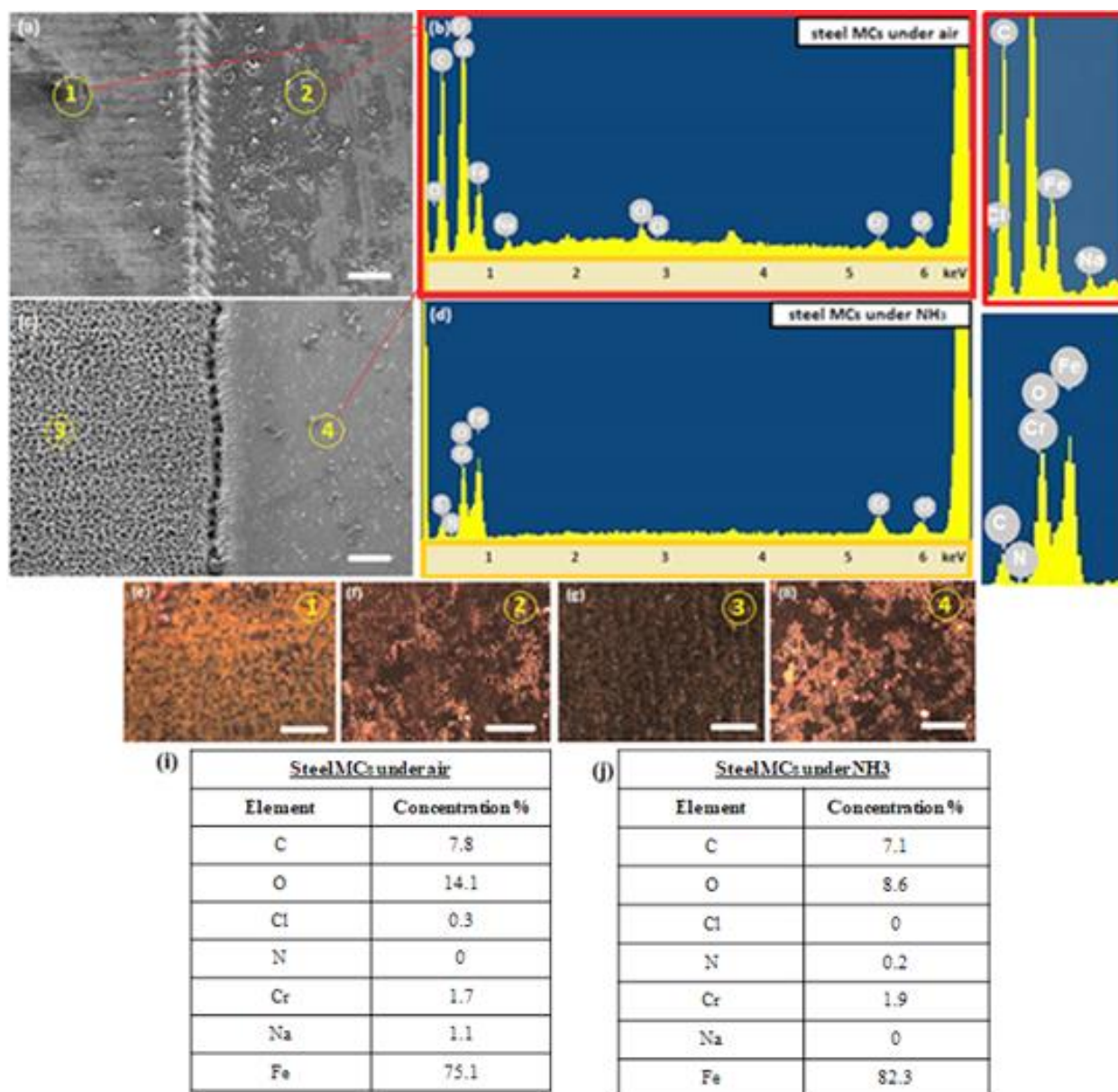


Figure 4.10 : (a) Top view SEM image of steel MCs fabricated in air, following the corrosion test (scale bar: 100 μm ; (b) EDS spectra from the regions 1,2 shown in (a). The corresponding elemental analysis is shown in (i); (c) Top view SEM image of steel MCs irradiated in NH_3 (scale bar: 100 μm); (d) EDS spectra from the region 3 shown in (c); The corresponding elemental analysis is shown in (j); (e-h) Microscope images of the regions 1-4 shown in the SEM images (a),(c) (scale bar : 100 μm).

Table 4.3 shows that the static contact angle values after the corrosion test, of the ammonia functionalized steel micro-nanostructured substrates, is in the range of 50 to 40 degrees for over 15 days. These values of C.A. are very close to these before the corrosion test (Table 4.2). This behavior was not observed in the case of air structured steel substrates, which became hydrophobic to super hydrophobic after 7 days of the corrosion test (Table 4.3). More specifically, the C.A. value of the air structured steel

surfaces, was larger than their measured C.A. value after the irradiation procedure (Table 4.2). The control substrates for the C.A. measurements, was the flat steel substrate. Micro-structured substrates were (5x5)mm and deionized Millipore water droplet's volume was stable to 3 μ l.

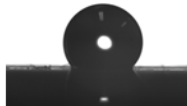
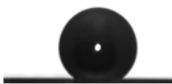


Days after corrosion test	1st	20th
<i>Air structured steel MCs</i>		
C.A. \pm S.D. (o)	130\pm4	140\pm 2
<i>NH₃ gaseous environment structured steel MCs</i>		
C.A. \pm S.D. (o)	50\pm4	43\pm4

Table 4.3 : Static contact angle (C.A.) measurements, after the corrosion test of steel MCs structures in air and gaseous NH₃ irradiation atmospheres for over 15 days after the test.

Figure 4.11 illustrates the oxidation of both air- (Fig. 4.11 a) and NH₃- (Fig. 4.11 b) steel MCs, and the untreated areas respectively, after one year of the irradiation procedures. These images show that the NH₃-steel MCs are dramatically less oxidized than the air-steel MCs.

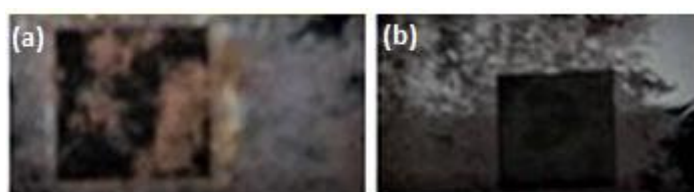


Figure 4.11: Photo-shoot of (a) air-structured steel MCs (black square) with the untreated area and (b) NH₃-structured steel MCs (black square) with the untreated area

5 Discussion & Conclusions

5.1 Micropatterned steel & silicon substrates fabricated via ultrashort-pulsed laser processing as artificial biomimetic surfaces

The fabrication of biomimetic surfaces constitutes a research area of great interest. The reason is the unique properties of these surfaces, which find numerous applications including nanoscale devices, water repellence, and self-cleaning surfaces, drag reduction in fluid flow, energy conversion and conservation, high adhesion, materials and fibers with high mechanical strength, antireflection and structural coloration¹.

Various methods have been developed for structuring surfaces and fabrication of micro-nano-patterned and hierarchical surfaces such as electron – beam lithography⁵, photolithography⁶, plasma treatments⁷. A promising technique for fabrication of micro structures with different scale topographies is irradiation using pulsed laser, with pulse duration lower than a second, i.e. short and ultra-short pulse. With proper setting of the laser parameters (e.g. fluence) and the environment (reactive gas), it is possible the formation of surfaces with different morphologies. The wetting³¹, optical¹⁵, microfluidic⁴ and surface properties¹⁴ of micro-structured silicon surfaces, have already studied.

The approach used in the present study involves the fabrication of microconical structured silicon surfaces by ultra-short pulsed laser processing. The aim was to investigate the optical properties of these surfaces, for different thicknesses of deposited layers on them via chemical process (thermal oxidation) and via coating of gold nanoparticles.

5.2 Irradiation parameters influence the surface micro-topography

The irradiation of a solid surface via ultra-short fs pulsed laser, lead to microstructures of various morphologies depending on the unique laser-matter interactions. Microstructuring by ultra-short pulsed lasers is an especially attractive approach, because it leads to the formation of arrays of high-aspect ratio microcones

(MCs) on solid surfaces¹⁶. Proper tuning of the laser (such as laser fluence, repetition rate, etc.) and reactive gas parameters (such as pressure) can lead to the formation of structures with different morphologies [Zorba V. et al., 2006¹⁶⁰].

In this study we have shown that by keeping constants four experimental parameters, (i.e. wavelength, repetition rate, irradiation environment and pulse duration) and by changing only the beam power, the surface micro-topography can change dramatically in a very controllable manner. Increased laser fluence (0.17-0.57J/cm²) lead to increased, MCs' height (3.21-13.81um) and the structures becoming more pronounced and spatially separated.

Furthermore, irradiation environment is a very important parameter for the topography of the substrates. We have already seen (BSc thesis) that, silicon substrates which have been irradiated in vacuum comprised blunt, irregular and shorter pikes than the ones which have been fabricated in reactive gas (SF₆) environment. On the other hand, steel substrates which have been irradiated in ambient air are larger and taller, than these that have been fabricated in ammonia gaseous (NH₃) environment. In the latter case, spikes were sharp and they exhibited on their surface roughness in the scale of nano-. So, the effect of irradiation environment, plays a distinct role to the nano-scale roughness and surface chemistry of the substrate, and hierarchical structures are created.

The surface response to the above parameters has been previously studied^{9,10,14}, with the same efficiency.

5.3 The influence of surface roughness on the optical properties of Si micropatterned surfaces

Si is a semiconductor commonly used in optoelectronic devices, such as solar cells and photodetector applications. However certain shortcomings make its use limited in certain types of applications; for example as an indirect bandgap material, it is a poor light emitter. Furthermore, the crystalline Si band gap (1.1 eV) makes its absorption and photoresponse to abruptly decrease for wavelengths typically above 1100 nm. This makes crystalline Si unsuitable for many near infrared applications, since it is insensitive to wavelengths that are extensively used for both telecommunications and

scientific instrumentation. Nevertheless, Si-based near infrared detectors could lower production costs and facilitate integration with other microelectronics. Also, the IR absorption has potential applications for the IR optoelectronic devices, such as IR image detector.

The optical properties of laser structured Si have been studied^{32,33}. The findings of these authors are almost exclusively based on studies of Si doping with sulfur via fs and ns pulsed lasers. We showed that laser structuring in the presence of SF₆ can increase substantially the absorption of Si in the visible and near infrared range.

Generally speaking, there are two ways to produce below-band gap absorption in ordinary Si; by introducing impurity atoms or by changing the structural order. First of all, impurity atoms bind electrons with a different potential and thus can introduce states in the band gap. On the other hand, structural changes cause deviations from the periodic crystal lattice and introduce electronic energy levels within the band gap. Transitions from, or to, these levels can then occur, which enable absorption of photons with below bandgap energies. Amorphous silicon (a-Si), polycrystalline silicon (poly-Si), and absorptance. [C.H. Seager et al.,1985¹⁶¹, W.B. Jackson et al.,1983¹⁶², W.B. Jackson and N.M. Amer,1982¹⁶³] damaged/deformed silicon exhibit below bandgap In all cases, the presence of significant disorder broadens the abrupt band edge of crystalline Si producing so called band tails of localized states extending into the gap.

For samples fabricated in in SF₆, there is an increased absorptance (close to 95 %) observed in the visible spectral range. The increased absorptance in the visible spectral range can be interpreted as a result of irradiation trapping between the intercone areas, leading to multiple reflections and thus to enhanced absorptance³³. This is in consistency to the observation that visible absorptance is not affected by thermal oxidation. The absorptance in the infrared spectral range, suggests an altered band structure associated with the introduction of sulphur impurity bands within the Si bandgap³³. A doping concentration of the order of 1%, [J.I. Pankove,1971¹⁶⁴] can induce states within the Si bandgap.

5.4 Surface functionality influence the optical response of Si micropatterned surfaces

In the previous section, the optical properties of black silicon were always discussed about bare silicon–air interface. However, a real world device usually requires the coating of the interface with some dielectric material either for the purpose of interface passivation or for the functionalization of the device. To take this circumstance into account we coated black silicon with SiO₂ layer, in different thicknesses, via dry thermal oxidation process which is a high-conformal method. Furthermore, we evaporated sphere and rod shaped AuNPs on oxidized black Si, because metal coatings are very promising for the improvement of optical response for many materials [Mehdi Keshavarz Hedayati et. al.,2016¹⁷³, Svetoslav Koynov et. al.,2006¹⁷⁴, Chee Leong Tan et al.,2012¹⁷⁵].

The oxidation of prepared black silicon structures is one of the most suitable passivation procedures, eliminating the negative influence of defective states created during the formation of black silicon structures. Our results shows that when a SiO₂ layer is deposited on black Si surface, reflectance and transmittance increases in the near IR regions. This means that absorbance decreases, but in the UV/Vis range there is a stable high absorbance efficiency behavior (97%).

It is very interesting that for 128nm thickness of SiO₂ layer, there is a saturation effect. More specifically, for layers thicker than 128nm transmittance reduces and absorbance increases, while for layers thinner than 128nm there is exactly the opposite effect. The decrease in the absorbance spectra can maybe attributed to bond rearrangement within the Si matrix caused by oxidation, rendering the sulphur impurities optically inactive, or because of defects of the SiO₂ layer. Structural inhomogeneities such as stretched, bent or broken bonds, stoichiometric conditions or ionic impurities at the SiO₂ interface can result in the formation of trap sites for charge carriers. Strained and broken bonds caused by the rate at which the oxide is grown would lead to the formation of carrier trap sites [J F Verwey,1990¹⁷⁶, Herbert R. Philipp,1979¹⁷⁷]. Also, the energy band change of Si due to SiO₂, is very important.

Metal nanoparticles (NPs) are well known to increase the efficiency of photovoltaic devices by reducing reflection and increasing light trapping within device. However, metal NPs on top flat surface suffer from high reflectivity losses

due to the backscattering of the NPs itself. The cone shaped of the micro-structures, the size of deposited metal NPs and their random deposition, can randomize the incident light direction within the structures. This leads to higher light collection and absorption of the incident light by creating multiple interactions of incident photon within the surface of the device, and also increases the path length of the incident light¹⁷⁵. This means that metal NPs on silicon structures allows light absorption close to 100% over a wavelength range of 300 nm to 1000 nm. By default, the presence of SiO₂ layer under the deposited AuNPs plays a distinct role, because we have seen that if the SiO₂ layer does not exist, we have a super absorbed surface which absorbs ~97% over a wavelength range of 250nm to 2000nm.

For different AuNPs shapes, there is a different behavior in R,T and A spectras in the near IR region (>1200 nm). We can conclude that the shape and the distribution of AuNPs affect the optical response of the structures. In our experiments the most dense distribution appears of sphere-shaped AuNPs with 7nm diameter and the most sparse distribution appears of rod-shaped AuNPs with aspect ratio 3:1.

We have presented a novel structure that exhibits unique optical properties, especially in the near IR region. This could find application on IR devices, photodiodes and solar cells with higher device efficiency.

5.5 The influence of surface chemistry on the wetting properties of steel micropatterned surfaces

Super-hydrophilic surfaces have attracted great attention due their interesting applications [⁴, N. Ren et. al.,2014¹⁶⁵, C. Byon et al.,2010¹⁶⁶]. Various methods have been developed for structuring solid surfaces with novel wetting properties, such as plasma treatment [R. Niemi et. al.,2010¹⁶⁷], surface coatings [A.M. McDonnell et.al.,2005¹⁶⁸] and chemical processing [D. Lattner and H. Jennissen,2009¹⁶⁹]. These methods are not “one-step” methods. Pulsed laser surface processing is an emerging, one-step, technique for the modification of surface wettability^{4,13,98}. This technique offers the opportunity to produce surfaces with superior wetting properties, such as improved corrosion resistance [²⁰, Bizi-bandoki et. al.,2013¹⁷⁰]. Different micro/nano-scale surface structures have been found to affect the surface functionality. These

structures include ripples, grooves and semi-periodic micro/nano structures (spikes or MCs)⁹⁸.

Steel is one of most widely used metals in industry for applications including personal care product vessels and chemical processing vessels. Thus, protection of steel from corrosion is of great technical importance. Controlling its wettability is useful for fluid contact control with the steel surfaces. Many studies have shown that the surface chemistry affects dramatically the wettability of the surface [S. Razi et al., 2016¹⁷¹, Y. Guan et. al., 2015¹⁷²]. The wettability of a metallic surface changes with time, due to the air room conditions which are exposed (organic/carbon material contamination), but during this process the surface roughness on microscale stays the same^{90,157}. Therefore, it is a challenge to maintain long-term hydrophilic characteristics on a metallic surface.

Femtosecond pulsed laser was irradiated, under air and ammonia gaseous atmospheres, on steel surfaces at controlled laser fluence, laser pulse duration and repetition rate. Laser-induced surface hydrophilic and anti-corrosive functionalities and their formation were investigated. After surface micro-structuring, under both air and ammonia gaseous atmospheres, MCs was successfully formed on the surface. MCs that formed under air atmosphere appeared hydrophobic behavior after 10 days of the irradiation procedure. In the opposite, ammonia functionalized steel MCs appeared super-hydrophilic behavior for over 130 days, after the irradiation procedure. Furthermore, after the corrosion procedure only the ammonia-structured surfaces remained hydrophilic and the formation of salty layer was not observed. Air-structured and flat steel samples became hydrophobic, which means that the corrosive medium affected them. Also the formation of salty layer was observed. To date, there is no reported work on generating a stable hydrophilic metallic surface using a simple process. In this work, long term super-hydrophilic steel surfaces were produced using fs laser surface structuring under NH₃ gaseous atmosphere. The findings from this study demonstrated the possibility of improving steel surface functionalities, by irradiating via a femtosecond pulsed laser under reactive gaseous atmosphere.

6 References

- [1] Stratakis, E. I., & Zorba, V. (2010). Biomimetic Artificial Nanostructured Surfaces. *Nanomaterials for the Life Sciences* (Vol. 7).
- [2] Xia, F., & Jiang, L. (2008). Bio-inspired, smart, multiscale interfacial materials. *Advanced Materials*, 20(15), 2842–2858.
- [3] Alberts B, Johnson A, Lewis J, Raff M, Roberts K, Walter P (eds) (2008) *Molecular biology of the cell*. Garland Science, New York
- [4] Stratakis, E., Ranella, A., & Fotakis, C. (2011). Biomimetic micro/nanostructured functional surfaces for microfluidic and tissue engineering applications. *Biomicrofluidics*, 5(1), 1–31.
- [5] E. Martines, K. Seunarine, H. Morgan, N. Gadegaard, C. D. W. Wilkinson, and M. O. Riehle, *Nano Lett.* 5, 2097 (2005).
- [6] J.-Y. Shiu, C.-W. Kuo, P. Chen, and C.-Y. Mou, *Chem. Mater.* 16, 561 (2004).
- [7] I. Woodward, W. C. E. Schofield, V. Roucoules, and J. P. S. Badyal, *Langmuir* 19, 3432 (2003).
- [8] Bhushan, B., Jung, Y. C., & Koch, K. (2009). Micro-, nano- and hierarchical structures for superhydrophobicity, self-cleaning and low adhesion. *Philosophical Transactions. Series A, Mathematical, Physical, and Engineering Sciences*, 367(1894), 1631–1672.
- [9] Zorba, V., Boukos, N., Zergioti, I., & Fotakis, C. (2008). Ultraviolet femtosecond, picosecond and nanosecond laser microstructuring of silicon: structural and optical properties. *Applied Optics*, 47(11), 1846–1850.
- [10] Her, T. H., Finlay, R. J., Wu, C., Deliwala, S., & Mazur, E. (1998). Microstructuring of silicon with femtosecond laser pulses. *Applied Physics Letters*, 73(12), 1673–1675.
- [11] Zorba, V., Tzanetakis, P., Fotakis, C., Spanakis, E., Stratakis, E., Papazoglou, D. G., & Zergioti, I. (2006). Silicon electron emitters fabricated by ultraviolet laser pulses. *Applied Physics Letters*, 88(8).
- [12] Simitzi, C., Efstathopoulos, P., Kourgiantaki, A., Ranella, A., Charalampopoulos, I., Fotakis, C., Gravanis, A. (2015). Laser fabricated discontinuous anisotropic microconical substrates as a new model scaffold to control the directionality of neuronal network outgrowth. *Biomaterials*, 67, 115–128.
- [13] Zorba, V., Stratakis, E., Barberoglou, M., Spanakis, E., Tzanetakis, P., Anastasiadis, S. H., & Fotakis, C. (2008). Biomimetic artificial surfaces quantitatively reproduce the water repellency of a lotus leaf. *Advanced Materials*, 20(21), 4049–4054.
- [14] Simitzi, C., Stratakis, E., Fotakis, C., Athanassakis, I., & Ranella, A. (2015). Microconical silicon structures influence NGF-induced PC12 cell morphology. *Journal of Tissue Engineering and Regenerative Medicine*, 9(4), 424–434.
- [15] Rudenko, A., Colombier, J., & Itina, T. E. (2016). Influence of Polarization State on Ultrafast Laser-Induced Bulk Nanostructuring. *Journal of Laser Micro/Nanoengineering*, 11(3), 304–311.
- [16] Stratakis, E. (2012). *Nanomaterials by Ultrafast Laser Processing of Surfaces*, 4, 407–431.
- [17] Whitesides, G. M. (2006). The origins and the future of microfluidics. *Nature*, 442(7101), 368–73.

- [18] Koch, K., Bhushan, B., & Barthlott, W. (2008). Diversity of structure, morphology and wetting of plant surfaces. *Soft Matter*, 4(10), 1943.
- [19] Guo, Z., Liu, W., & Su, B. L. (2011). Superhydrophobic surfaces: From natural to biomimetic to functional. *Journal of Colloid and Interface Science*, 353(2), 335–355.
- [20] Trdan, U.; Hočevár, M.; Gregorčič, P. (2017) Transition from superhydrophilic to superhydrophobic state of laser textured stainless steel surface and its effect on corrosion resistance. *Corros. Sci.*, 123, 21–26 .
- [21] Rajab, F. H., Liu, Z., & Li, L. (2018). Applied Surface Science Production of stable superhydrophilic surfaces on 316L steel by simultaneous laser texturing and SiO₂ deposition. *Applied Surface Science*, 427, 1135–1145.
- [22] Karthick, B., & Maheshwari, R. (2008). Lotus-inspired nanotechnology applications. *Resonance*, 13(12), 1141–1145.
- [23] Vukusic, P., & Sambles, J. R. (2003). Photonic structures in biology. *Nature*, 424(6950), 852–5.
- [24] Rossiter, J., Yap, B., & Conn, A. (2012). Biomimetic chromatophores for camouflage and soft active surfaces. *Bioinspir Biomim*, 7(3), 36009.
- [25] Morhard, C., Pacholski, C., Lehr, D., Brunner, R., Helgert, M., Sundermann, M., & Spatz, J. P. (2010). Tailored antireflective biomimetic nanostructures for UV applications. *Nanotechnology*, 21(42), 425301.
- [26] Stuart A. Boden and Darren M. Bagnall , Natural Moth-eye. “Moth-Eye Antireflective Structures,” 2015.
- [27] Boden, Stuart A, and Darren M Bagnall (2009) “Nanostructured Biomimetic Moth-Eye Arrays in Silicon by Nanoimprint Lithography.” In *Proc. SPIE7401 J*, edited by Raul J. Martin-Palma and Akhlesh Lakhtakia, 74010:74010J.
- [28] Siddique, Radwanul Hasan, Guillaume Gomard, and Hendrik Hölscher. “The Role of Random Nanostructures for the Omnidirectional Anti-Reflection Properties of the Glasswing Butterfly.” *Nature Communications* 6, no. November (2015).
- [29] Watanabe, Keiichiro, Takayuki Hoshino, Kazuhiro Kanda, Yuichi Haruyama, and Shinji Matsui. “Brilliant Blue Observation from a Morpho-Butterfly-Scale Quasi-Structure.” *Japanese Journal of Applied Physics, Part 2: Letters* 44, no. 1–7 (2005).
- [30] Bonse, J. et al. “Femtosecond laser-induced periodic surface structures on steel and titanium alloy for tribological applications”, *Appl. Phys.* A117, 103–110 (2014) .
- [31] Hermens, U., S.V. Kirner, C. Emonts, P. Comanns, E. Skoulas, A. Mimidis, H. Mescheder, et al. “Mimicking Lizard-like Surface Structures upon Ultrashort Laser Pulse Irradiation of Inorganic Materials.” *Applied Surface Science*, 2016.
- [32] Crouch, C. H., J. E. Carey, J. M. Warrender, M. J. Aziz, E. Mazur, and F. Y. Génin. “Comparison of Structure and Properties of Femtosecond and Nanosecond Laser-Structured Silicon.” *Applied Physics Letters* 84, no. 11 (2004): 1850–52.
- [33] Crouch, C. H., J. E. Carey, M. Shen, E. Mazur, and F. Y. Génin. “Infrared Absorption by Sulfur-Doped Silicon Formed by Femtosecond Laser Irradiation.” *Applied Physics A: Materials Science and Processing* 79, no. 7 (2004): 1635–41.

- [34] Janzén, E., R. Stedman, G. Grossmann, and H. G. Grimmeiss. "High-Resolution Studies of Sulfur- and Selenium-Related Donor Centers in Silicon." *Physical Review B* 29, no. 4 (1984): 1907–18.
- [35] Nolte, S, C Momma, H Jacobs, A Tu, B N Chichkov, B Wellegehausen, and H Welling. "Ablation of Metals by Ultrashort Laser Pulses." *Journal of the Optical Society of America B* 14, no. 10 (1997): 2716–22.
- [36] Jost, D., W. Lüthy, H. P. Weber, and R. P. Salathé. "Laser Pulse Width Dependent Surface Ripples on Silicon." *Applied Physics Letters* 49, no. 11 (1986): 625–27.
- [37] Henyk, M., N. Vogel, D. Wolfframm, A. Tempel, and J. Reif. "Femtosecond Laser Ablation from Dielectric Materials: Comparison to Arc Discharge Erosion." *Applied Physics A: Materials Science and Processing* 69, no. 7 (1999): 355–58.
- [38] Barberoglou, M., G. D. Tsibidis, D. Gray, E. Magoulakis, C. Fotakis, E. Stratakis, and P. A. Loukakos. "The Influence of Ultra-Fast Temporal Energy Regulation on the Morphology of Si Surfaces through Femtosecond Double Pulse Laser Irradiation." *Applied Physics A: Materials Science and Processing* 113, no. 2 (2013): 273–83.
- [39] Jing-tao , Z H U, Zhao Ming, Y I N Gang, Zhao Li, and Chen De-ying. "Silicon Micro-Structuring Using Ultra-Short Laser Pulses" 5629 (n.d.): 11–14.
- [40] J.F.Young, J.E. Sipe, H.M. van Driel, *Phys. Rev. B* 30(4) , 2001 (1984).
- [41] Sukumar Basu , *Crystalline Silicon – Properties and Uses*, 2011
- [42] Voldman J, Gray ML, Schmidt MA, 1999, *Microfabrication in biology and medicine*, *Annu Rev.Biomed Eng*, 1:401.
- [43] Sievila P, 2013, *Microfabrication technologies for single-crystal sensors*, PhD thesis, Aalto University
- [44] Pearce TM, Williams JC, 2007, *Microtechnology: Meet neurobiology, Lab on a Chip*, 7:30.
- [45] Stratakis, E. "Nanomaterials by Ultrafast Laser Processing of Surfaces." *Science of Advanced Materials* 4 (2012): 407–31.
- [46] Hunt LP, 1990, *Silicon Precursors: Their Manufacture and Properties In Handbook of semiconductor silicon technology*, ed. WC O'Mara, RB Herring, LP Hunt, Noyes Publications
- [47] Brown, P. J. "The Crystal Structure of Solids." *Physics Today* 27 (1974): 50.
- [48] B.G. Streetman, *Solid State Electronics*, Third Edition, Chapter 1, Prentice Hall, 1990.
- [49] F. J. Himpsel, F.R.Mc Feely, A.Taleb-Ibrahimi and J.A.Yarmoff, *Physical Review B*, Vol.38, No.9, pp.6084-6095 (1988)
- [50] M. Razeghi *Technology of Quantum Devices* pp.42 LLC (2010), Springer, ISBN 978-1-4419-1055-4.
- [51] Hierlemann A, *Thermal Oxidation of Silicon, Microtechnology and microelectronics*.
- [52] Logofatu, C., C. C. Negrila, R. V. Ghita, F. Ungureanu, C. Cotirlan, C. G. Adrian Lazarescu, M. Stefan, and M. Florin. *Study of SiO₂/Si Interface by Surface Techniques. Crystalline Silicon - Properties and Uses*, 2011.

- [53] B.E. Deal and A.S. Grove, "General Relationship for the Thermal Oxidation of Silicon," J. Appl. Physics., 36 , 3770 (1965).
- [54] Sze SM, 2002, Semiconductor Devices, Physics and Technology, Wiley
- [55] Carrier, P.; Lewis, L.J. & Dharma-Wardana, M.W.C. (2002). Optical properties of structurally relaxed Si/SiO₂ superlattices: The role of bonding at interfaces, Phys. Rev. B65, pp.165339-165350.
- [56] Morita, M., T. Ohmi, E. Hasegawa, M. Kawakami, and M. Ohwada. "Growth of Native Oxide on a Silicon Surface." Journal of Applied Physics 68, no. 3 (1990): 1272–81.
- [57] G. S. Henderson, D. R. Baker, (eds, . Synchrotron, Earth. Radiation, Environmental, Sciences. Material, Short. Applications, Series. 3. Course, Association. Mineralogical, Canada. of, (2002)159-178. Henderson G. S., The Geochemical News, 113 113 October (2002), 13.
- [58] William D. Callister, Jr. (2001), "Fundamentals of Materials Science and Engineering An Interactive", 5th edition
- [59] E. Magoulakis, E. L. Papadopoulou, E. Stratakis, C. Fotakis, and P. A. Loukakos, Appl. Phys. A. 98, 701 (2010).
- [60] A.C. Tien, S. Backus, H. Kapteyn, M. Mourane, G. Mourou, Phys. Rev. Lett. 82, 3883 (1999).
- [61] Lucas, L. and J. Zhang, Femtosecond laser micromachining: a back-to-basics primer. 2012.
- [62] Y.C. Koji Sugioka, Ultrafast Laser Processing: From Micro- to Nanoscale, 2013.
- [63] M. Birnbaum, "Semiconductor Surface Damage Produced by Ruby Lasers", J. Appl. Phys. 36, 3688 (1965).
- [64] D. C. Emmony, R. P. Howson, L. J. Willis, "Laser mirror damage in germanium at 10.6 μm ", Appl. Phys. Lett. 23, 598 (1973).
- [65] H. J. Leamy, G. A. Rozgonyi, T. T. Sheng, G. K. Celler, "Periodic regrowth phenomena produced by laser annealing of ion-implanted silicon", Appl. Phys. Lett. 32, 535 (1978).
- [66] P. M. Fauchet, A. E. Siegman, "Surface ripples on silicon and gallium arsenide under picosecond laser illumination", Appl. Phys. Lett. 40, 824 (1981).
- [67] T. E. Zavecz, M. A. Saifi, "Metal reflectivity under high-intensity optical radiation", Appl. Phys. Lett. 26, 165 (1975).
- [68] J. C. Koo, R. E. Slusher, "Diffraction from laser-induced deformation on reflective surfaces ", Appl. Phys. Lett. 28, 614 (1976).
- [69] N. R. Isenor, "CO₂ laser-produced ripple patterns on Ni_xP_{1-x} surfaces", Appl. Phys. Lett. 31, 148 (1977).
- [70] A. K. Jain, V. N. Kulkarni, D. K. Sood, J.S. Uppal, "Periodic surface ripples in laser-treated aluminum and their use to determine absorbed power", J. Appl. Phys. 52, 4882 (1981).
- [71] P. A. Temple, M. J. Soileau, "Polarization change model for laser-induced ripple patterns in dielectric materials", IEEE J. Quant. Elec. QE-17, 2067 (1981).

- [72] M. Huang, F. L. Zhao, Y. Cheng, N. S. Xu, and Z. Z. Xu, “Origin of Laser-Induced Near-Subwavelength Ripples: Interference between Surface Plasmons and Incident Laser”, *ACS Nano* 3, 4062 (2009).
- [73] A. Latif, M.S. M.A. Aleem, M.S. Rafique, M. Khaleeq-Ur-Rahman, “Influence of number of laser shots on laser induced microstructures on Ag and Cu targets”, *Laser and Particle Beams*, 27, 129, (2009).
- [74] D. Bäuerle, “Laser Processing and Chemistry”, Third Edition, Springer-Verlag Berlin Heidelberg New York (2000).
- [75] Tsibidis, George D., C. Fotakis, and E. Stratakis. “From Ripples to Spikes: A Hydrodynamical Mechanism to Interpret Femtosecond Laser-Induced Self-Assembled Structures.” *Physical Review B* 92, no. 4 (July 9, 2015): 41405.
- [76] S. Sakabe, M. Hashida, S. Tokita, S. Namba, and K. Okamuro, *Phys. Rev. B* 79, 033409 (2009).
- [77] S. Clark, D.C. Emmony, *Phys. Rev. B.* 40, 2031 (1989).
- [78] Tsibidis, George D., Evangelos Skoulas, Antonis Papadopoulos, and Emmanuel Stratakis. “Convection Roll-Driven Generation of Supra-Wavelength Periodic Surface Structures on Dielectrics upon Irradiation with Femtosecond Pulsed Lasers.” *Physical Review B - Condensed Matter and Materials Physics* 94, no. 8 (2016): 2–6.
- [79] J. Zenneck, *Ann. Phys. Leipz.* 23, 846-866 (1907).
- [80] R. H. Ritchie, “Plasma Losses by Fast Electrons in Thin Films”, *Phys. Rev.* 106, 874–881 (1957).
- [81] Pedraza AJ, Fowlkes JD, Lowndes DH, 1999, Silicon microcolumn arrays grown by nanosecond pulsed-excimer laser irradiation, *Phys. Lett.* , 74:2322
- [82] Dolgaev SI, Lavrishev SV, Lyalin AA, Simakin AV, Voronov VV, Shafeev GA, 2001, Formation of conical microstructures upon laser evaporation of solids, *Applied Physics A: Materials Science & Processing*, 73:177.
- [83] Zorba V, Persano L, Pisignano D, Athanassiou A, Stratakis E, et al, 2006, Making silicon hydrophobic: wettability control by two-lengthscale simultaneous patterning with femtosecond laser irradiation, *Nanotechnology*, 17:3234.
- [84] T.-H. Her, R. J. Finlay, C. Wu, S. Deliwala, E. Mazur, *Appl. Phys. Lett.* 1998, 73, 1673.
- [85] Bates Robert L, P L Stephan Thamban, Matthew J Goeckner, and Lawrence J Overzet. “Silicon Etch Using SF₆/C₄F₈/Ar Gas Mixtures,” 2014, 0–11.
- [86] Lii, Y.-J., J. Jorné, K.-C. Cadien, and J.-E. Schoenholtz Jr. “Plasma Etching of Silicon in SF₆.” *J. Electrochem. Soc.* 137, no. 11 (1990): 3633.
- [87] J.D.Fowlkes, A.J.Pedraza, D.H.Lowndes, *Appl. Phys. Lett.* 77, 1629 (2000).
- [88] M. MEZERA and G.R.B.E. RÖMER, “Model based optimization of process parameters to produce large homogeneous areas of laser-induced periodic surface structures”, *Optics Express*, 6012, 27, No. 15, 2019.
- [89] Sabri Alamri, Fotis Fraggelakis, Tim Kunze, Benjamin Krupop, Girolamo Mincuzzi, Rainer Kling and Andrés Fabián Lasagni, “On the Interplay of DLIP and LIPSS Upon Ultra-Short Laser Pulse Irradiation”, *Materials* 2019, 12

- [90] Kietzig A, Hatzikiriakos S, Englezos P. Patterned superhydrophobic metallic surfaces. *Langmuir* 2009;25:4821–7.
- [91] Wennerberg A, Albrektsson T, Johansson C, Andersson B. Experimental study of turned and grit-blasted screw-shaped implants with special emphasis on effects of blasting material and surface topography. *Biomaterials* 1996;17:15–22.
- [92] Bathomarco R, Solorzano G, Elias C, Prioli R. Atomic force microscopy analysis of different surface treatments of Ti dental implant surfaces. *Appl Surf Sci* 2004;233:29–3.
- [93] Madore C, Piotrowski O, Landolt D. Through-mask electrochemical micromachining of titanium. *J Electrochem Soc* 1999;146:2526–32.
- [94] Sano T, Yanai M, Ohmura E, Nomura Y, Miyamoto I, Hirose A, et al. Femtosecond laser fabrication of microspike-arrays on tungsten surface. *Appl Surf Sci* 2005;247:340–6.
- [95] Gaggl A, Schultes G, Muller W, Karcher H. Scanning electron microscopical analysis of laser-treated titanium implant surfaces—a comparative study. *Biomaterials* 2000;21:1067–73.
- [96] Bereznai M, Pelsoczi I, Toth Z, Turzo K, Radnai M, Bor Z, et al. Surface modifications induced by ns and sub-ps excimer laser pulses on titanium implant material. *Biomaterials* 2003;24:4197–203.
- [97] Chichkov B, Momma C, Nolte S, von Alvensleben F, Tunnermann A. Femtosecond, picosecond and nanosecond laser ablation of solids. *Appl Phys A* 1996;63:109–15.
- [98] Hermens, U., Kirner, S. V, Emonts, C., Comanns, P., Skoulas, E., Mimidis, A., Meschedera H., Winandsa K., Krügerb J., Stratakis E., Bonse, J. (2017). “Mimicking lizard-like surface structures upon ultrashort laser pulse irradiation of inorganic materials”, *Applied Surface Science*, 418, 499–507.
- [99] S. V. Kirner, U. Hermens, A. Mimidis, E. Skoulas, C. Florian, F. Hischen, C. Plamadeala, W. Baumgartner, K. Winands, H. Mescheder, J. Krüger, J. Solis, J. Siegel, E. Stratakis, J. Bonse (2017). Mimicking bug-like surface structures and their fluid transport produced by ultrashort laser pulse irradiation of steel. *Applied Physics A*, 123(12), 1–13.
- [100] Schmidt V, Husinsky W, Betz G. Dynamics of laser desorption and ablation of metals at the threshold on the femtosecond time scale. *Physical Review Letters* 2000;85:3516–9.
- [101] Barada K. Nayak and Mool C. Gupta, ” Self-organized micro/nano structures in metal surfaces by ultrafast laser irradiation”, *Optics and Lasers in Engineering* 48 (2010) 940–949.
- [102] P. Pou, J. del Val, A. Riveiro, R. Comesaña, F. Arias-González, F. Lusquiños, M. Bountinguiza, F. Quintero, J. Pou (2018). Laser texturing of stainless steel under different processing atmospheres: From superhydrophilic to superhydrophobic surfaces. *Applied Surface Science*.
- [103] T. van der Heyden, J.M. Díaz, *Arquivos Entomológicos* 15, 371–373 (2016).
- [104] Mody VV, Siwale R, Singh A, Mody HR. 2010. Introduction to metallic nanoparticles. *J Pharm Bioall Sci*. 2: 282–9.
- [105] Salata OV. 2004. Applications of nanoparticles in biology and medicine. *J Nanobiotechnol*. 2 : 3.
- [106] Thakkar KN, Mhatre SS, and Parikh RY. 2010. Biological synthesis of metallic nanoparticles. *Nanomedicine*. 6 : 257 – 262.
- [107] Vollath, D. “Introduction to Nanoparticles and Nanomaterials,” 2013, 1–24.

- [108] Zhou, Jingfang, John Ralston, Rossen Sedev, and David A. Beattie. "Functionalized Gold Nanoparticles: Synthesis, Structure and Colloid Stability." *Journal of Colloid and Interface Science* 331, no. 2 (2009): 251–62.
- [109] Sperling R. and W. J. Parak. "Surface Modification, Functionalization and Bioconjugation of Colloidal Inorganic Nanoparticles." *Philosophical Transactions. Series A, Mathematical, Physical, and Engineering Sciences* 368, no. 1915 (2010).
- [110] Kumar, S, K S Gandhi, and R Kumar. "Modeling of Formation of Gold Nanoparticles by Citrate Method." *Industrial & Engineering Chemistry Research* 46, no. 10 (2007): 3128–36.
- [111] Turkevich, J.; Stevenson, P.; Hillier, J. A Study of the Nucleation and Growth Process in the Synthesis of Colloidal Gold. *Discuss. Faraday Soc.* 1951, 11, 55.
- [112] Muhlforth, H. The Preparation of Colloidal Gold Particles Using Tannic Acid as an Additional Reducing Agent. *Experientia* 1982, 38, 1127.
- [113] Brust, M.; Walker, M.; Bethell, D.; Schiffrin, D. J.; Whyman, R. Synthesis of Thiol-Derivatised Gold Nanoparticles in a Two-Phase Liquid-Liquid System. *Chem. Commun.* 1994, 801.
- [114] U. Drechsler, N. O. Fischer, B. L. Frankamp and V. M. Rotello, *Adv. Mater.*, 2004, 16, 271–274.
- [115] Reetz MT, Helbig W, Quaiser SA, Stimming U, Breuer N, Vogel R. 1995. Visualization of surfactants on nanostructured palladium clusters by a combination of STM and high-resolution TEM. *Science*. 267 : 367 – 369.
- [116] Reetz MT, Helbig W. 1994. Size-selective synthesis of nanostructured transition metal clusters. *J Am Chem Soc.* 116: 7401– 7402.
- [117] Jana NR, Gearheart L, Murphy CJ. 2001. Seeding growth for size control of 5 – 40 nm diameter gold nanoparticles. *Langmuir*. 17 : 6782 – 6786.
- [118] Das RK, Gogoi N, Bora U. 2011. Green synthesis of gold nanoparticles using *Nyctanthes arbortristis* flower extract. *Bioprocess Biosyst Eng.* 34 : 615 – 619.
- [119] Smitha SL, Philip D, Gopchandran KG. 2009. Green synthesis of gold nanoparticles using *Cinnamomum zeylanicum* leaf broth. *Spectrochim Acta A Mol Biomol Spectrosc.* 74 : 735 – 739.
- [120] Itoh H, Naka K, Chujo Y. 2004. Synthesis of gold nanoparticles modified with imidazole based on the imidazolium cation. *J Am Chem Soc.* 126: 3026– 3027.
- [121] Eustis Susie, and Mostafa El-Sayed. "Why Gold Nanoparticles Are More Precious than Pretty Gold: Noble Metal Surface Plasmon Resonance and Its Enhancement of the Radiative and Nonradiative Properties of Nanocrystals of Different Shapes." *Chemical Society Reviews* 35, no. 3 (2006): 209–17.
- [122] Yeh, Yi-Cheun, Brian Creran, and Vincent M Rotello. "Gold Nanoparticles: Preparation, Properties, and Applications in Bionanotechnology." *Nanoscale* 4, no. 6 (2012): 1871–80.
- [123] Tiwari PM, Vig K, Dennis VA, Singh SR. 2011. Functionalized gold nanoparticles and their biomedical applications. *Nanomaterials*. 1 : 31 – 63.
- [124] Shah M, V Badwaik, Y Kherde, H K Waghvani, T Modi, Z P Aguilar, H Rodgers, et al. "Gold Nanoparticles: Various Methods of Synthesis and Antibacterial Applications." *Front Biosci (Landmark Ed)* 19, no. May 2015 (2014): 1320–44.

- [125] Majidi, Sima, Fatemeh Zeinali Sehrig, Samad Mussa Farkhani, Mehdi Soleymani Goloujeh, and Abolfazl Akbarzadeh. "Current Methods for Synthesis of Magnetic Nanoparticles." *Artificial Cells, Nanomedicine, and Biotechnology* 44, no. 2 (2016): 722–34.
- [126] Hu M, Chen J, Li ZY, Au L, Hartland GV, Li X, et al. 2006. Gold nanostructures: engineering their plasmonic properties for biomedical applications. *Chem Soc Rev.* 35: 1084–1094.
- [127] Hubert, C., L. Billot, P. M. Adam, R. Bachelot, P. Royer, J. Grand, D. Gindre, K. D. Dorkenoo, and A. Fort. "Role of Surface Plasmon in Second Harmonic Generation from Gold Nanorods." *Applied Physics Letters* 90, no. 18 (2007): 89–92.
- [128] Pong, Boon Kin, Hendry I. Elim, Jian Xiong Chong, Wei Ji, Bernhardt L. Trout, and Jim Yang Lee. "New Insights on the Nanoparticle Growth Mechanism in the Citrate Reduction of gold(III) Salt: Formation of the Au Nanowire Intermediate and Its Nonlinear Optical Properties." *Journal of Physical Chemistry C* 111, no. 17 (2007): 6281–87.
- [129] Chee Leong Tan, Sung Jun Jang and Yong Tak Lee, "Localized surface plasmon resonance with broadband ultralow reflectivity from metal nanoparticles on glass and silicon subwavelength structures", 2012, Optical Society of America.
- [130] Cesario, J.; Quidant, R.; Badenes, G.; Enoch, S. Electromagnetic coupling between a metal nanoparticle grating and a metallic surface. *Opt. Lett.* **2005**, 30, 3404–3406.
- [131] Mehdi Keshavarz Hedayati, Franz Faupel and Mady Elbahri, "Review of Plasmonic Nanocomposite Metamaterial Absorber", *Materials* 2014, 7, 1221-1248.
- [132] C.A. Grimes, E.C. Dickey, M.V. Pishko, *Encyclopedia of sensors*. American Scientific Publishers; 2006.
- [133] H. B. Liao, "Preparation and optical characterization of Au/SiO₂ composite films with multilayer structure", *Journal of Applied Physics*, 2003, 98, 8.
- [134] A. Ranjgar, R. Norouzi, A. Zolanvari, and H. Sadeghi, "Characterization and optical absorption properties of plasmonic nanostructured thin films", *Armenian Journal of Physics*, 2013, vol. 6, issue 4, pp. 198-203.
- [135] Dongdong Lin et. al., "Large-Area Au-Nanoparticle-Functionalized Si Nanorod Arrays for Spatially Uniform Surface- Enhanced Raman Spectroscopy", *ACS Nano* 2017, 11, 1478–1487.
- [136] E.H. Nicollins and J.R. Brews, *MOS Physics and Technology*. New York: Wiley, 1952.
- [137] Biver, T., A. Corti, N. Eltugral, E. Lorenzini, M. Masini, A. Paolicchi, A. Pucci, G. Ruggeri, F. Secco, and M. Venturini. "Analysis of 4-Dimethylaminopyridine (DMAP)-Gold Nanoparticles Behaviour in Solution and of Their Interaction with Calf Thymus DNA and Living Cells." *Journal of Nanoparticle Research* 14, no. 2 (2012).
- [138] Hersel, Ulrich, Claudia Dahmen, and Horst Kessler. "RGD Modified Polymers: Biomaterials for Stimulated Cell Adhesion and beyond." *Biomaterials* 24, no. 24 (2003): 4385–4415.
- [139] Lévy, Raphaël, Nguyen T K Thanh, R. Christopher Doty, Irshad Hussain, Richard J. Nichols, David J. Schiffrin, Mathias Brust, and David G. Fernig. "Rational and Combinatorial Design of Peptide Capping Ligands for Gold Nanoparticles." *Journal of the American Chemical Society* 126, no. 32 (2004): 10076–84.
- [140] Hermanson Gerg T., *Bioconjugate techniques*, 2nd edition.

- [141] Hasan, B. O. (2010). Effect of Salt Content on The Corrosion Rate of Steel Pipe in Turbulently Flowing Solutions, College of Engineering Journal, 13(1), 66–73.
- [142] Cortadellas N, Fernández E, Garcia A. 2012. Biomedical and Biological Applications of Scanning Electron Microscopy. Handbook of instrumental techniques. Scientific and Technological Centers of the University of Barcelona.
- [143] John Wiley & Sons Ltd, Energy dispersive spectroscopy, Second edition 2015, The Atrium, Southern Gate, Chichester, West Sussex, PO19 8SQ.
- [144] P.G. De Gennes, Rev. Mod. Phys. 57, 827 (1985).
- [145] L. Leger, J.F. Joanny, Rep. Prog. Phys. 55, 431 (1992).
- [146] G. McHale, N.J. Shirtcliffe, M.I. Newton, Langmuir 20, 10146 (2004)
- [147] R. N. Wenzel, Ind. Eng. Chem. 28, 988 (1936).
- [148] A. B. D. Cassie, S. Baxter, Trans. Faraday. Soc., 40, 546 (1944).
- [149] Chauhan, Sourabh Singh. “Ellipsometry for Measuring the Thickness of Thin Films,” n.d., 2014.
- [150] By, Published. “World βETM S Largest Science , Technology & Medicine Open Access Book Publisher Infrared Spectroscopic Ellipsometry for Ion-Implanted Silicon Wafers,” n.d.
- [151] Débora Gonçalves and Eugene A. Irene, FUNDAMENTALS AND APPLICATIONS OF SPECTROSCOPIC ELLIPSOMETRY, Quím. Nova vol.25 no.5 São Paulo Sept./Oct. 2002.
- [152] R.M.A. Azzam, N.M. Bashara “Ellipsometry and polarized light”, North Holland , Amsteram, 1977.
- [153] J. M. Palmer, Handbook of Optics (McGraw-Hill, 1995).
- [154] R. Menzel, Photonics: Linear and Nonlinear Interactions of Laser Light and Matter, .Springer-Verlag Berlin Heidelberg (2001).
- [155] Ji, Yi-Qin, Yu-Gang Jiang, Hua-Song Liu, Li-Shuan Wang, Dan-Dan Liu, Cheng-Hui Jiang, Rong-Wei Fan, and De-Ying Chen. “Optical Constants of SiO₂ Films Deposited on Si Substrates.” Chinese Physics Letters 31, no. 4 (2014): 46401.
- [156] Ketan K Ladava1, Nandkishor R Dadhania, Anand P Sarvaiya, “PHOTONIC DESIGN FOR PHOTOVOLTAIC CELL”, IJARIE-ISSN(O)-2395-4396, Vol-4 Issue-2, 2018.
- [157] J. Long, M. Zhong, P. Fan, D. Gong, H. Zhang, Wettability conversion of ultrafast laser structured copper surface, J. Laser Appl. 27 (2015) S29107.
- [158] Burns, R. M. (6AD). Chemical reactions in the corrosion of metals. New England Association of Chemistry Teachers, 8, 318–321.
- [159] Hasan, B. O. (2010). Effect of Salt Content on The Corrosion Rate of Steel Pipe in Turbulently Flowing Solutions, College of Engineering Journal, 13(1), 66–73.
- [160] Zorba V, Persano L, Pisignano D, Athanassiou A, Stratakis E, et al, 2006, Making silicon hydrophobic: wettability control by two-lengthscale simultaneous patterning with femtosecond laser irradiation, Nanotechnology, 17:3234.
- [161] C.H. Seager, P. M. Lenahan, K. L. Brower, and R.E. Mikawa, J. Appl. Phys. **58**, 2704 (1985).

- [162] W.B. Jackson, N.M. Johnson, D.K. Biegelsen, *Appl. Phys. Lett.* **43**, 195 (1983).
- [163] W.B. Jackson and N.M. Amer. *Phys. Rev. B* **25**, 5559 (1982).
- [164] J.I. Pankove, *Optical Processes In Semiconductors* (New York: Dover Publications, Inc. 1971).
- [165] N. Ren, J. Li, J. Qiu, Y. Sang, H. Jiang, R.I. Boughton, L. Huang, W. Huang, H. Liu, Nanostructured titanate with different metal ions on the surface of metallic titanium: a facile approach for regulation of rBMSCs fate on titanium implants, *Small* **10** (2014) 3169–3180.
- [166] C. Byon, Y. Nam, S.J. Kim, Y.S. Ju, Drag reduction in stokes flows over spheres with nanostructured superhydrophilic surfaces, *J. Appl. Phys.* **107** (2010) 066102.
- [167] R. Niemi, A. Mahiout, J. Siivinen, R. Mahlberg, J. Likonen, J. Nikkola, J. Mannila, T. Vuorio, L.S. Johansson, O. Söderberg, S.P. Hannula, Surface pretreatment of austenitic stainless steel and copper by chemical, plasma electrolytic or CO₂ cryoblasting techniques for sol-gel coating, *Surf. Coat. Technol.* **204** (2010) 2424–2431.
- [168] A.M. McDonnell, D. Beving, A. Wang, W. Chen, Y. Yan, Hydrophilic and antimicrobial zeolite coatings for gravity-independent water separation, *Adv. Funct. Mater.* **15** (2005) 336–340.
- [169] D. Lattner, H. Jennissen, Preparation and properties of ultra-hydrophilic surfaces on titanium and steel, *Materialwiss. Werkstofftech.* **40** (2009) 108–116.
- [170] Bizi-bandoki, P.; Valette, S.; Audouard, E.; Benayoun, S. Time dependency of the hydrophilicity and hydrophobicity of metallic alloys subjected to femtosecond laser irradiations. *Appl. Surf. Sci.* **2013**, *273*, 399–407.
- [171] S. Razi, K. Madanipour, M. Mollabashi, Laser surface texturing of 316L stainless steel in air and water: a method for increasing hydrophilicity via direct creation of microstructures, *Opt. Laser Technol.* **80** (2016) 237–246.
- [172] Y. Guan, F. Luo, G. Lim, M. Hong, H. Zheng, B. Qi, Fabrication of metallic surfaces with long-term superhydrophilic property using one-stop laser method, *Mater. Des.* **78** (2015) 19–24.
- [173] Mehdi Keshavarz Hedayati, Moheb Abdelaziz, Christoph Etrich, Shahin Homaeigohar, Carsten Rockstuhl and Mady Elbahri, Broadband Anti-Reflective Coating Based on Plasmonic Nanocomposite Materials **2016**, *9*, 636.
- [174] Svetoslav Koynov, Martin S. Brandt, and Martin Stutzmann, Black nonreflecting silicon surfaces for solar cells, *APPLIED PHYSICS LETTERS* **88**, 203107, 2006.
- [175] Chee Leong Tan, Sung Jun Jang and Yong Tak Lee, Localized surface plasmon resonance with broadband ultralow reflectivity from metal nanoparticles on glass and silicon subwavelength structures, *Vol. 20, No. 16 / OPTICS EXPRESS* **17448**, 2012.
- [176] J F Verwey, E A Amerasekera and J Bisschop, The physics of SiO₂ layers, *Rep. Prog. Phys.* **53** (1990) 1297–1331.
- [177] Herbert R. Philipp, The infrared optical properties of SiO₂ and SiO₂ layers on silicon, *J. Appl. Phys.* **50**(2), 1979.

Webpages

- <http://www.virginiasemi.com/pdf/BasicCrystallographicPropertiesofSi.pdf>
- <https://www.azom.com/article.aspx?ArticleID=6135>
- https://www.tutorialspoint.com/basic_electronics/basic_electronics_energy_bands.htm
- <http://www.elementalmatter.info/silicon-properties.htm>
- <http://web.ift.uib.no/AMOS/PHYS208/larsP-N/p-n-slide-lars.pdf>
- https://people.eecs.berkeley.edu/~hu/Chenming-Hu_ch1.pdf
- <http://www.iue.tuwien.ac.at/phd/filipovic/node26.html>
- <https://www.geo.arizona.edu/xtal/nats101/s04-19.html>
- <http://ww2.che.ufl.edu/unit-ops-lab/experiments/semiconductors/oxide-growth/Oxide-growth-theory.pdf>
- <http://www.cmxr.com/Education/Short.html>
- <http://www.cmxr.com/Education/Long.html>
- <http://www.cem.msu.edu/~cem924sg/Topic03.pdf>
- <http://www.iue.tuwien.ac.at/phd/hollauer/node11.html>
- <https://www.capitalsteel.net/news/blog/why-does-steel-rust-plus-other-steel-rusting-questions-answered>
- slideplayer.com/slide/4915345/
- https://www.rp-photonics.com/polarization_of_light.html